

# DETECTOR DEVELOPMENT FOR DARK MATTER RESEARCH

VON

ERNST-INGO ESCH

INAUGURAL DISSERTATION  
ZUR  
ERLANGUNG DES DOKTORGRADES  
DER NATURWISSENSCHAFTEN  
DER JUSTUS-LIEBIG UNIVERSITÄT GIESSEN  
(FACHBEREICH PHYSIK)

DECLASSIFICATION: LA-UR-01-3974

LOS ALAMOS,  
17TH SEPTEMBER 2001

© ERNST-INGO ESCH, SEPTEMBER 2001

TYPESET IN PALATINO BY T<sub>E</sub>X AND L<sup>A</sup>T<sub>E</sub>X 2<sub>ε</sub>.

For my parents.



---

# DECLARATION

---

This thesis is an account of research undertaken in the II. Physikalisches Institut, Justus-Liebig-Universität Giessen and in the Physics Division group P-23 of Los Alamos National Laboratory between June 1997 and August 2001.

Except where acknowledged in the customary manner, the material presented in this thesis is, to the best of my knowledge, original and has not been submitted in whole or part for a degree in any university.

---

Ernst-Ingo Esch  
17th September 2001



---

# ABSTRACT

---

One of the major questions in modern astrophysics is the dark matter problem. Even though there is little to no doubt that dark matter exists, it is still not yet known what dark matter is made of. Cosmology provides evidence that the dark matter contains a non-baryonic component. One possible candidate is the existence of weakly interacting massive particles (WIMPs).

This work describes how WIMPs can be detected and what signal type and range can be expected of them. With the expectable low count rate of WIMPs it becomes obvious that the main constraint for recording a dark-matter event is the background of the WIMP signature. One possible detector for such a WIMP experiment can be a lithium drifted silicon detector in which a WIMP interaction generates a nuclear recoil of a silicon atom which produces a detector signal. Los Alamos National Laboratory can potentially get more than 650 lithium drifted silicon detectors with a mass of 100 grams each. Three prototypes of these detectors have been tested to determine the quality of the material and to check their intrinsic background. The results of these tests are documented here.

A possible underground laboratory candidate for these measurement is the waste isolation pilot plant (WIPP). near Carlsbad. This thesis describes the setup of the underground site as well as the background measurements conducted for the gamma and muon background. Several measurements of the gamma background with different shielding material have been done and the results are discussed in detail. The results of the gamma measurements show that the gamma background can be reduced by a factor of 927 with the current shielding material and the underground location.

Since the muons represent the only radiation that cannot be blocked by passive shielding in the underground their flux and induced background is of high importance to all low background experiments. The muon flux is measured with a quadrupel coincidence scintillator detector. An estimate for the muon induced background is discussed. The muon flux is then derived from the data and Monte-Carlo simulations as  $\Phi_{tot} = 5.00^{+0.10}_{-0.14} \times 10^{-7} \frac{Hz}{cm^2}$  which converts into a vertical flux of  $\Phi_{ver} = 3.25^{+0.07}_{-0.10} \times 10^{-7} \frac{Hz}{cm^2 sr}$ . The flux is then compared to that of other underground experimental sites.



---

# ZUSAMMENFASSUNG

---

Eines der Hauptprobleme der modernen Astrophysik ist die schwarze Materie. Obwohl die Existenz von schwarzer Materie mittlerweile allgemein anerkannt wird und selbst die Menge der schwarzen Materie als bekannt gilt ( $40\% \pm 10\%$  der Gesamtenergie im Universum), ist es doch noch immer unklar, woraus die schwarze Materie besteht. Mehrere theoretische Annahmen schließen baryonische Materie aus und die Astronomie in Kombination mit Supersymmetrie hält eine Teilchenlösung für angebracht. Die im Urknall generierten Teilchen (weakly interacting massive particles (WIMPs)), so die Theorie, hätten sich aus der Urknallmasse relativ früh entkoppelt und existierten als Halo in unserer Galaxie und im Universum. Die schwarze Materie formt das schwere Feld im Universum. In dessen Senken befindet sich die baryonische Masse, die die Sterne und Galaxien bildet.

Die vorliegende Arbeit gibt einen Überblick über Fragen zur Kosmologie, die Theorie der Entstehungsgeschichte des Universums. Insbesondere werden die Argumentationspunkte für die Existenz schwarzer Materie im Universum dargestellt und die Diskrepanzen im Modell eines reinen baryonischen Universum gezeigt. Desweiteren werden die zur Zeit gemessenen Massen- und Energieverteilungen im Universum aufgelistet und die Notwendigkeit für die Existenz von schwarzer Materie gezeigt.

Die Nachweismöglichkeiten für WIMPs werden dargestellt, die Energieverteilung eines nuklearen Rückstoßes wird diskutiert und es wird gezeigt, welche Eigenschaften ein Detektor zum Nachweis von WIMPs haben muß. Es wird demonstriert, daß die erwartete Zählrate in einem WIMP Experiment sehr klein ist und das ein genaues Kennen und Unterdrücken des radioaktiven Hintergrunds von größter Wichtigkeit ist. Außerdem werden die momentan vorgeschlagenen und existierenden Technologien zum Nachweis von WIMPs erläutert. Es werden auch die momentanen experimentellen Grenzen für die Masse und den Wechselwirkungsquerschnitt von WIMPs dargestellt.

Das Weak-Interaction Team in Los Alamos National Laboratory hat die Möglichkeit ungefähr 700 Lithium gedriftete Silizium Detektoren von dem St. Petersburg Nuclear Physics Institute zu bekommen. Diese sollen einen Detektor für ein schwarze Materie-Experiment bilden. Drei Prototypen wurden nach Los Alamos gesendet, um ihre Parameter zu bestimmen und zu überprüfen, ob die Kristalle als Detektor

geeignet sind. Zur selben Zeit wurde ein Programm gestartet, um den radioaktiven Hintergrund im Untertagelabor WIPP (Waste Isolation Pilote Plant) in Carlsbad, New Mexico zu messen und festzustellen ob das Labor den Ansprüchen für ein solches Experiment genügt.

Die in Los Alamos zu Verfügung stehenden Silizium-Detektoren werden beschrieben. Die Eigenschaften der Detektoren werden dargestellt und ihre experimentellen Befunde erläutert. Die Entwicklung des Designs und der Bau der Halterung für die Detektoren wird detailliert beschrieben und die Modifikation und Abweichungen von herkömmlichen Standards wird diskutiert. Weiterhin werden die Probleme, die mit den Detektoren auftreten, dargestellt und Lösungswege dafür vorgeschlagen.

Es wird gezeigt, daß die Information über die Untergrundstrahlung für Experimente zur Detektion von schwarzer Materie von extremer Wichtigkeit ist. Der Aufbau eines staubfreien Untertagelabors in WIPP wird beschrieben und es wird erklärt, was die Hintergründe für die Konstruktion waren. Die Messungen des Gamma-Hintergrunds und dessen Unterdrückung mit Hilfe verschiedener Abschirmmaterialien wird beschrieben und es wird gezeigt, daß eine Verminderung der Gamma-Strahlung um einen Faktor von nahezu 1000 mit der zur Verfügung stehenden Abschirmung und der Standortwahl möglich ist. Eine Abschätzung des Gammateilchenflusses in der Abschirmung wird durchgeführt.

Da kosmische Myonen den stärksten Strahlungs-Untergrund auf der Erdoberfläche bilden und sie nicht durch passive Abschirmung aufzuhalten sind, wurde der Standort untertage in WIPP gewählt. Eine ausführliche Messung der kosmischen Myonen wird vorgestellt und die Analyse dieser Daten wird dargestellt. Die vom Myonenfluß abhängigen Untergründe werden dargestellt und mit Hilfe der Daten und Computersimulationen abgeschätzt. Der Myonenfluß wird mit Hilfe von Monte-Carlo-Berechnungen abgeschätzt, als ein totaler Fluß von  $\Phi_{tot} = 5.00^{+0.10}_{-0.14} \times 10^{-7} \frac{Hz}{cm^2}$  der sich dann in einen vertikalen Fluß von  $\Phi_{ver} = 3.25^{+0.07}_{-0.10} \times 10^{-7} \frac{Hz}{cm^2 sr}$  umrechnen läßt. Mit dieser Messung wird anderen hintergrundarmen Experimenten die für WIPP geplant sind der Weg geebnet. Mit Hilfe des Myonenflusses kann gezeigt werden, daß WIPP für die zweite Generation schwarzer Materie-Experimente durchaus geeignet ist, solange das Experiment eine Vetoabschirmung für die Myonen benutzt.

---

# ACKNOWLEDGEMENTS

---

This work was performed at the Los Alamos National Laboratory in cooperation with the II. Physikalisches Institut der Justus-Liebig-Universität Giessen. I want to thank Prof. Dr. Hermann Wollnik who provided me with the opportunity of such a unique problem and situation. My gratitude extends further to my supervisor in Los Alamos, Dr. Andrew Hime and my host Prof. Dr. Thomas J. Bowles for the continuing support and stimulation during the project. Their advice and knowledge in the subject of weak-interaction was very beneficial for me.

I am also grateful for Dr. Salman Habib for his clarifying lectures in cosmology. Thanks are due to the co-students and post doctoral students of the weak interaction team, Dr. Azriel Goldschmidt for his continuous support in physics and personal matters, Dr. Steven Brice for his patience during my questions, Dr. Ralf Guckert, Dr. Klaus Kirch, Dr. Axel Pichlmaier for their help when it was needed and their advice not only as great co-workers but also as dear friends. I want to further more express my gratitude to our two technicians Mel Anaya and Bill Teasdale who helped me in any hands-on problems I encountered. I am also indebted to Dr. John M. O'Donnell the person that taught me all the little details one needs to know to run a computer and its tools.

During my trips to Carlsbad I had to work with the people from the WIPP team. Each one was very helpful in the task of getting my work done. Special gratitude is due to Roger Nelson, the most interesting and bright character I met in Carlsbad for his continued effort to supply me with needed equipment and great advice. I am very grateful for his friendship. Thanks are also due to Dennis Hofer, the man that organized all the paperwork on the WIPP site so my trips there were successful. At last but not least I want to thank Dale Parish and his team for the great support and effort as underground management. Without their fast and excellent help things would not have moved as smoothly as they did.



---

# CONTENTS

---

<b>Declaration</b>	<b>v</b>
<b>1 The Dark Matter Problem</b>	<b>1</b>
1.1 Introduction . . . . .	1
1.2 The Big Bang Model . . . . .	2
1.3 Evidence for Dark Matter . . . . .	5
1.3.1 Dynamic Evidence . . . . .	6
1.3.2 Galactic Rotation Curves . . . . .	8
1.3.3 Gravitational Lensing . . . . .	8
1.3.4 Indirect Evidence . . . . .	10
1.4 Cosmological Parameters . . . . .	11
<b>2 Search for weakly interacting massive particles</b>	<b>15</b>
2.1 Detecting WIMPs . . . . .	16
2.1.1 The annual fluctuation and its detection . . . . .	22
2.1.2 WIMP detection Experiments . . . . .	23
2.1.3 Limits on WIMPs . . . . .	25
<b>3 The Silicon Detector</b>	<b>31</b>
3.1 The Crystals . . . . .	31
3.2 The single Setup for the Prototypes . . . . .	32
3.3 The three Crystal Holder . . . . .	42
3.3.1 Common Design Elements . . . . .	46
3.3.2 The first Stage of the Pre-amplifier . . . . .	47
3.3.3 First Holder Design . . . . .	48
3.3.4 Second Holder Design . . . . .	49
3.4 Measurements at WIPP . . . . .	50
3.5 The Breakdown Problem . . . . .	51
3.6 Modifications and Tests of the Si-Detector . . . . .	52
3.6.1 Vacuum Test . . . . .	52
3.6.2 Temperature Test . . . . .	53

3.6.3	Surface Contamination Tests . . . . .	54
<b>4</b>	<b>Backgrounds at the Waste Isolation Pilot Plant</b>	<b>63</b>
4.1	Background . . . . .	63
4.2	Intrinsic Background . . . . .	63
4.3	Environmental Backgrounds . . . . .	63
4.3.1	Photon Background . . . . .	63
4.3.2	Neutron Background . . . . .	68
4.3.3	Cosmic Ray Background . . . . .	72
4.4	The Waste Isolation Pilot Plant . . . . .	74
4.4.1	The WIPP Lay-Out . . . . .	74
4.4.2	The Experimental Area . . . . .	76
4.5	Gamma background at WIPP . . . . .	81
4.5.1	The Data Acquisition . . . . .	81
4.5.2	Detector Energy Calibration at LANL . . . . .	81
4.5.3	the Background Spectra at LANL . . . . .	82
4.5.4	Detector Energy Calibration at the WIPP . . . . .	86
4.5.5	The background spectra at the WIPP . . . . .	89
4.5.6	Reduction of $^{40}\text{K}$ Flux . . . . .	100
4.6	Muon Background at the WIPP . . . . .	105
4.6.1	Experimental Setup . . . . .	105
4.6.2	Data Analysis . . . . .	106
4.6.3	The Muon-Flux . . . . .	115
<b>5</b>	<b>Summary and Conclusion</b>	<b>125</b>
<b>A</b>	<b>Manufacturing Process of a Commercial Solid State Detector</b>	<b>129</b>
<b>B</b>	<b>Equipment Used</b>	<b>133</b>
B.1	Experimental Equipment . . . . .	133
B.2	Data Analysis and Documentation Equipment . . . . .	134
	<b>Bibliography</b>	<b>137</b>

---

# LIST OF FIGURES

---

1.1	Time line of the universe . . . . .	3
1.2	Galaxy rotation curve . . . . .	9
1.3	Gravitational lensing . . . . .	10
1.4	Summary of matter and energy in the universe . . . . .	12
2.1	Center of mass collision . . . . .	17
2.2	Event versus WIMP mass . . . . .	19
2.3	Events vs. WIMP mass in a range from 0 to 100 GeV . . . . .	20
2.4	Events vs. WIMP mass on a log scale . . . . .	21
2.5	Different Wimp velocity spectra . . . . .	27
2.6	Ratio between observed and actual recoil energy . . . . .	28
2.7	Limits from different WIMP search experiments . . . . .	29
3.1	Design of the single crystal holder . . . . .	34
3.2	Electronic data acquisition system for the Si(Li) crystals . . . . .	34
3.3	$^{57}\text{Co}$ calibration run for the lithium drifted silicone detectors . . . . .	35
3.4	Linear fit of the silicon detector 219 . . . . .	36
3.5	Linear fit of the silicon detector 371 . . . . .	37
3.6	Underground data from WIPP . . . . .	39
3.7	Schematic drawing of the crystal holder . . . . .	43
3.8	Schematic drawing of the crystal holder . . . . .	44
3.9	Setup of a three crystal prototype detector in a clean-room at LANL . . . . .	45
3.10	Schematic of front-end electronics . . . . .	47
3.11	Picture of front-end electronics . . . . .	47
3.12	Design of the differential shielding . . . . .	57
3.13	The breakdown problem vs time . . . . .	58
3.14	10 second interval of all pulses . . . . .	59
3.15	The breakdown problem over time and ADC pulse height . . . . .	59
3.16	Vacuum check system for Si-detector . . . . .	60
3.17	Temperature test for Si-detector . . . . .	61
4.1	$^{238}\text{U}$ decay chain . . . . .	66
4.2	$^{232}\text{Th}$ decay chain . . . . .	67

4.3	Neutron flux for different sources . . . . .	69
4.4	Neutrons created per muon . . . . .	73
4.5	Differential muon intensity . . . . .	73
4.6	The layout of the WIPP . . . . .	75
4.7	The layout of Q-area . . . . .	76
4.8	Linear fit of the gamma spectra taken at LANL . . . . .	83
4.9	Pure background spectrum at LANL . . . . .	85
4.10	Copper background spectrum at LANL . . . . .	87
4.11	Full shielded background spectrum at LANL . . . . .	88
4.12	Linear fit of the gamma spectra taken at WIPP . . . . .	90
4.13	Pure background spectrum at the WIPP . . . . .	92
4.14	Background spectrum at the WIPP inside 1 inches of copper . . . . .	93
4.15	Background spectrum at the WIPP inside 2 inches of copper . . . . .	94
4.16	Background spectrum at the WIPP inside 4 inches of lead and 2 inches of copper . . . . .	95
4.17	Background spectrum at the WIPP inside 12 inches of wax, 4 inches of lead and 2 inches of copper . . . . .	96
4.18	Detector inside full shielding at the WIPP underground . . . . .	97
4.19	All spectra taken with the germanium detector . . . . .	104
4.20	Setup of the efficiency test . . . . .	106
4.21	Setup of the scintillator panels . . . . .	107
4.22	Setup of the scintillator-electronics . . . . .	108
4.23	Timing of the scintillator Coincidence . . . . .	109
4.24	Spectrum of the raw data in scintillator . . . . .	117
4.25	Spectrum for the raw energy in the two scintillator panels . . . . .	118
4.26	Two dimensional spectrum for the cuts applied to the muons . . . . .	119
4.27	Two dimensional spectrum for the cuts applied to the muon Monte-Carlo . . . . .	120
4.28	Energy spectrum of the two panels with spectrum cut . . . . .	121
4.29	Geometric efficiency for different densities at the depth of WIPP . . . . .	122
4.30	Vertical muon flux for different underground experiments . . . . .	123
5.1	Possible annual fluctuation signal . . . . .	128
A.1	Manufacturing process for a hyper pure germanium detector . . . . .	130
A.2	Typical germanium detector cryostat . . . . .	131

---

# LIST OF TABLES

---

1.1	The density contribution of different masses and energies towards $\Omega_0$	13
3.1	Pulsar peak and Full-Width-Half-Maximum (FWHM) distribution for different coltages	38
3.2	Pulsar peak and Full-Width-Half-Maximum distribution for different shaping times.	38
3.3	Fit parameter for the $^{57}\text{Co}$ spectrum	42
3.4	Vacuum pressure readout for the Si-detector	53
3.5	Temperature and pressure during silicon bake out phase	56
4.1	Gamma rays produced by the uranium chain	65
4.2	Gamma rays produced by the thorium chain	68
4.3	Primordial radio nuclide concentration in various materials	78
4.4	Cosmic ray isotopes	79
4.5	Neutron production in rock	80
4.6	Neutron multiplicity factors	80
4.7	Average muon range in rock	80
4.8	TRUMP-card technical data	81
4.9	Sources and their energies	82
4.10	Germanium spectra taken at LANL	84
4.11	Count rates for germanium spectra taken at LANL	86
4.12	Energy fit compared to the real energy with intrinsic peaks	89
4.13	Germanium spectra taken at WIPP	91
4.14	Count rates for germanium spectra taken at the WIPP	98
4.15	Peak intensities inside copper and lead shield	99
4.16	Reduction rates for all spectra	100
4.17	$^{40}\text{K}$ peaks at LANL	101
4.18	Reduction rates for the $^{40}\text{K}$ peak for all spectra	102
4.19	Cuts applied to determine event numbers in muon peak	110
4.20	Tail fits of the background and muon signal	111
4.21	Natural Radioactivity at the WIPP underground	114
4.22	Calculated neutron fluxes at WIPP	114

4.23 The contributing parameter for the muon flux. . . . . 116

## THE DARK MATTER PROBLEM

---

### 1.1 INTRODUCTION

The urge to explain where the human race comes from and how its surrounding environment was created has its root in the early history of mankind. What began with myths and religious beliefs soon turned into theories that could be observed (see for example [COP43], [KEP09], [KEP19] and [GAL32]). Since ancient times mankind has been interested in ideas and theories of how the world, in which we live works. Particular interest was paid to the universe and the stars. Theories about how and why the universe has formed were developed very early in human history.

When the first experiments were conducted to test these theories scientists used the electro-magnetic emissions from the universe in the visible light spectrum. Later the spectrum widened and today most of our knowledge about the universe is based on the observation of electro-magnetic radiation. Today luminous stars are observed as are the x-ray emissions from hot gas or the cosmic microwave background.

Up until 1933, the scientific world was convinced that all matter in the universe was observable through photons. The first evidence for dark matter was brought forward by F. Zwicky in 1933 [ZWI33]. He had observed the red shift of galaxies in the Coma cluster, a nearby cluster of galaxies. His calculations were based on the virial theorem, which states that, for a stable, self-gravitating, spherical distribution of equal mass objects (stars, galaxies, etc), the total kinetic energy of the objects is equal to 1/2 times the total gravitational potential energy

$$\bar{E}_k = \frac{1}{2}E_p. \tag{1.1}$$

Here  $\bar{E}_k$  is the average kinetic energy and  $E_p$  the potential energy of the system. His calculations had shown that the speed of the galaxies should not have been faster than  $80 \frac{km}{s}$ . His observation of the velocity distribution by red shift analysis however had shown that the speeds reached up to  $1000 \frac{km}{s}$ , more than one order of magnitude larger than expected. He concluded the strong possibility of the existence of some sort of “dark matter”. A matter type not absorbing or emitting electro-magnetic radiation which was responsible for the speed increase.

Since then cosmology and astrophysics have derived more evidence for the existence of dark matter. The idea that was very controversial for many years, later found great acceptance. Today there is a strong consensus in the scientific world, that non-electro-magnetically observable matter exists and makes up the major part of the matter in the universe. Many hypotheses have been postulated about the nature of dark matter. The ideas vary from baryonic dark matter such as large Jupiter size objects that are distributed throughout the galaxy or clouds of gas to non baryonic dark matter such as halos of fundamental particles.

## 1.2 THE BIG BANG MODEL

Common understanding in the cosmological society today states that the universe has its origin in the big bang, a state of infinite density. Evidence for this theory was discovered by Hubble in 1929 [HUB29] when he found that galaxies were departing from each other at a velocity  $v$  that is proportional to their distance  $l$

$$v = H(t)l. \quad (1.2)$$

This finding was in agreement with Einstein’s general relativity theory [EIN16] which also states a relationship between distance and velocity. The expansion of the universe was therefore taken as evidence that general relativity describes the universe correctly. With these equations it is now possible to take the present data and calculate back in time. The universe’s density and temperature increases inversely to the time flow. This means the universe was hotter and denser in the past than it is today. This temperature and density condition can be retraced to a point of classical singularity where the density and temperature go to infinity - the big bang - at time 0. The big bang theory was first expressed by Gammov and his collaborators in the late 1940’s [GAM46] [ALP48].

With the theories of modern physics it is now possible to generate a time line of the universe from the big bang to today (see figure 1.1) [SCR98]. After the big bang

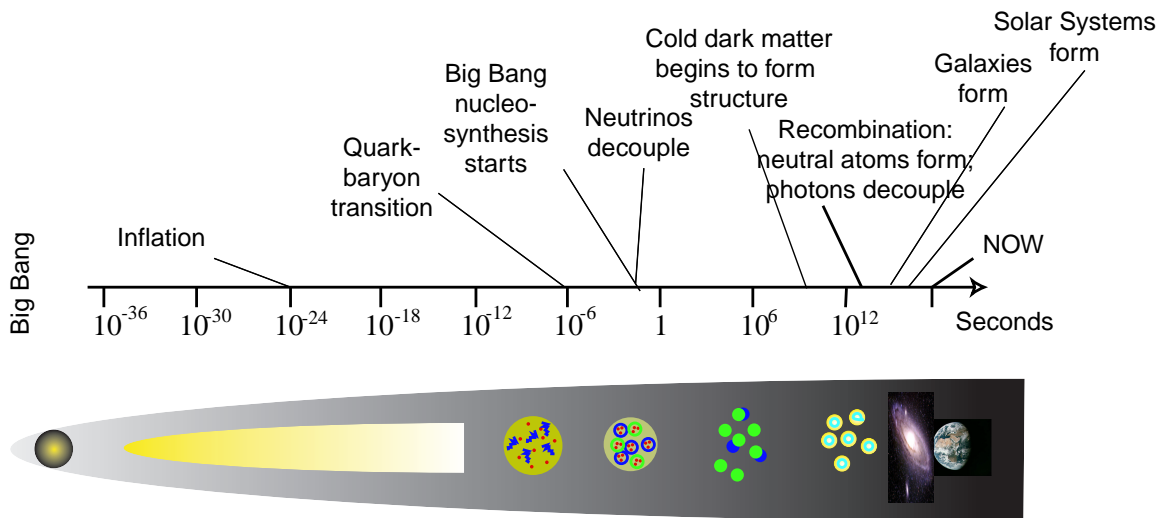


**Figure 1.1:** Time line of the universe.

had occurred, the very hot universe expanded on a rapid scale. In the first  $10^{-30}$  seconds quarks, leptons and gauge bosons condensed. Protons and neutrons were formed after the first several micro seconds. The first primordial nuclei synthesized about a second after the big bang. Hydrogen, helium and small amounts of lithium were generated during this time. This process of primordial nucleosynthesis was completed after about 3 minutes. The temperature of the universe was still too high to allow the nuclei to capture electrons. Matter and radiation was in equilibrium. The existing charged particles constantly scattered background radiation of photons. When the decoupling of matter and radiation was possible the first atoms were able to form. This recombination happened about ten thousand years after the big bang. Since matter and radiation was now decoupled the universe became transparent to radiation.

Due to this transparency the primordial radiation field still exists and can be observed as the microwave background radiation. Because the universe is still expanding today the photon field has lost energy and therefore shifted its frequency down into the microwave region. The existence of the microwave background has first been postulated by Gamow, Alpher and Herman in 1949 [GAM49]. It was detected in 1965 by Penzias and Willson [PEN65].

After about  $10^8$  years past the big bang the matter in the universe formed galaxies. Our Solar system formed about  $10^9$  years after the big bang. We know today

that the universe is still expanding. The questions now are what is responsible for the expansion of the universe, will it expand forever or will it collapse? The main parameter is the mean density  $\rho$  of the mass [HAB97] and energy [TUR98] in the universe. A critical density  $\rho_c$  exists that determines the fate of the universe. If  $\rho$  is smaller than the critical density, the gravitational force will not be able stop the expansion of the universe. If  $\rho$  is equal to  $\rho_c$ , the universe expansion will asymptotically come to a stop but it will not collapse. If the density lies above the critical density, the universe will slow down its expansion and finally collapse under the gravitational force. The critical density is [HAB97]

$$\rho_c = \frac{3H_0^2}{8\pi G} \quad (1.3)$$

where  $H_0$  is the Hubble constant today and  $G$  is Newton's gravitational constant. With a Hubble constant of  $65 \frac{km}{s Mpc}$ <sup>1</sup> the density comes out as

$$\rho_c = 4 \times 10^{-30} \frac{g}{cm^3}. \quad (1.4)$$

One can now define a parameter  $\Omega_0$  which describes the density compared to the critical density

$$\Omega_0 = \frac{\rho}{\rho_c}. \quad (1.5)$$

If  $\Omega_0$  is equal to one, the universe is closed, if it is smaller than one, the universe will expand forever (open) and if it is greater than one the universe will collapse again. Observations of luminous baryonic matter in galaxies (counting the stars in a galaxy and assuming an average mass per star) have shown that its density is just [WIL98]

$$\Omega_{luminous} = \frac{\rho_{luminous}}{\rho_c} \sim 0.003. \quad (1.6)$$

Observations of galaxies (see subsection 1.3.1) however show that  $\Omega_M$ , the total matter density in the universe is  $0.33 \pm 0.045$ . These observations are made by measuring the rotational speed of galaxies (see subsection 1.3.2). This would make our universe an open universe, it would expand forever. Theoretical and experi-

---

<sup>1</sup>A parsec (pc) is 3.258 light-years or  $3 \times 10^{13}$  kilometers

mental physicists share the idea of a mass ratio of [TUR01]

$$\Omega_0 = 1 \pm 0.05. \quad (1.7)$$

Theorists explain their confidence in an  $\Omega_0$  extremely close to one by a theory called inflation theory. The theory states that the initial conditions for the universe in its beginning have to be strongly constrained. For a large range of parameters the expansion from the postulated infinite high density and energy state would collapse under the force of gravity almost instantly or expand so rapidly that no structure can form. Only a universe with an  $\Omega_0$  very close to one would be able to survive as long as our own universe and form structure as we know it today. The inflation theory postulates a rapid expansion of the universe in the first  $10^{-32}$  seconds. During this time the universe grows by a factor of  $10^{43}$ . The theory predicts deviations from critical density not larger than one part in  $10^{60}$ . The inflation phase long before the matter - radiation decoupling makes it possible for quantum fluctuation to become large scale structure forming parameters.

Experimental physicists believe that  $\Omega_0$  should be equal to one from microwave background data (see section 1.4) which is also the strongest evidence for the inflation theory [ALL97].

Scientists have found evidence in several different experiments [TUR99] that  $\Omega_M$  has to be significantly larger than  $\Omega_{luminous}$ . It is widely acknowledged that the missing density is linked to matter which is not emitting electro-magnetic radiation, the so called dark matter.

### 1.3 EVIDENCE FOR DARK MATTER

The experimental evidence for dark matter has evolved since the 1930's [ZWI33]. Today several independent observations agree on the idea of dark matter in the universe. They are described in the following subsections.

The observation of dark matter contains these different topics:

- dynamic evidence
- galactic rotation curves
- gravitational lensing
- indirect evidence from structural formation

### 1.3.1 DYNAMIC EVIDENCE

The dynamic evidence for dark matter is the oldest form of observation. The red shift distribution of galaxies in clusters and the observation of dwarf galaxies rotating around a large galaxy have been used for these experiments. The principal idea behind the experiment is to measure the red shift of the light coming from the galaxies in the cluster or the dwarf galaxy and determining with this measurement their relative velocities to each other. Then one can calculate the mass necessary to obtain the derived velocity and compare it with the mass derived by counting the stars in the galaxies and thereby estimating the galaxies weight.

F. Zwicky postulated in 1933 [ZWI33] for the first time that the universe consists of much more than the luminous matter. His main assumptions were based on different experimental facts known from the red shift of stars and galaxies:

- The red shift is analog to a Doppler effect.
- The Doppler speed is proportional to the distance  $r$ .
- There is a neglected amount of absorption and scattering of light in the universe related to the red shift.
- The resolution of his instruments is known to him and the distance of the galaxies observed are in the expected geometric relationship. Which meant the galaxies really form a cluster.
- The types of electro-magnetic spectra from galaxies are independent from the distance of the galaxy.
- The speed of light from the observed galaxy to the observer is constant and known

Zwicky had observed the red shift of different galaxies in the Coma cluster. He found with the virial theorem (equation 1.1) that the red shift in the coma cluster was varying by  $1500 \frac{km}{s}$  to  $2000 \frac{km}{s}$ . To explain the discrepancies he proposed four ideas.

1. The Coma cluster has reached a mechanical equilibrium. Therefore the virial theorem (equation 1.1) describes the relationship between  $\bar{E}_k$  the average kinetic energy and  $\bar{E}_p$  the potential energy. His estimate of the kinetic energy gave an average speed of  $80 \frac{km}{s}$ . To get an average velocity of  $1000 \frac{km}{s}$  the

density of the cluster had to be four hundred times heavier than it appeared to be. From this he concluded that there was much more “dark matter”, matter he was not able to see optically in the cluster.

2. The Coma cluster is not in equilibrium and equation 1.1 is not valid. In this case all the potential energy would show as kinetic energy and one would have [ZWI33]

$$\bar{E}_k = -\bar{E}_p. \quad (1.8)$$

This would increase the average kinetic Energy by a factor of two, which still does not provide a solution and is an argument for dark matter.

3. The mean density is completely given by the luminous matter such as stars, x-ray emitting clouds of gas. Then the cluster will drift apart in time. If this is true other isolated galaxies with speeds of  $1000 \frac{km}{s}$  to  $2000 \frac{km}{s}$  should have been observed in the universe. This is not the case.
4. One can interpret the galaxies velocities as virtual speeds caused by Einstein’s red shift resulting from his relativistic theory [EIN16]. This would result in a velocity of only  $10 \frac{m}{s}$ . In order to reach the observed average speed one would have to allow even more dark matter density than in case 1 and 2.

From this time on scientists have observed galaxy clusters to determine their velocity distributions. The common consensus was that the virial mass was distributed the same way as the luminosity. The first important discussion of galactic luminosity functions was done by Hubble in 1926 [HUB26]. In 1942 Zwicky [ZWI42] summarized results for large numbers of low luminosity galaxies and suggested that the luminosity is in monotonic relationship to their magnitude.

In order to determine the mass to light ratio in a range better than orders of magnitude, one had to estimate the mass of a cluster in a better way [COW87]. This was done by observing hot X-rays coming from the cluster. The assumption made was such that the mass followed the galaxy distribution in the cluster. Gunn and Thomas [GUN96] had attempted to lower the baryonic ratio in the cluster by questioning this assumption. Giradis’ calculations [GIR98] in 1998 found that the X-ray analysis and the optical mass analysis agreed.

The observations of dwarf galaxies enables scientists to determine the mass of the main galaxy. With the rotation speed of the dwarf galaxy and its distance to the

center of the main galaxy it is possible to make predictions about the mass distribution in the main galaxy and their variation from the luminous matter. This technique has shown that the galaxy appears to be significantly larger ( $100 - 200kpc$ ) than the reach of the luminous matter ( $20kpc$ ) or even the hydrogen ( $50kpc$ ).

### 1.3.2 GALACTIC ROTATION CURVES

Rotation curves are velocity distribution curves in galaxies for varying radii  $R$ . The radius of the galaxy is measured from the galactic center to the outside of the galaxy. The velocities are measured by observing the Doppler red shift of stars and hydrogen clouds of the galaxy. Rotation curves are only measurable in disk-galaxies. Observations have shown that the velocity distribution throughout many of the galaxies is flat. Kepler's law however predicts a slope proportional to  $\frac{1}{r^2}$  for the assumption that most of the mass is distributed in the center of the galaxy.

In order to make statements about the dark matter in a galaxy it is important to know every contributing mass term in the galaxy. The masses are distributed in the luminous disk, the bulge of the center stars, a spherical baryonic dark halo around the disk and a much larger halo of non-baryonic matter (see for example [KEN87]). All these masses contribute to the rotation curve. The curve can be observed to a radius of  $20kpc$  with stars rotating in the disk, and up to  $50kpc$  with hydrogen red shift. Because of the lack of luminous material it is not possible to map out the velocity curve further than a radius of  $50kpc$ . Therefore the total mass distribution and size of the dark halo cannot be determined. If the highest percentage of mass in a galaxy is luminous matter then the biggest portion of matter is located in the galaxy center. Therefore the velocity distribution of objects in the galaxy should fall off towards the outside. As mentioned above the mathematical description varies from galaxy to galaxy. However the galaxies observed show a flat velocity distribution all the way to the possible observable radius of  $50kpc$ . To obtain such a distribution more mass has to be present in the outside regions of the galaxy than one observes. Figure 1.2 shows the velocity distribution of one galaxy (C3198) the data was taken from [KEN87] The solid line represents the measured data, the dashed line is the curve one achieves if the mass distribution would be proportional to the mass distribution of the stars in the galaxy.

### 1.3.3 GRAVITATIONAL LENSING

Gravitational lensing has to be distinguished between strong lensing and weak lensing. The idea is based on the lensing effect of mass. Every gravitational field

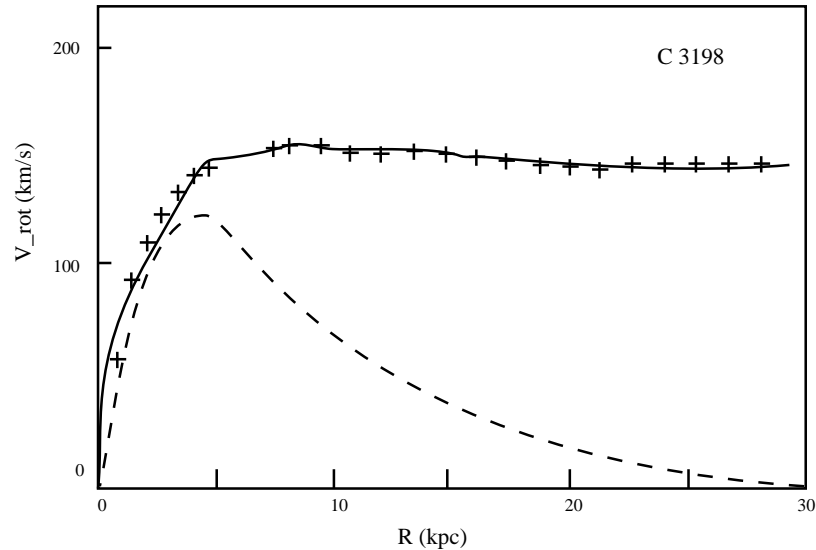


**Figure 1.2:** Velocity distribution of one galaxy (C3198) the data was taken from [KEN87] The solid line represents the measured data, the dashed line is the curve one achieves if the mass distribution would be proportional to the mass distribution of the stars in the galaxy.

bends light away from its straight line. Figure 1.3 shows the principal of the gravitational lensing effect. In the case of strong lensing one looks at a patch of background stars. If a massive object is in front of these stars, the light will be bend and more light is focused towards the observer. A star in this background will appear brighter while the dark object is in the front similar to an optical lens. The observed signal is a brightening and dimming of the star. It is symmetric over time. Since the electromagnetic emission spectrum only changes in amplitude it is possible to distinguish between a strong lensing effect and a variable star, where the signal of the energy spectrum changes.

In weak lensing one looks at very distant galaxies as background and the observed object is usually a galaxy in the foreground. The galaxies in the background are just visible as diffuse light blobs with a oval like shape. Onto each one a coordinate system is attached. During the lensing effect the angles of the coordinate system are changing while the foreground object (galaxy) is moving. This way, it is possible to calculate the total matter in the foreground galaxy and a measurement of the dark halo's size and mass can be done. The data derived from weak lensing is at this time still statistically weak but a galaxy size of  $100kpc$  to  $200kpc$  can be calculated[HAB97].

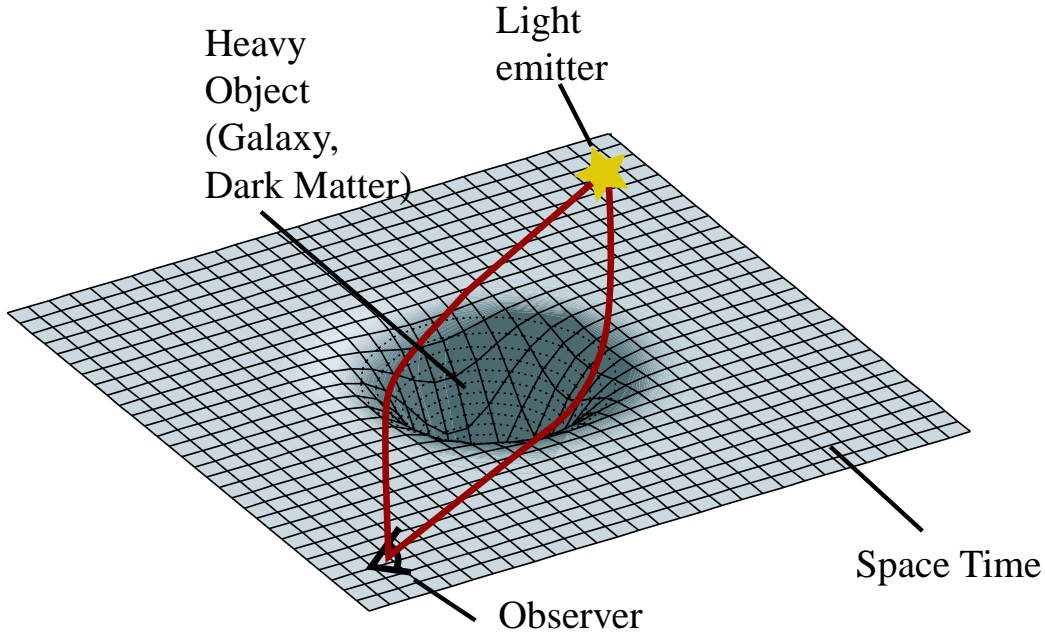


**Figure 1.3:** Schematic diagram of the gravitational lensing effect. The Object to be observed appears brighter since the Heavy object focuses the light to the observer.

#### 1.3.4 INDIRECT EVIDENCE

The indirect evidence is based on Big Bang Nucleosynthesis (BBNS). BBNS provides a theory describing the amount of mass condensed as baryonic matter in the universe. BBNS has only one free parameter,  $\eta$  [KAP01]. It is defined as

$$\eta = \frac{\text{number of baryons}}{\text{number of photons}}, \quad (1.9)$$

the ratio of the number of primordial baryons to the number of photons in the universe. This relative abundance can be compared with observations of luminous matter in galaxies [KAP01] where

$$\eta \approx 5.1 \pm 0.02 \times 10^{-10}. \quad (1.10)$$

The amount of primordial baryonic matter can so be calculated and a certain mass density in the universe today can be derived [HAB97]. Together with the cosmic microwave background radiation (CMB) experiments BBNS can make very strong restraints on the total mass and energy density of the universe. Photons that make up the microwave background traveled unhindered through time since the recombination. The small deviation of the temperature for this background leads to the conclusion that the intrinsic fluctuation of temperature and gravitational potential was very small at the time when photons decoupled from matter.

The results from the CMBR experiments combined with BBNS lead to the consequence that there was not sufficient time in a pure baryonic universe to create structure formations as we see them today. Non-baryonic dark matter would be able to explain the structure formation. With the ability not to couple to photons it could generate density perturbations before the recombination occurs. Without violating the constraints for density given by the microwave background large density perturbations could have been generated.

## 1.4 COSMOLOGICAL PARAMETERS

As shown in section 1.2, the quantity of matter in the universe is an essential question in the field of cosmology.  $\Omega_0$  is directly dependent on the Hubble constant. The latest measurement from Freedman [FRE01] determines  $H_0 = 72 \pm 7 \frac{km}{s Mpc}$ . This measurement displays the first one where the largest part of the error is due to systematics and not due to statistical effects. One can write  $\Omega_0$  [TUR98] as the sum

$$\Omega_0 = \sum_i \Omega_i \quad (1.11)$$

where  $\Omega_i$  represents the different fractions of the critical density in the universe. Current theories assume that  $\Omega_0$  can also be written as

$$\Omega_0 = \Omega_M + \Omega_\Lambda. \quad (1.12)$$

$\Omega_M$  is the ratio contributed to  $\Omega_0$  by mass. It consists of fractions coming from stars, neutrinos baryons, cold dark matter (non-baryonic matter) and dark energy. Table 1.1 shows the distribution of the different parts.  $\Omega_\Lambda$  represents a dark energy density which is not directly coupled to mass but can be seen as a result of the cosmological constant from Einstein's general relativity theory. The observable  $\Omega_\Lambda$

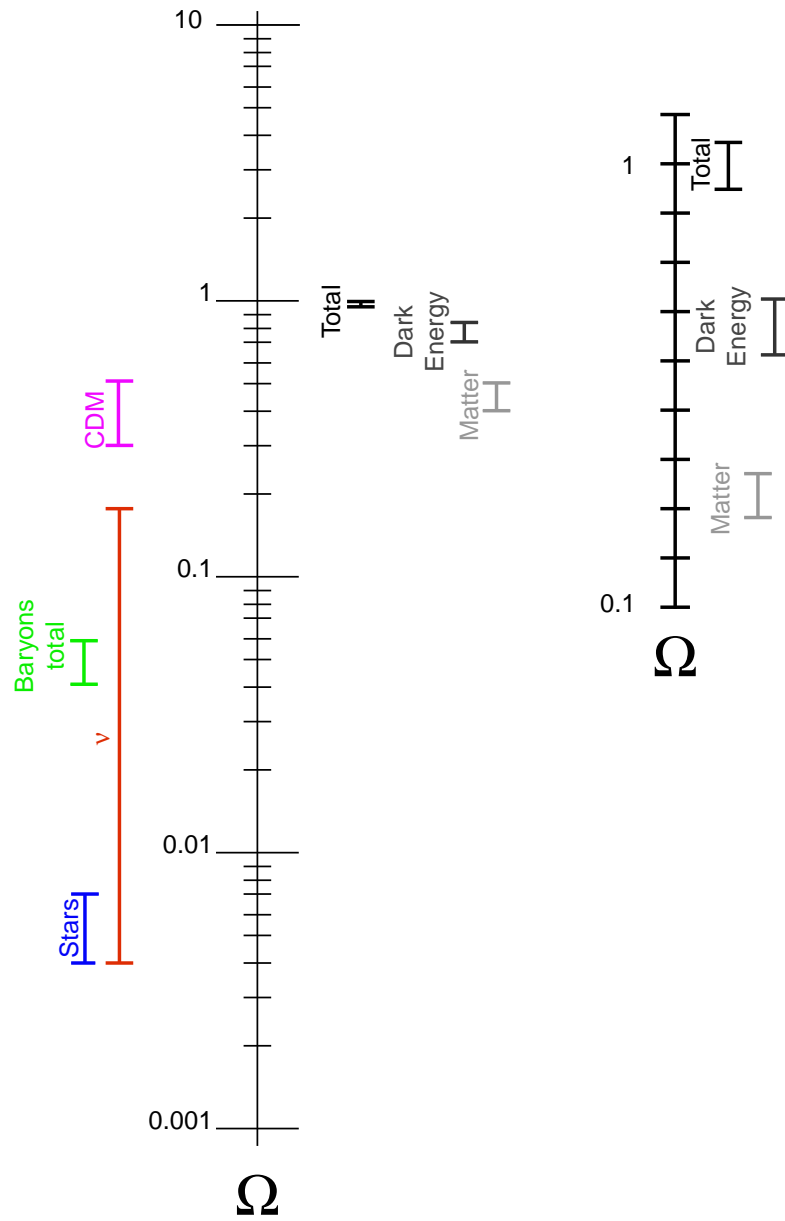


Figure 1.4: Summary of matter and energy in the universe.

is related to a so called dark Energy. Scientists today do not know what the dark energy consists of or how to test it. The only fact known about this energy is that it has an accelerating effect on the universe. The discovery of the effect of the dark energy by Perlmutter [PER99] represents the largest mystery of cosmology and probably fundamental physics today. Figure 1.1 [TUR99] shows the distribution of

Matter type	Fraction contributed
$\Omega_{\text{Stars}}$	$0.005 \pm 0.002$
$\Omega_{\text{B}}$	$0.040 \pm 0.012$
$\Omega_{\nu}$	$\geq 0.003 \leq 0.18$
$\Omega_{\text{CDM}}$	$0.29 \pm 0.1$
$\Omega_{\Lambda}$	$0.67 \pm 0.06$
$\Omega_{\text{M}}$	$0.33 \pm 0.045$
$\Omega_0$	$1 \pm 0.05$

**Table 1.1:** The density contribution of different masses and energies towards  $\Omega_0$ . The data is taken from [TUR98]

$\Omega_i$ 's from different experiments. The contribution of the matter in the universe can be written as follows: Neutrinos : more than 0.3% and less than 18%, Stars 0.5%, baryons 4%, cold dark matter 29% and a dark energy of some kind 60% (see also table 1.1). The total matter density in the universe is  $\Omega_0=1$ .

The lower limits for neutrinos in stars have been measured by neutrino experiments such as Super Kamiokande [FUK98] to be a contribution of not more than 3% of the critical density. Just recently the SNO experiment demonstrated with their first data that the neutrino contribution to the total critical density is not more than 18% [SNO01]. An additional constraint comes from the big bang theory and their models. If neutrinos would make up more than 20% of the critical density in the universe then the universe, so predicted by the models, would have evolved from large structure to small structure ("top-down"). Only with cold dark matter could the universe have evolved from small structure to large structure (galaxies, clusters, super-clusters). Recent red shift observations show that the universe has evolved from the "bottom-up".

Data from the anisotropy of the cosmic microwave background (CMB) can be used to determine the total density  $\Omega_0$ , the ratio of mass to baryon  $\Omega_{\text{M}}/\Omega_{\text{B}}$  [HUW97] Several experiments have been made to measure the anisotropy spectra, the latest measurement from the DASI CMB interferometer [PRY01] and a new value from

reevaluated data from Boomerang [NET01] have shown similar values.

The baryon to matter density ratio can also be obtained by x-ray measurements (see [MOH98],[EVR96]) of galaxy clusters and the Sunyaev-Zel'dovic (SZ) distortion of the CMB (see [GRE01],[CAR00]). In order to do so one has to make two assumptions [TUR01]. The assumptions are that if clusters are averaged over a large enough scale they represent a fair sample of the matter in the universe and that the baryons in clusters are mainly due to hot x-ray emitting gas or stars.

The third way to determine the baryon to matter density ratio is the extraction from observations of primeval abundance of deuterium [OME01] and an accurate theoretical prediction of the light element abundance in the early universe (see [BUR98],[BUR01]) These measurements are the most accurate ones available today

Turners analysis of  $\Omega_B$  and  $\Omega_M$  [TUR01] shows the values for these two parameters to be  $\Omega_B = 0.040 \pm 0.012$  and  $\Omega_M = 0.33 \pm 0.045$ . This is a clear indication that more than 87% of the matter present in the universe is non-baryonic.

The density  $\Omega_\Lambda$  results from accurate distance measurements to more than fifty supernovas of type 1a conducted by Reiss et. al. [SCH98] and Perlmutter et. al. (see [PER99],[RIE98]). The principal idea is that if the universe is slowing down then distant objects should be moving faster than predicted by Hubble's law. The conclusion from the measurements show that the Universe is speeding up and forces an  $\Omega_\Lambda$  to exist.

At the same time the experiments BOOMERANG (balloon observation of millimetric extra galactic radiation and geophysics) [NET01] and DASI [PRY01](degree angular scale interferometer) delivered data from CMB powerspectrum observations. Their results are confirming the the super-nova results from Perlmutter and Reiss. By combining the results one deduces  $\Omega_\Lambda = .7 \pm 0.3$ . This fits very well with  $\Omega_M = .4 \pm 0.1$  and  $\Omega_0 = 1 \pm 0.2$ .

# SEARCH FOR WEAKLY INTERACTING MASSIVE PARTICLES

---

As discussed in chapter 1 a strong case for non-baryonic dark matter exists. Most common theories predict the non-baryonic dark matter to be made of exotic particles remaining from the early stages of the universe. Two types of dark matter particles can be considered. Particles that had relativistic energies at the time of freeze out, so called hot dark matter (like the neutrinos) and particles that were non-relativistic when they decoupled from the remaining equilibrium of the universe. The latter is referred to as cold dark matter. Two cold dark matter particles are most favored by scientists, axions and WIMPs. Both particles are in conflict with the standard model. Models of super symmetry are needed to explain these particles. Since the evidence for non-baryonic dark matter exists it is of importance for fundamental physics to find these particles and to map out their properties. The opportunity to detect cold dark matter is not only relevant to the field of cosmology but also bears high importance for the physics beyond the standard model.

The axion displays an example for a particle that could have been created in the early universe. The particle was postulated to solve the problem of CP violation in the strong interaction [PEC77]. The abundance of axions is strongly dependent on the considered model. Experiments searching for axions have been performed (see for example [PAN87]). Their limits are still 3 orders of magnitude away from cosmologically significant axions. Since the presented work revolves around WIMPs, axion experiments are not presented here.

The weakly interacting massive particles or WIMPs display a generic class of particles that were non-relativistic at the time of freeze out. WIMPs are not conforming with the standard model of particle physics. They are particles that can only be described in a larger super symmetric model. This makes a WIMP experiment also a test for the standard model. WIMPs are described as particles that are only

interacting gravitationally and weakly. They are massive non-relativistic particles. Their mass range set by super symmetry models is between  $1\text{GeV}$  and  $50\text{TeV}$ . Their weak cross section is smaller than  $10^{-5}$ . The search for this particle can be compared with the search for the neutrino by Fred Reines [REI59] after it was postulated by Wolfgang Pauli in 1932 [PAU30].

It can be shown that their present density is a function of their annihilation rate during their freeze out process [LEE77]. It can be argued that if WIMP's exist the temperature and density in the early universe was high enough to keep the WIMPs( $\delta$ ), quarks ( $q$ ) and leptons ( $l$ ) in chemical and kinetic equilibrium through the process of annihilation.

$$\delta\bar{\delta} \leftrightarrow l\bar{l} \quad (2.1)$$

$$\delta\bar{\delta} \leftrightarrow q\bar{q} \quad (2.2)$$

With the expansion of the universe the temperature drops. At a certain point the temperature will have dropped below a point where the annihilation rate is much less than the expansion rate of the universe and the WIMP's freeze out. On the universal time scale this might have happened milliseconds after the big bang.

## 2.1 DETECTING WIMPS

### WIMP-INTERACTIONS

To find WIMPs two different detection methods can be used ([PRI88],[BER95]). One is direct detection through a WIMP interacting with the detector through nuclear recoil. This is discussed later in this chapter. The other method is to detect WIMPs indirectly through their assumed annihilation products such as neutrinos produced by WIMP annihilation in the earth or the sun, or anti-protons and high energy gamma rays produced by them in the galaxy (for example [SIL84]).

### THE WIMP ENERGY SPECTRUM

Current theories [SMI90] assumed that WIMPs are distributed throughout our galaxy as a halo. The average velocity of the WIMPs is supposed to be zero compared to the velocity of the galaxy. Now the idea is to compute a possible energy spectrum that these particles would generate in a nuclear recoil detector. The inci-

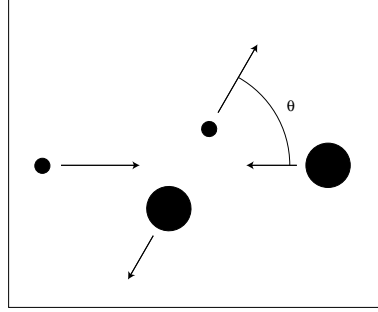


**Figure 2.1:** Center of mass collision.

dent kinetic energy  $E_1$  of a non-relativistic particle is given by

$$E_1 = \frac{1}{2}M_D\beta^2, \quad (2.3)$$

with  $M_D$  as mass of the particle. The units chosen are  $GeV$  for the mass and  $\beta c$  for the velocity of the particle. For a center of mass scattering angle  $\Theta$  (see figure 2.1) the nuclear recoil energy is given by

$$E_r = E_1 r \frac{1 - \cos(\Theta)}{2} \quad (2.4)$$

where  $r = \frac{4M_T M_D}{(M_T + M_D)^2}$  and  $M_T$  represents the mass of the target nucleus. The maximum scattering energy is given by  $E_M = E_1 r$ . Because of the low energy scattering the angular distribution is isotropic in the center of mass. Therefore the differential rate is  $\frac{dR}{d\omega} = \frac{R_0}{4\pi}$  and with equation 2.4 one can deduce  $\frac{dE_r}{d\omega} = \frac{E_1 r}{4\pi}$ . A recoil spectrum for a single energy is then given by

$$\frac{dR}{dE_r} = \frac{R_0}{E_1 r} \quad \forall \quad 0 < E_r < E_1. \quad (2.5)$$

To obtain the integrated recoil spectrum, a velocity distribution is needed. Assumed is a Maxwellian distribution

$$\frac{dn(\beta)}{d\beta} = n_0 (\pi\beta_0^2)^{-\frac{3}{2}} 4\pi\beta^2 \exp\left(-\frac{(\vec{\beta} + \vec{\beta}_e)^2}{\beta_0^2}\right), \quad (2.6)$$

$n(\beta)$  is the number density of the dark matter particles with the velocity  $\vec{\beta}c$ ,  $\vec{\beta}_e c$  is the earth velocity through the dark matter halo and  $n_0$  is the total number density with

$$n_0 = \frac{\rho_{\text{DM}}}{M_D}, \quad (2.7)$$

where  $\rho_{\text{DM}} = 0.3 \text{ GeV cm}^{-3}$  [SMI90].

If the speed of the earth ( $\beta_e = 0$ ) in equation 2.6 is neglected the differential event rate for a target nucleus can be simplified to

$$dR(\beta) = dn(\beta)\beta\sigma_t \frac{6 \times 10^{26}}{A} s^{-1} kg^{-1}. \quad (2.8)$$

$A$  represents the target nucleus mass number. Combining equation 2.8 and 2.6 yields

$$\frac{dR}{d\beta} = c_1 \beta^3 \exp\left(-\frac{\beta^2}{\beta_0^2}\right) \quad (2.9)$$

with

$$c_1 = n_0 (\pi\beta_0^2)^{-\frac{3}{2}} 4\pi\sigma_t \frac{6 \times 10^{26}}{A} s^{-1} kg^{-1}. \quad (2.10)$$

Because for each WIMP velocity there is an equal distribution of event rates (see equation 2.5) the spectral shape from equation 2.9 has to be multiplied with the normalized value for each  $\beta$ . The normalized equation 2.5 is given as

$$\frac{dR(\beta)}{dE_r} = \frac{2}{rM_D M_T \beta^2}. \quad (2.11)$$

The following integral can now be assembled as

$$\int \frac{dR}{dE_r} dR = \frac{2}{rM_D M_T} c_1 \int_{\sqrt{\frac{2E_r}{M_D r}}}^{\infty} \beta \exp\left(-\frac{\beta^2}{\beta_0^2}\right) d\beta. \quad (2.12)$$

The lower limit of the integral is the minimum value of maximum recoil energy for a given  $\beta$ , every  $\beta$  smaller than that can not generate this maximum recoil energy. Therefore the limits are set from  $\sqrt{\frac{2E_r}{M_D r}}$  to infinity. The total spectrum is then given

by

$$\frac{dR}{dE_r} = \frac{1}{rM_D M_T} c_1 \beta_0^2 \exp\left(-\frac{E_r}{E_0 r}\right) \quad (2.13)$$

and can be written as

$$\frac{dR}{dE_r} = \frac{R_0}{E_0 r} \exp\left(-\frac{E_r}{E_0 r}\right) \quad (2.14)$$

with

$$R_0 = \frac{2}{\sqrt{\pi}} n_0 \beta_0 c \sigma_t \frac{6 \times 10^{26}}{A} s^{-1} kg^{-1}. \quad (2.15)$$

With this knowledge it is possible to approach the problem in two different ways.

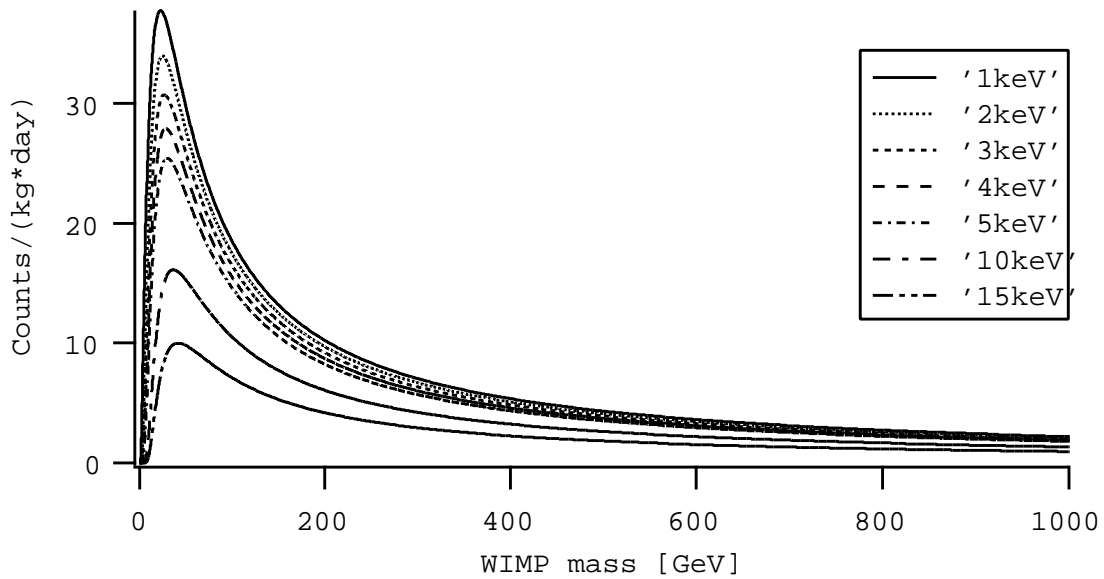


**Figure 2.2:** Event versus WIMP mass. The expected event rate shown in this plot was calculated with a non-relativistic left-handed neutrino cross section. The detector material was assumed to be silicon. The events are shown as a rate in  $[\frac{events}{kg\ day}]$ . The legend shows the various lower thresholds (1,2,3,4,5,10 and 15 keV). The upper threshold was set at 30 keV.

One can calculate the expected event rate for a certain massive WIMP or a limit

on cross section versus WIMP mass can be set. Since the cross section of a WIMP-nucleus interaction is unknown, this method can only be used as a guideline. The second way hosts the opportunity to determine limits of the WIMP-nucleus cross section and the WIMP mass.

In order to determine the total expected rate in a detector with a given threshold

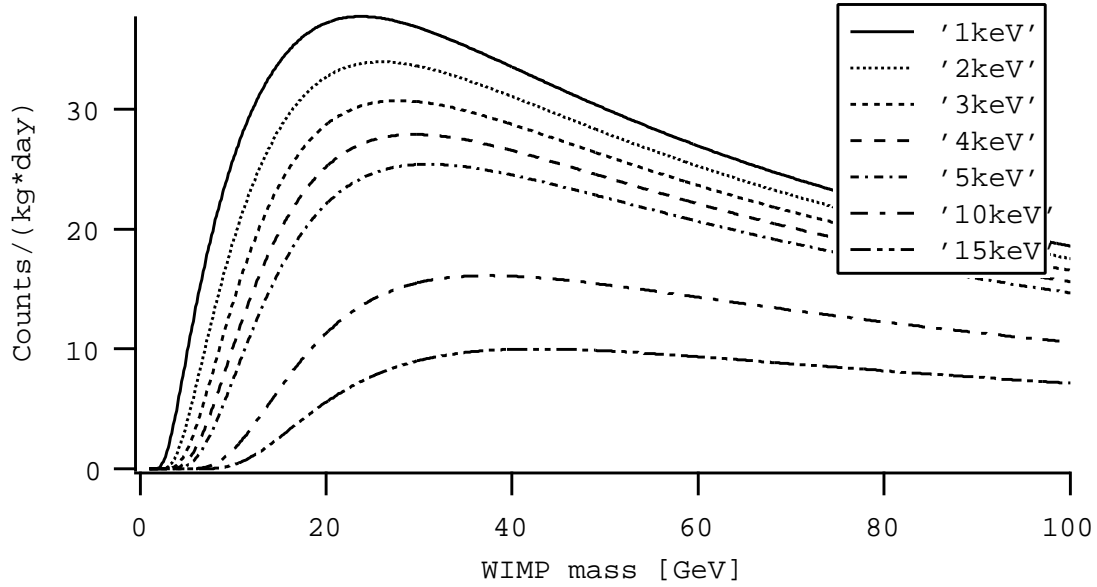


**Figure 2.3:** Events vs. WIMP mass in a range from 0 to 100 GeV. This plot enhances the region between 0 and 100 GeV of Figure 2.2

an assumption about the WIMP - nucleus cross section has to be made. Very often a cross section for non-relativistic coherent (left-handed) neutrino scattering is used [SMI90]. It can be written as

$$\sigma_T = \frac{G_F^2}{2\pi} \mu^2 K_N^2 \text{ with} \quad (2.16)$$

$$\mu = \frac{M_T M_D}{M_T + M_D} \text{ this can be written as} \quad (2.17)$$

$$\sigma_T \approx 2 \times 10^{-39} M_D M_T r K_N^2 \quad (2.18)$$

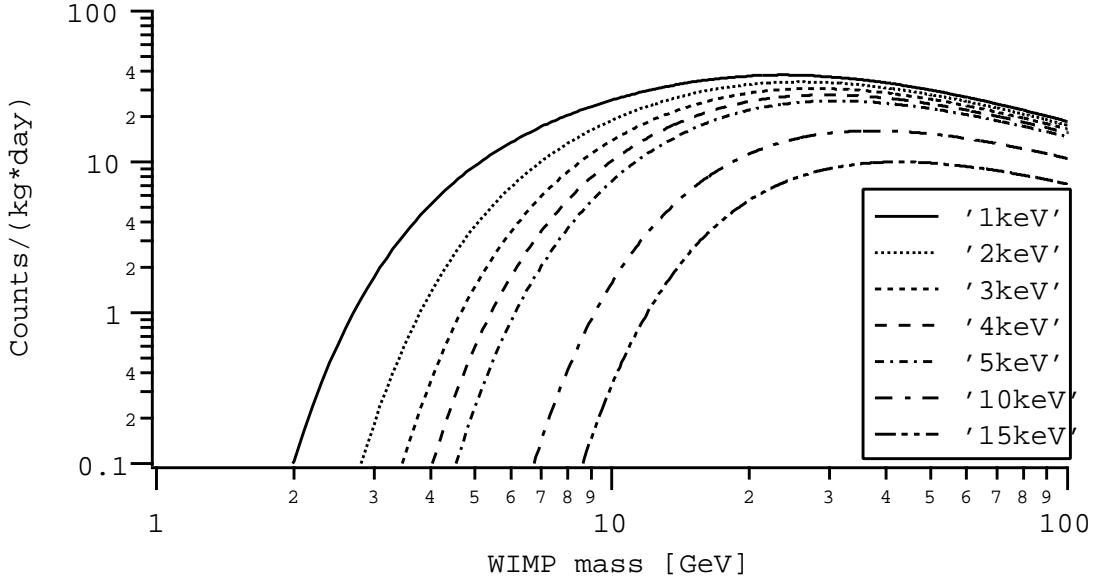


**Figure 2.4:** Events vs. WIMP mass on a log scale. The expected event rate shown in this plot was calculated with a non-relativistic left-handed neutrino cross section. The detector material was assumed to be silicon. The events are shown as a rate in  $[\frac{events}{kg\ day}]$ . The legend shows the various lower thresholds (1,2,3,4,5,10 and 15 keV). The upper threshold was set at 30 keV.

where  $\sigma_T$  is in units of  $cm^2$ ,  $G_F$  represents the Fermi constant and  $K_N$  the coherent factor:

$$K_N \approx \frac{(A - Z)}{2}. \quad (2.19)$$

The fraction of the number of neutrons comes from the fact that neutral current interaction for protons is small and only half the neutrons have a spin that is aligned correctly. To determine the total rate in an energy interval equation 2.14 has to be integrated between the lower and upper threshold limit.

$$R = \int_{\text{threshold}}^{\text{max. Energy}} \left( \frac{R_0}{E_0 r} \exp\left(-\frac{E_r}{E_0 r}\right) \right) dE_r \quad (2.20)$$

$$= R_0 \left( \exp\left(-\frac{E_r(\text{threshold})}{E_0 r}\right) - \exp\left(-\frac{E_r(\text{max Energy})}{E_0 r}\right) \right) \quad (2.21)$$

The count rate derived from this cross section is extremely sensitive to the lower threshold. Figures 2.2, 2.3 and 2.4 show the expected rate for different thresholds. The calculations were made for lower thresholds as shown in the graph and the upper threshold was always 30 keV. The assumed WIMP-speed for the calculation was  $\beta c = 270 \frac{km}{s}$  and the WIMP-density  $\rho_{DM}$  was equal to  $0.3 \frac{GeV}{cm^3}$ . The calculation shows that one has to expect a low signal rate. With such a small rate it becomes extremely important to reduce and know the contributing backgrounds of the experiment.

### 2.1.1 THE ANNUAL FLUCTUATION AND ITS DETECTION

Accounting for the velocity of the earth, one can approach the limits of WIMP detection in a different way. The earth is circling around once going with the movement of the galaxy and once against it. In the simplest approach, the earth is revolving in a circle around the sun. The speed distribution of the WIMPs is the given by

$$\beta(t) = \beta_0 + \beta_E \cos\left(\frac{\pi}{12}t\right). \quad (2.22)$$

Here  $\beta_0$  is the mean distribution of the velocity in  $\beta c$  and  $\beta_E$  is the earth velocity  $\beta_E c = 30 \frac{km}{s}$ . One can now integrate over an average speed per month to determine the spectrum expected for this time of year

$$\bar{\beta}(t) = \beta_0 + \beta_e \int_{month-0.5}^{month+0.5} \cos\left(\frac{\pi}{6}t\right) dt. \quad (2.23)$$

In numbers the two opposite months have a speed of  $c\beta_1 = 278 \frac{km}{s}$  and  $c\beta_2 = 262 \frac{km}{s}$ . Figure 2.5 shows the two differential spectra. In this case the region of interest is between 2 and 12 keV of nuclear recoil energy. The integral over this region gives the expected rate of the signal. The maximum velocity rate is  $W_+ = 19.1$  events per day per Kilogramm and the minimum speed velocity is  $W_- = 17.0$  events per day per Kilogramm. The difference  $\Delta W = W_+ - W_-$  is 2.1 events per day per Kilogramm which is a roughly 11 percent effect. With this knowledge it is now possible to determine the amount of mass needed to distinguish between the two signals. The signal can be written as a two component sum:

$$S = B + W \pm \Delta W \quad (2.24)$$

with  $S$  as the signal achieved by the detector,  $B$  the Background in the detector and  $W$  the signal coming from the nuclear recoil of the WIMPs. To distinguish the two wimp rates the resolution of the detector has to be at least  $\frac{1}{2}\Delta W$ . With  $m$  as the mass of the detector in  $[kg]$  this can be written in the following equation:

$$\sqrt{mS} = \frac{1}{2}m\Delta W. \quad (2.25)$$

Solving this equation for the mass term one achieves

$$m = \frac{4S}{\Delta W^2}. \quad (2.26)$$

Since the WIMP signal is small the background is extremely difficult to reduce. A large detector mass designed to look at the annual fluctuation provides therefore a possibility to deal with higher background. In the case of figure 2.5 and for a mass of  $65kg$  one could distinguish the spectra if the background in the region of interest is lower than 71.7 counts per Kilogramm per day. This translates into a count rate of not more than 7.17 counts per  $keV$  per Kilogramm per day in the region of interest for recoil energies between  $2keV$  and  $12keV$  nuclear recoil in silicon.

During a nuclear recoil event in a solid state detector not all the energy is transformed into ionizing energy. The energy is split up between the ionization process and the generation of phonons. Phonons are resonances in the crystal structure itself. The magnitude of this effect varies for low recoil energies between 10% and 40%. Figure 2.6 shows the recoil energy over the ionized energy produced by the recoil event as the percentage of the recoil event. The solid line is the theoretical predictions [LIN63], the round points are data points from [GER90] the squares are from [SAT65]. In recoil energy regions between  $2keV$  and  $12keV$  the actual spectrum achieved shifts down into the  $0.2keV$  to  $3.6keV$  region. That means that in addition to a low background the detector also needs a very low threshold to be able to see the signal.

### 2.1.2 WIMP DETECTION EXPERIMENTS

Different solid state detector experiments in search of WIMP's have been conducted. The material of choice was mostly germanium, silicon or NaI scintillators. In the first two cases the recoil energy from an event generates electron-hole pairs in a semiconductor material such as germanium or silicon. In the third case the recoiled nucleus generates a scintillation signal. This technique is less effective than

the ionization process and hence deriving the signal is even more difficult. Additional experiments with calorimetric detectors have been done to detect WIMPs.

### IONIZATION DETECTORS

Several experiments for limits on WIMPs with germanium detectors were first used in double beta decay experiments like Caldwell's double beta decay experiment [CAL88], the Heidelberg-Moscow experiment [BAU98a] and the Godhard germanium experiment [REU91]. Their detector mass was always on the order of up to one Kilogramm. Plans for the future are including ideas such as the self shielding germanium detector [BAU97] which is designed to consist of two germanium detectors one surrounding the other and thereby being able to actively shield the inner detector with an excellent veto. A different approach is the proposal for the one ton germanium detector GENIUS (germanium nitrogen underground setup) [BAU98a] where the detector mass will be placed directly into a large tank of liquid nitrogen. This nitrogen would also act as shielding material against the background. Germanium is preferred for its purity and the potential to generate large crystals. The drawback of using germanium is the relatively small recoil energy generated in the detector.

The first silicon experiment in search for WIMPs was conducted by Caldwell et al. [CAL90]. The experiment consisted of an array of four planar lithium drifted silicon detectors mounted on a single cold finger. The total mass of the detector was 17g. The detector mass in this experiment is rather small. The advantage of silicon over the purer and easier to generate germanium detectors is its smaller atom weight which results in a larger nuclear recoil.

### SCINTILLATOR EXPERIMENTS

Scintillator detectors have been built to detect the dark matter particles. They trade off low threshold for large target mass which results in high event rates. There are several experiments proposed by groups like the United Kingdom Dark Matter Project [SPO91], the BPRS collaboration [BAC92] and the Team of Osaka [FUS93]. The purity of the NaI crystals can meet the values of hyper-pure germanium but the threshold is limited to about  $4keV$  in the scintillator [FOR95]. Additionally the low scintillation efficiency of low recoil energies correlates a  $4keV$  event seen in the scintillator to a true recoil energy of  $16keV$  for Na and  $60keV$  for I. The DAMA (dark matter search) collaboration has a NaI detector with a mass of  $100kg$  operating at Gran Sasso. This group claims to see a WIMP signal [BEL01].

### CALORIMETRIC DETECTORS

A somewhat different and more difficult approach is the measurement of the recoiling energy in a calorimetric detector. The detector works by converting the deposited energy into heat. The temperature increase is then measured. The detector consists of an absorber crystal, a thermal conductance to a heat bath at very low temperature and a thermometer. To detect energies in the range of  $5keV$  it is necessary that the detector is cooled into the  $mK$  region. The energy threshold can be pushed as low as  $0.5keV$  and energy resolution is as good as  $4.5eV$  [FIO84]. The detectors can be made with a large choice of materials which can be used as identifying criteria for a WIMP signal. Detectors up to a size of  $1kg$  have been proposed [FOR95]. The environmental background can be reduced strongly since the experiments need only the heat connector and the detector itself. Difficulties of these experiments are the ultra low temperature requirements and the technology to use large masses.

### DETECTORS WITH MIXED TECHNOLOGY

One approach to distinguish between the nuclear recoil and a gamma ray event was done by the CDMS (cryogenic dark matter search) collaboration [DAS96] and by the CRESST (cryogenic rare event search with super conducting thermometers) collaboration [BUH96]. The germanium detector uses two channels to detect the energy. The calorimetric approach is used to detect the deposited heat and an ionization channel is used to measure the numbers of electron-hole pairs created during the event. Since the thermal and ionization energy deposited during a nuclear recoil and a gamma event differ it is possible to distinguish between recoil and gamma events. This method can be used to subtract the gamma background. Since the detector temperature has to be held in the  $mK$  level the cryogenics involved generate an obstacle. Furthermore the detectors are still limited in size.

#### 2.1.3 LIMITS ON WIMPS

Since WIMPs have not yet been detected, current experiments can only set limits on their existence. Equation 2.21 demonstrate that the count rate achieved in a detector is dependent on the interaction cross section of the WIMP with the nucleus or the nucleon and the WIMP mass. Therefore limits on WIMPs are usually portrayed in a two dimensional plot. The x-axis displays the possible mass of the WIMP and the y-axis the interaction cross section with a nucleon. The nucleon-interaction cross section is chosen since it provides the possibility to compare de-

tectors with different target material with each other. The relation between the nuclear cross section  $\sigma_T$  and the nucleon cross section  $\sigma_n$  is given by [BAU01]

$$\sigma_T = \sigma_n A^2 \left( \frac{M_T}{M_D + M_T} \right)^2 \left( \frac{M_D + M_n}{M_n} \right)^2. \quad (2.27)$$

Here just like above  $A$  represents the nucleon number,  $M_D$  is the assumed WIMP mass,  $M_T$  the target nucleus mass and  $M_n$  the mass for the nucleon. Figure 2.7 show the most recent constraints for WIMPs [CAL99]. The lines of the different experiments represent the upper limit of cross section and mass constraint. Everything on the right side and above the line is canceled out by the experiment. One can see that the most stringent constraint comes from the NaI experiment DAMA. Figure 2.7 does not show the constraints from all experiments conducted. The plot limits itself to the most recent and strongest constraints. The area marked "Theory" is the theoretically predicted constraint on WIMPs [BED97]. These constraints are due to different theoretical predictions in super symmetry, cosmology and big bang nucleosynthesis. It is clear that the experiments are not yet in the same region as the theory and are therefore not yet able to put constraints on the theory.

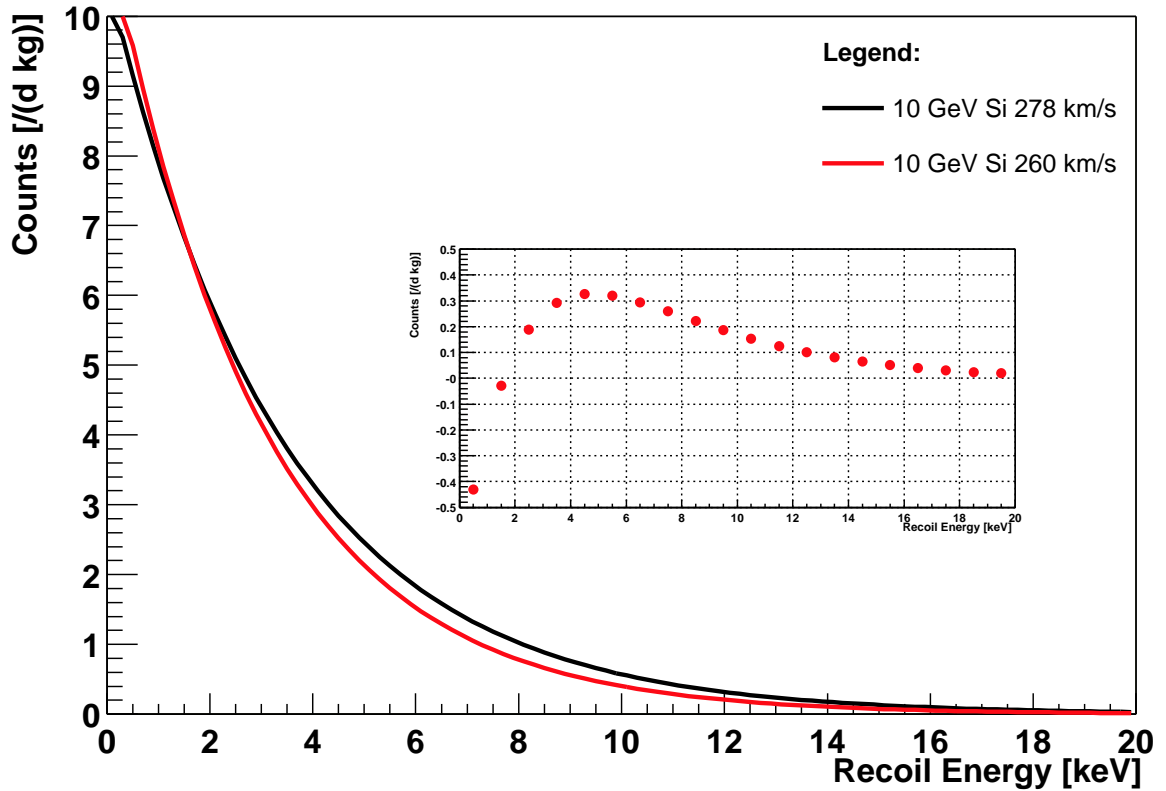


**Figure 2.5:** Different Wimp velocity spectra. This plot shows the different spectra expected in SiLi detectors for maximum and minimum speed of the earth through the dark matter halo. It represents a 10 GeV WIMP, a maximum speed of  $278 \frac{km}{s}$  and a minimum speed of  $260 \frac{km}{s}$ . The left axis shows the expected rate per day per Kilogram of detector mass and the bottom is the recoil energy in Kilogram. The inlay graph displays the residual for the two spectra. It is visible that the region of interest is in a recoil energy region of 2 to 12 keV.

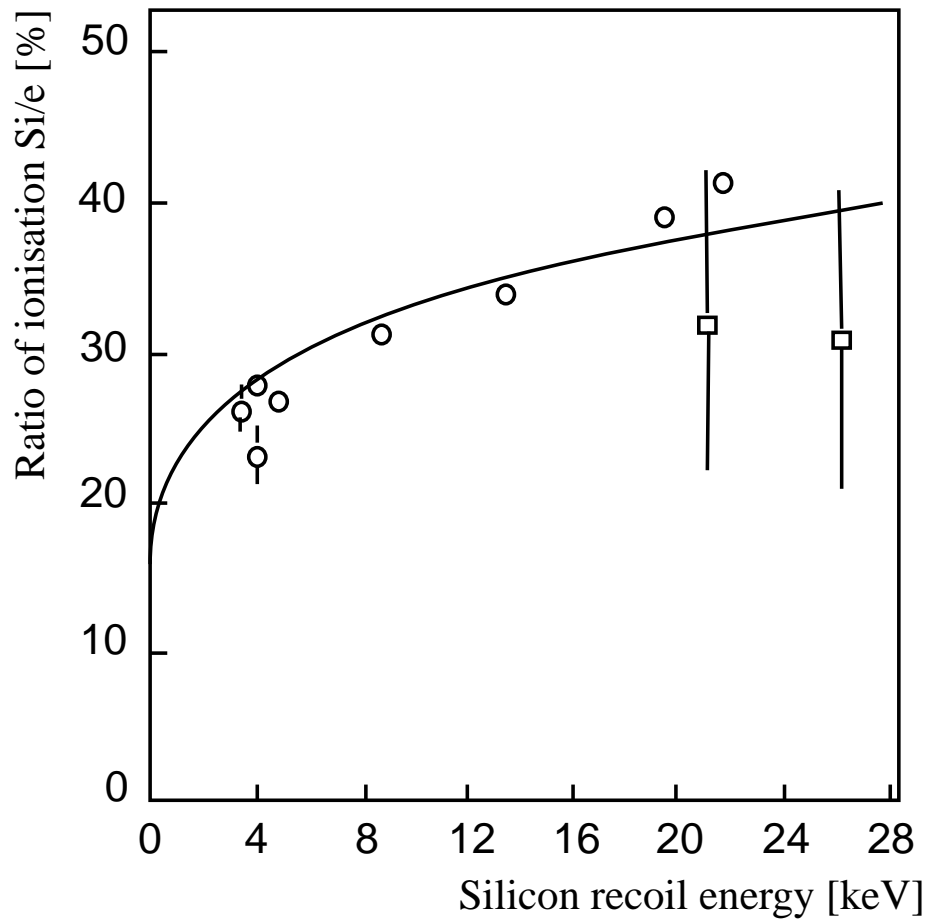


**Figure 2.6:** Ratio between observed and actual recoil energy. The line resembles the calculated ratio for silicon [LIN63], the circles are from [GER90] and the squares are from [SAT65].

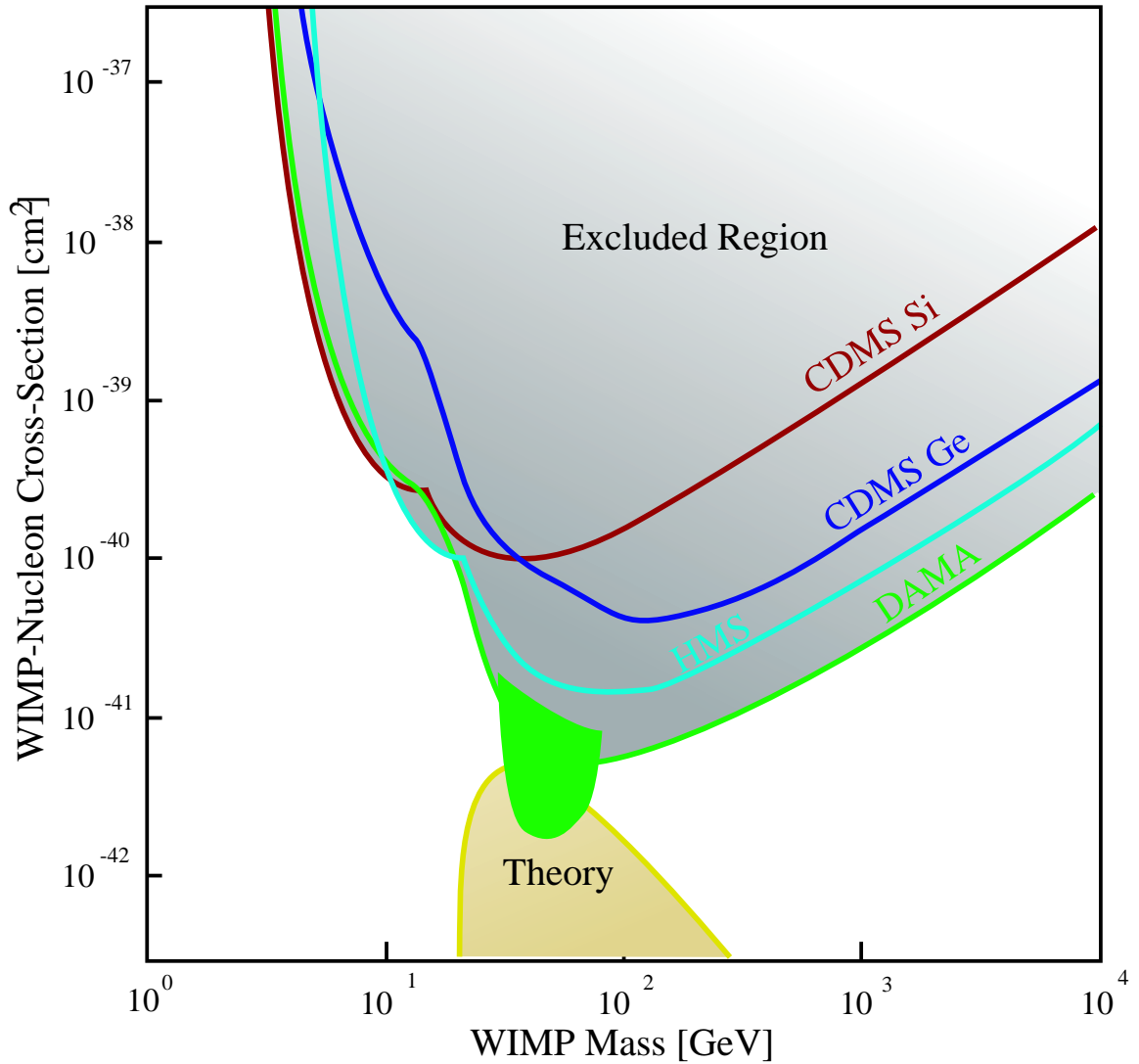


**Figure 2.7:** Limits from different WIMP search experiments. The strongest limit can be set by the DAMA NaI scintillator experiment. The filled region on that line represents the DAMA annual modulation data with a  $3\sigma$  confidence level [BER00]. Also shown are the CDMS silicon and germanium constraints and the Heidelberg-Moscow search (HMS). The lines represent the lower limit achieved by the experiment. Everything above and to the right of the line has been tested by the particular experiment.



---

## THE SILICON DETECTOR

---

### 3.1 THE CRYSTALS

Throughout the physics community exists an ongoing effort in the field of cosmology to determine the density parameter  $\Omega$  of the universe [TUR98]. As discussed in the previous chapter evidence lead to the assumption that the larger part of this parameter is governed by mass we cannot see, so called Dark Matter. One possibility is Weakly Interacting Massive Particles (WIMPs or neutralinos). These particles can be detected in a nuclear recoil event inside a solid state detector. The WIMPs are assumed stationary in the universe so their relative speed is determined by the speed of the earth in the galaxy ( $\approx 280 \frac{km}{s}$ ). Therefore the nuclear recoil produced is on the order of  $0-30 keV$ . Because lighter nuclei produce larger recoil energy, silicon is a preferred candidate.

The Weak-Interaction-Team at Los Alamos National Laboratory has the opportunity to obtain  $75kg$  of lithium drifted silicon detectors for a dark matter project. This amounts to about 700 crystals. To launch a dark matter project of this size one has to map out the qualities of the crystals and the quality of the radioactive background in the experimental area. Three of the crystals were obtained from the St. Petersburg institute of nuclear science in Russia to do the prototype testing and determine the quality of the detectors. Since the count rate expected in such experiments is very low it is important to know the backgrounds of the experiments very well. A radioactive background analysis of the experimental site had to be performed in parallel to this effort (see chapter 4).

Each crystal prototype is of cylindrical shape with a diameter of  $27-29mm$  and  $100mm$  in height. The inner diameter is  $8mm$ . The operating voltage is  $+800V$ . Each crystal has a serial number etched into it on the outside cylinder. They were manufactured by L. A Popeko and A.I. Derbine at the St. Petersburg Nuclear Physics Institute. Figure 3.9 shows a picture of the third stage of a three crystal

prototype assembly at Los Alamos National Laboratories.  $75kg$  are available for building a large scale WIMP detector. To determine the intrinsic contamination and the noise levels of these crystals three (serial numbers 219, 371 and 636) were setup in a prototype cold-finger.

## 3.2 THE SINGLE SETUP FOR THE PROTOTYPES

During the manufacturing of the first low-background copper cold-finger and dewar each crystal was tested in an unused lithium drifted germanium detector dewar. A copper crystal holder was designed (see Figure 3.1) to mount on a Princeton Gamma Tec cold-finger. A cold-finger is an element designed to be used as a heat conductor between a dewar with cooling liquid and an object that has to be cooled. It is usually made from copper. To reduce radioactive background the holder is manufactured from oxygen free copper (see section 4.3.1). The idea is to hold the crystal in place with a vice-like apparatus clamping the top and bottom thereby allowing a good heat flow from the crystal. To prevent having the housing under high voltage the crystal is separated from the copper by a thin capton foil. The high voltage is then connected to the crystal with a copper clamp around the crystal. The signal wire is connected to a hole in the center of the crystal by a tempered steel spring pressing against the inside walls of the hole. The design of the model RG-11A pre-amplifier is changed such that the FET of the pre-amplifier which is mounted inside the pre-amplifier housing is moved onto a Teflon plate attached to the cold-finger itself close to the detector inside the cryostat. This way the FET is cooled to liquid nitrogen temperature and its electronic thermal noise is reduced. The holding device is constructed to hold always only one detector at a time. Three lithium drifted silicon detectors were exchanged in turns and placed under high voltage. Each detector is cleaned on the outer surface with a lint-free cloth soaked with isopropynol and then assembled in the holder and attached to the cold-finger. The cold-finger is then hooked up to a vacuum pump and pumped down to a vacuum less than  $3.5 \cdot 10^{-7} torr$ . After that the cold-finger was cooled down during a time period of at least 24 hours. Each crystal is monitored for breakdown and a spectrum from a  $^{57}Co$  source is taken. The electronics data acquisition setup is shown as schematic in Figure 3.2. The pre-amplifier used in the electronic system is the modified RG-11A described above. The signal is then sent through an ORTEC 672 shaping amplifier and fed into an ADC mounted on a trump pc-card. Technical details of the ADC and the card can be found in table 4.8.

It was observed that two of the three detectors were working correctly after the

operating voltage was connected, the third one was breaking down. During the first test the leakage current at different voltages was monitored. Each crystal was mounted in the dewar cup while the operating voltage was applied in steps of 100V and the leakage current was monitored. The voltage was increased in time intervals of 1 minute. The voltage was ramped up from 0 to 1000 volts. For each crystal the leakage current was read out at the readout port of the Bertran 1755P high voltage power supply for current monitoring as  $206 \pm 1 \text{ nA}$  with a multi-meter. The same measurement was done with the crystal removed from the setup and the high voltage only connected to the pre-amplifier. The readout revealed  $60 \pm 3 \text{ nA}$ . The difference results in a leakage current of  $146 \pm 4 \text{ nA}$ . Since the leakage current for a crystal of this magnitude is not known one can only compare it with the numbers in smaller silicon detectors which vary from  $10^{-11} \text{ A}$  to  $10^{-8} \text{ A}$ . Since two detectors were working and because of their size and the fact that each detector showed the same relatively high leakage current the number was accepted. The leakage current suggests a resistance under bias voltage of  $5.7 \text{ G}\Omega$ . This brings the leakage current into the same current region one expects from a  $10^4$  electron-hole pair generating event which is equivalent of a radiation event of about  $3 \text{ keV}$  (see [KNO99]). This number can be treated as the detector limitation of the threshold.

An attempt to optimize the bias voltage was made by adding a pulser into the test signal input. Incomplete depletion of the detector volume results in a partly unbiased detector and the amount of random electron hole pairs increases. This results in additional noise and can be reduced by applying higher bias voltage. On the other hand with increasing bias voltage the leakage current will increase and thereby induce noise into the signal. Therefore the pulser was added into the test input of the pre-amplifier and the signal was recorded with the bias crystal attached to the input of the pre-amplifier. The idea was to find an optimum voltage under which the depletion of the crystal was complete and the leakage current was inducing an acceptable amount of noise into the system. The pulser amplitude was 4 Volts which after going through the electronics resulted in a channel number of 3255 out of 8192. The input pulse was chosen such that it would be well above the noise threshold at channel 150-200. The pulse rate was  $25 \text{ kHz}$ . The applied voltage was then increased up and the mean of the peak and the full-width-half-maximum was used to determine the best voltage setting. Table 3.1 shows that it was not possible to determine the optimum in voltage for the full depletion of the detector. The resolution shown in table 3.1 has a value of roughly 1%. This number displays a value which is comparable within a factor of 2 with large modern germanium detectors. Specs called for not more than 1100 Volts as bias voltage. The electronic noise completely dominated in this test. Therefore the test was not continued over

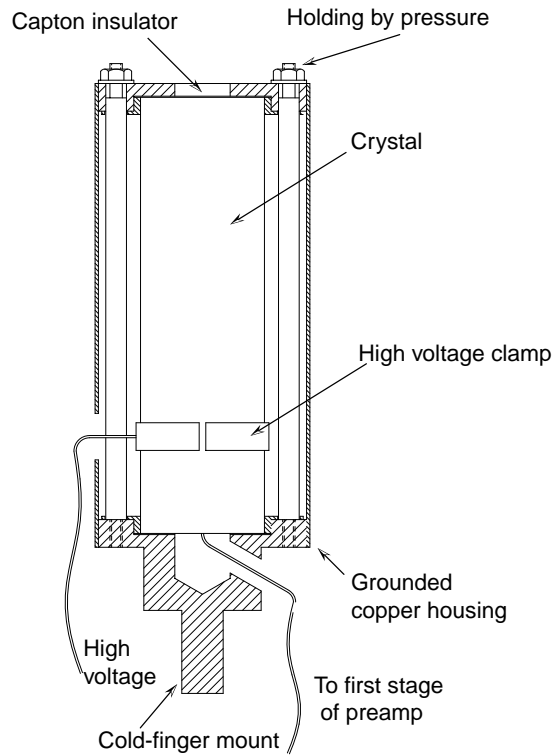


**Figure 3.1:** Design of the single crystal holder. This device was designed to be able to quickly test each crystal for its functionality.

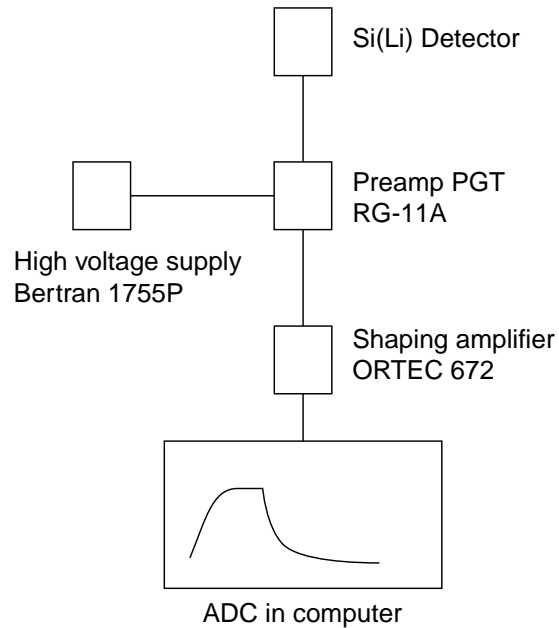


**Figure 3.2:** Electronic data acquisition system for the Si(Li) crystals.

1100 Volts. Since the variation of the FWHM was so large it was concluded that the noise was dominated by electronic noise, not by noise generated from the crystal. The optimum voltage was therefore set as quoted by the specs to 800 Volts. This value was measured by the group that grew the crystal. [DER97]

In the next test an attempt was made to minimize the Full-Width-Half-Maximum (FWHM) by choosing the optimum shaping time in the shaping amplifier. Table 3.2 shows the shaping time and the according FWHM and the mean of the peak at 1000 Volts. One can see that the FWHM has its minimum at  $6\mu s$ . The optimum shaping time is directly connected with the rise-time of the pulse. With the assumption of a cylindrical electric field inside the crystal the maximum rise-time for a pulse generated at a certain voltage can be calculated in the below following way.

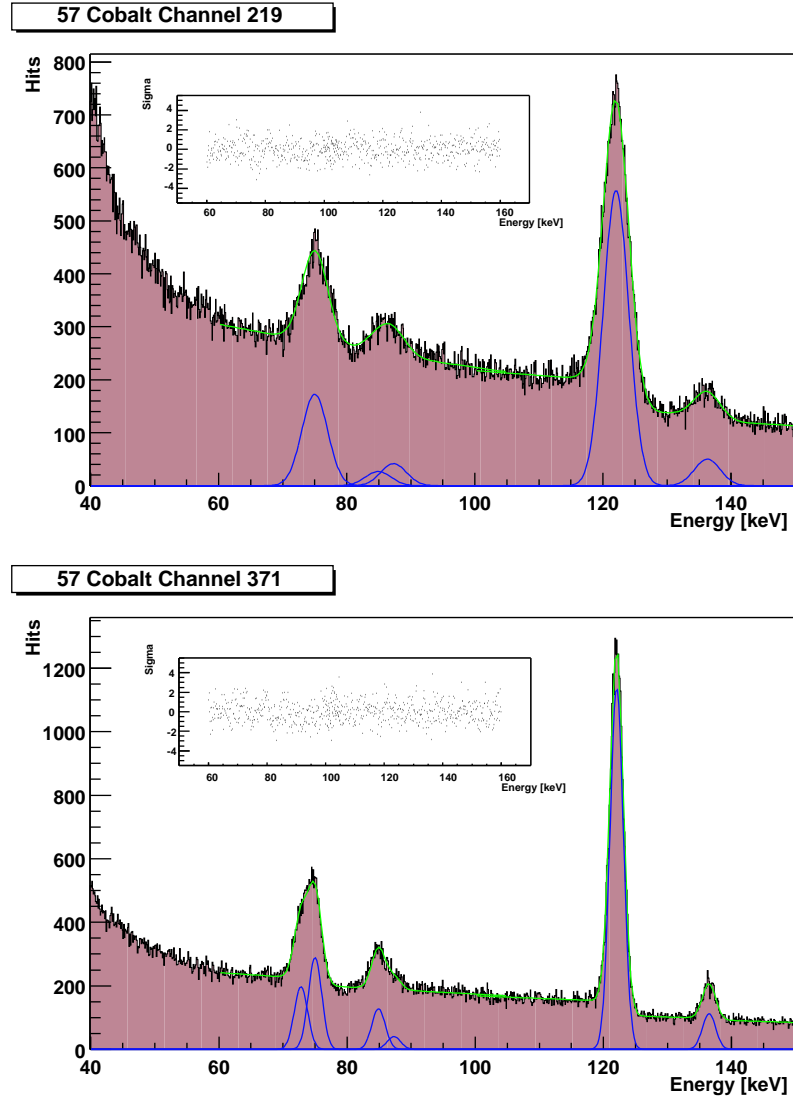


**Figure 3.3:**  $^{57}\text{Co}$  calibration run for the lithium drifted silicon detectors. The upper spectrum shows the calibration of crystal 219 the lower spectrum that of crystal 371. One can see the 122.06 and 136.47 keV lines from  $^{57}\text{Co}$  and also the  $K_{\alpha}$  and  $K_{\beta}$  lines at 75 keV and 85 keV coming from the surrounding lead shield. The small insert shows the residual for each data point from the fit in units of one standard deviation [ $\sigma$ ].

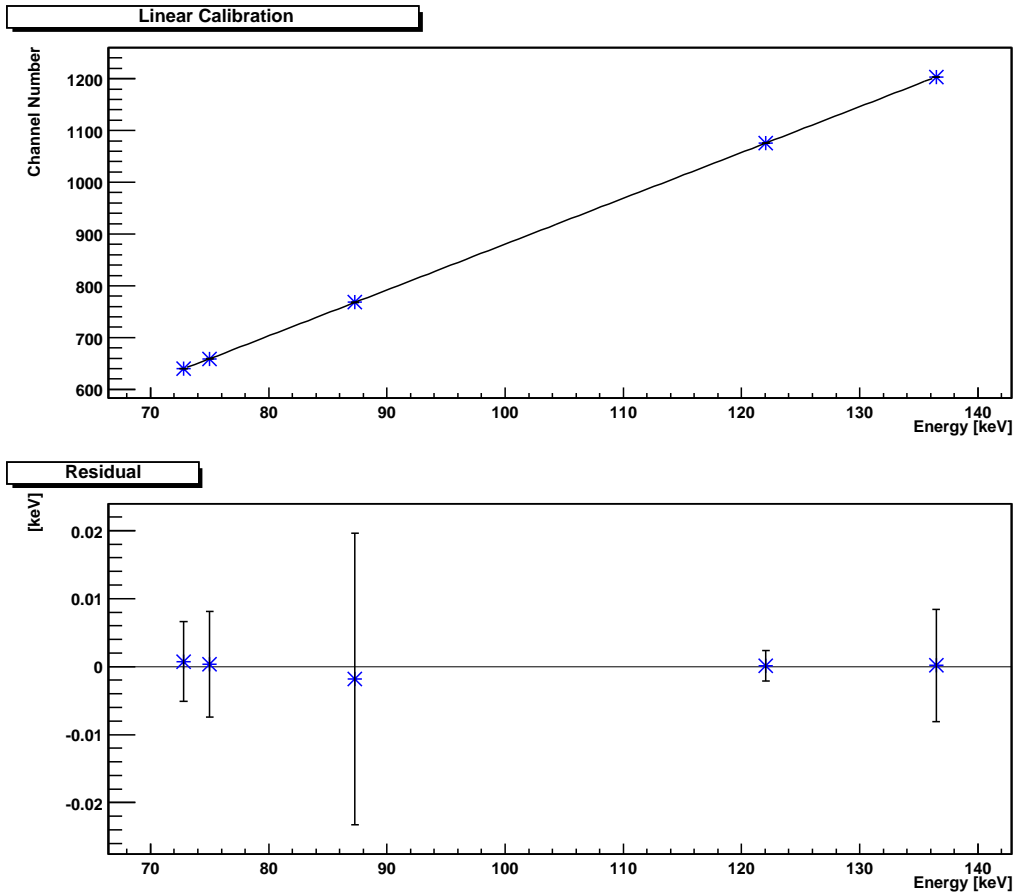


**Figure 3.4:** Linear fit of the silicon detector 219. The upper graph shows the line fit and the data points, the lower graph shows the residual and the error on the data points.

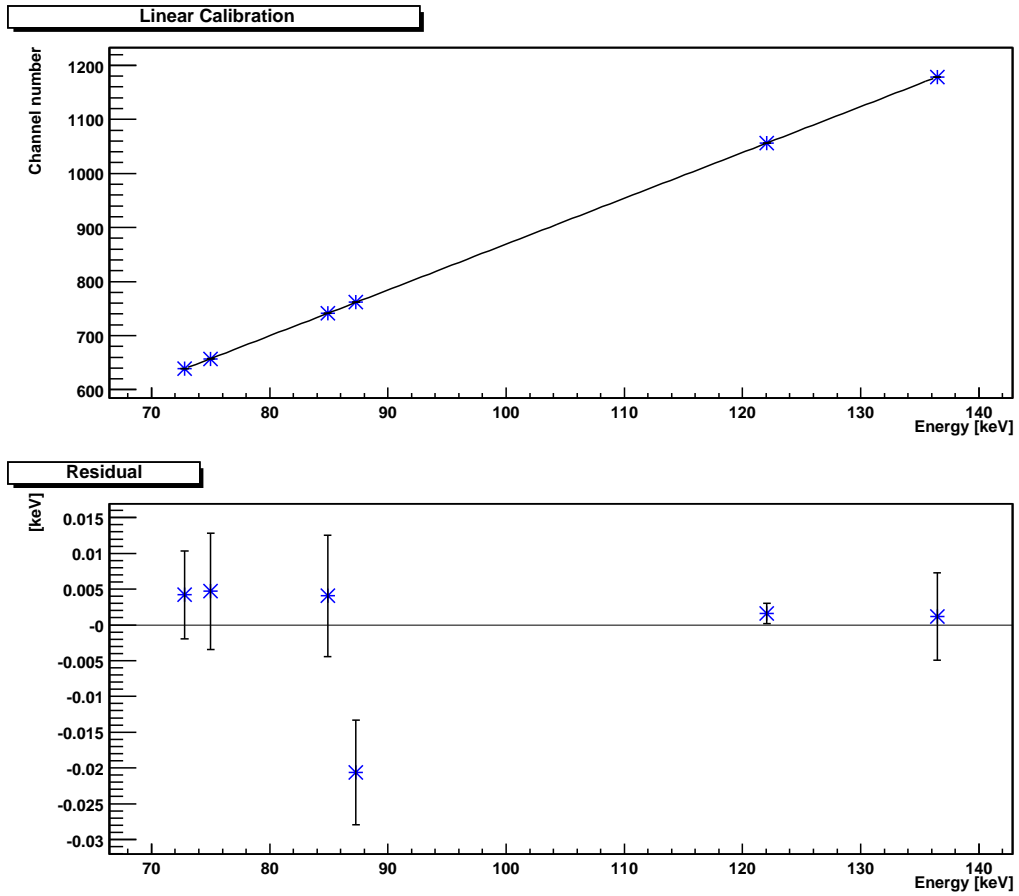


**Figure 3.5:** Linear fit of the silicon detector 371. The upper graph shows the line fit and the data points, the lower graph shows the residual and the error on the data points.

<i>Voltage [V]</i>	<i>Peak (mean) [Digits]</i>	<i>FWHM [Digits]</i>
300	3255.6	46.6
400	3255.9	43.1
500	3255.1	44.0
600	3255.3	45.8
700	3255.9	45.6
800	3255.3	44.4
900	3255.3	45.4
1000	3255.7	47.4
1100	3255.3	43.8

**Table 3.1:** Pulser peak and Full-Width-Half-Maximum (FWHM) distribution for different voltages.

<i>Shaping Time [<math>\mu</math>s]</i>	<i>Peak (mean) [Digits]</i>	<i>FWHM [Digits]</i>
0.5	2763.49	57.26
1.0	3063.59	51.88
2.0	3205.58	48.19
3.0	3255.97	45.50
6.0	3297.00	39.60
10	3383.92	38.87

**Table 3.2:** Pulser peak and Full-Width-Half-Maximum distribution for different shaping times.

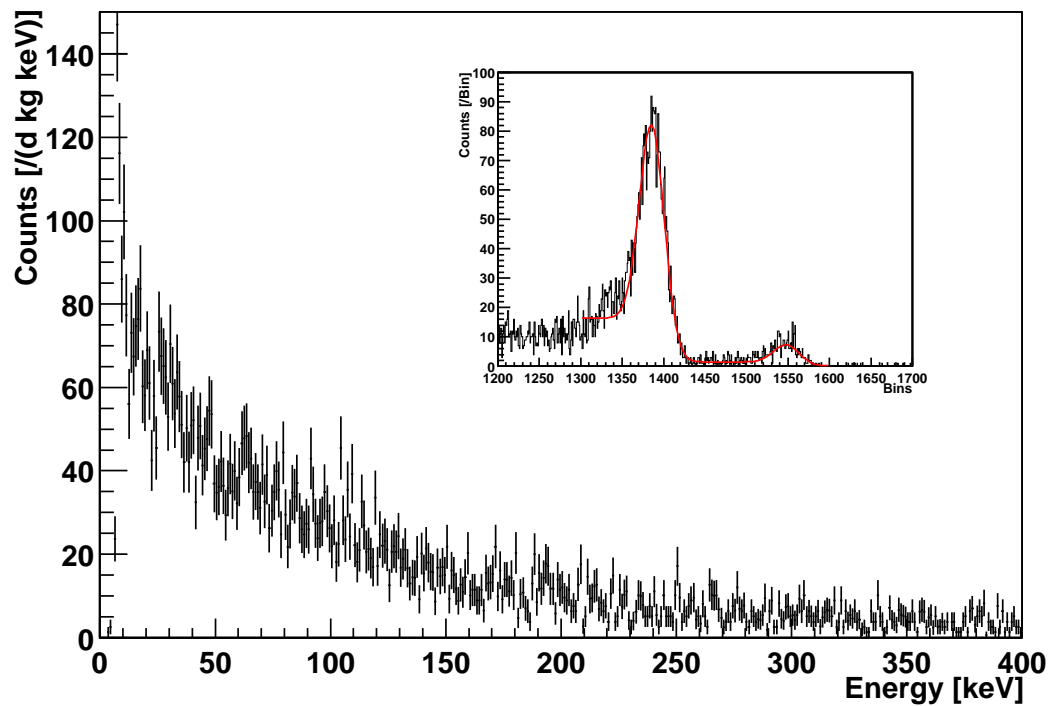
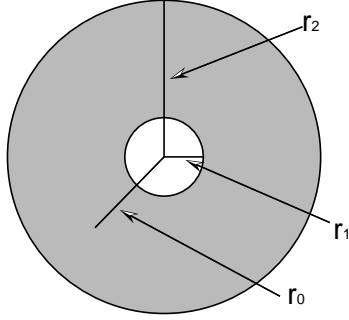


**Figure 3.6:** Underground Data from WIPP. The main plot shows the data in side the shield. The bin is normalized to counts per day per  $keV$  per  $kg$ . The threshold of the experiment can be calculated to  $8keV$ . The small insert shows the calibration data taken with a  $^{57}\text{Co}$  source.

With the notation in the figure on the left one can write the electric field  $\epsilon$  with an applied voltage  $V$  as

$$\epsilon(r) = \frac{V}{r \ln\left(\frac{r_2}{r_1}\right)}, \quad (3.1)$$



the velocities  $v_e, v_h$  of the electrons and holes are give as

$$\begin{aligned} v_e &= \mu_e \epsilon \text{ and} \\ v_h &= \mu_h \epsilon. \end{aligned} \quad (3.2)$$

With  $\mu_{e,h}$  as the mobility of the electrons/holes. Placing this into the law of motion one derives

$$\begin{aligned} \int_{r_0}^{r(t)} \frac{\ln\left(\frac{r_2}{r_1}\right) r}{\mu_{e,h} V} dr &= \int_0^t dt \text{ which integrates to} \\ t &= \frac{\ln\left(\frac{r_2}{r_1}\right) 1}{\mu_{e,h} V 2} (r(t)^2 - r_1^2) \end{aligned} \quad (3.3)$$

Using the mobility values from [KNO99] it is possible to calculate the drift time of the holes and pairs. The maximum drift time in the crystal should not exceed  $1.5 \times 10^{-7}$  seconds. Therefore the argument can be made that the pre-amplifier is the limiting factor and is responsible for the  $6 \mu s$  shaping time. The rise-time observed from the pre-amplifier varied very little and was on the order of 2-3  $\mu s$ . The fall time of the pulse was  $50 \mu s$ . The noise measured on the baseline did not exceed  $10 mV$  peak to peak before breakdown occurred in the crystal. The signal to noise ratio for a  $122.06 keV$  peak was measured to be 50/1.

To make a first calibration run a  $^{57}Co$  source at 800 volts was used with each crystal. Three minutes into the run of crystal # 636 the crystal displayed a strong increase in noise which developed from its normal level of  $10 mV$  to a level of up to  $1.5V^1$  peak to peak at the pre-amplifier output. The frequency of the data acquisition went up and finally the signal saturated the pre-amplifier output. This breakdown event occurred during a time scale of 15-20 seconds. After switching of the high voltage waiting for about 5 minutes and turning it back on, the crystal ran adequately for about 1 minute and broke down in the same manner as described above. Over time

<sup>1</sup>This compares to an energy level greater  $5 MeV$

the crystal degraded so far that it was not possible to prevent amplifier overload at voltages on the order of five volts. Several attempts to clean all the parts in the cryostat and the surface of the crystal itself were conducted. Yet positive results could not be obtained.

The spectra for the other two calibration runs are shown in Figure 3.3. The  $122.06\text{keV}$  and  $136.47\text{keV}$  from  $^{57}\text{Co}$  are easy to see. The first two peaks at  $72.5\text{keV}$  and  $84.9\text{keV}$  are due to  $K_\alpha$  and  $K_\beta$  x-rays produced by the fluorescence of the surrounding lead shield. The peaks were determined by a  $\chi^2$ -fitter that had the capability of fitting a custom generated function to the two  $^{57}\text{Co}$  peaks. The program was equipped with the ability to fit a line to the background at the left, right and in between the two peaks. The peaks themselves were simulated by Gaussians (parameters  $\mu_n$  and  $\sigma_n$ ) added over the two lines which met at the middle of the Gauss function. The fitting function therefor can be written as four functions in four different intervals:

$$\begin{aligned}
 a_1x + b_1 + \frac{1}{\sigma_1\sqrt{2\pi}}e^{-\frac{(x-\mu_1)^2}{2\sigma_1^2}} & \quad \forall \quad 0.9\mu_1 \leq x < \mu_1 \\
 a_2x + b_2 + \frac{1}{\sigma_1\sqrt{2\pi}}e^{-\frac{(x-\mu_1)^2}{2\sigma_1^2}} & \quad \forall \quad \mu_1 \leq x < \frac{\mu_1 + \mu_2}{2} \\
 a_2x + b_2 + \frac{1}{\sigma_2\sqrt{2\pi}}e^{-\frac{(x-\mu_2)^2}{2\sigma_2^2}} & \quad \forall \quad \frac{\mu_1 + \mu_2}{2} \leq x < \mu_2 \\
 a_3x + b_3 + \frac{1}{\sigma_2\sqrt{2\pi}}e^{-\frac{(x-\mu_2)^2}{2\sigma_2^2}} & \quad \forall \quad \mu_2 \leq x < 1.1\mu_2
 \end{aligned} \tag{3.4}$$

where  $x$  represents the channel numbers and the fitting parameters are  $a_n, b_n, \sigma_n$  and  $\mu_n$ . The means  $\mu_n$  of the peaks were then used for the energy calibration. The four peaks of the K-lines were fit in the same way as the two above. This time the fit was divided into eight intervals. With the following notation for a Gaussian

$$\begin{aligned}
 G(\mu, \sigma) & = \frac{1}{\sigma\sqrt{2\pi}}e^{-\frac{(x-\mu)^2}{2\sigma^2}} \text{ and} \\
 \bar{\mu}_{i,j} & = \frac{\mu_i + \mu_j}{2}
 \end{aligned} \tag{3.5}$$

one can write this fit function as

$$\begin{aligned}
 a_1x + b_1 + G(\mu_1, \sigma_1) + G(\mu_2, \sigma_1) & \quad \forall \quad 0.9\bar{\mu}_{1,2} \leq x < \bar{\mu}_{1,2} \\
 a_2x + b_2 + G(\mu_1, \sigma_1) + G(\mu_2, \sigma_1) & \quad \forall \quad \bar{\mu}_{1,2} \leq x < \frac{\bar{\mu}_{1,2} + \bar{\mu}_{3,4}}{2}
 \end{aligned}$$

$$\begin{aligned}
a_2x + b_2 + G(\mu_3, \sigma_1) + G(\mu_4, \sigma_1) &\quad \forall \quad \frac{\bar{\mu}_{1,2} + \bar{\mu}_{3,4}}{2} \leq x < \bar{\mu}_{3,4} \\
a_3x + b_3G(\mu_3, \sigma_1) + G(\mu_4, \sigma_1) &\quad \forall \quad \bar{\mu}_{3,4} \leq x < \frac{\bar{\mu}_{3,4} + \mu_5}{2} \\
a_3x + b_3G(\mu_5, \sigma_5) &\quad \forall \quad \frac{\bar{\mu}_{3,4} + \mu_5}{2} \leq x < \mu_5 \\
a_4x + b_4G(\mu_5, \sigma_5) &\quad \forall \quad \mu_5 \leq x < \frac{\mu_5 + \mu_6}{2} \\
a_4x + b_4G(\mu_6, \sigma_6) &\quad \forall \quad \frac{\mu_5 + \mu_6}{2} \leq x < \mu_6 \\
a_5x + b_5G(\mu_6, \sigma_6) &\quad \forall \quad \mu_6 \leq x < 1.1\mu_6
\end{aligned} \tag{3.6}$$

The means  $\mu_n$  of the peaks were then used for the energy calibration. The energy was calibrated linearly to the channel number. Figure 3.4 and 3.5 show the linear fit and below the data points and their residuals. After the fit was completed the residual for each bin in the histograms compared to the fit function was calculated. The small graphs inlaid in the spectrum of figure 3.3 shows the residual for the function. The units are given in standard deviations from the bin value. The table 3.3 shows the fit values of the 6 peak fitter used after the energy calibration. The

Detector number	$\mu_1$	$\mu_2$	$\mu_3$	$\mu_4$	FWHM <sub>1-4</sub>	$\mu_5$	FWHM <sub>5</sub>	$\mu_6$	FWHM <sub>6</sub>
219	72.8±0.17	75.0±0.2	84.9±0.24		4.7±0.16	122.1±0.2	4.7±0.16	136.3±0.17	4.7
371	72.8±0.17	75.0±0.19	84.9±0.22	87.3±0.17	2.4±0.13	122.1±0.2	2.4±0.13	136.5±0.12	0.24
Real	72.8	74.96	84.9	87.3		122.06		136.54	

**Table 3.3:** Fit parameter for the  $^{57}\text{Co}$  spectrum. The  $\mu_n$  represent the fitted data. The row labeled Real is the true energy of the peak. All units are in  $keV$ .

fitted means of the peaks are in very good agreement with the real data. It is visible that the resolution of crystal # 219 is a factor of two lower than crystal # 371. The 122.06 $keV$  peak of crystal # 219 has a FWHM of 3.7 $keV$  whereas crystal # 371 has one of 2.35 $keV$ . The low energy threshold at that time was limited to 13 $keV$  for crystal # 371 and 16 $keV$  for crystal # 219. It was at that point not determined whether the threshold was crystal or electronics related since the electronics used were not designed for the crystals.

### 3.3 THE THREE CRYSTAL HOLDER

For the prototype tests in the underground at the WIPP a 30l dewar from EG&G-ORTEC was used to provide the cooling for the cold-finger for a setup which held

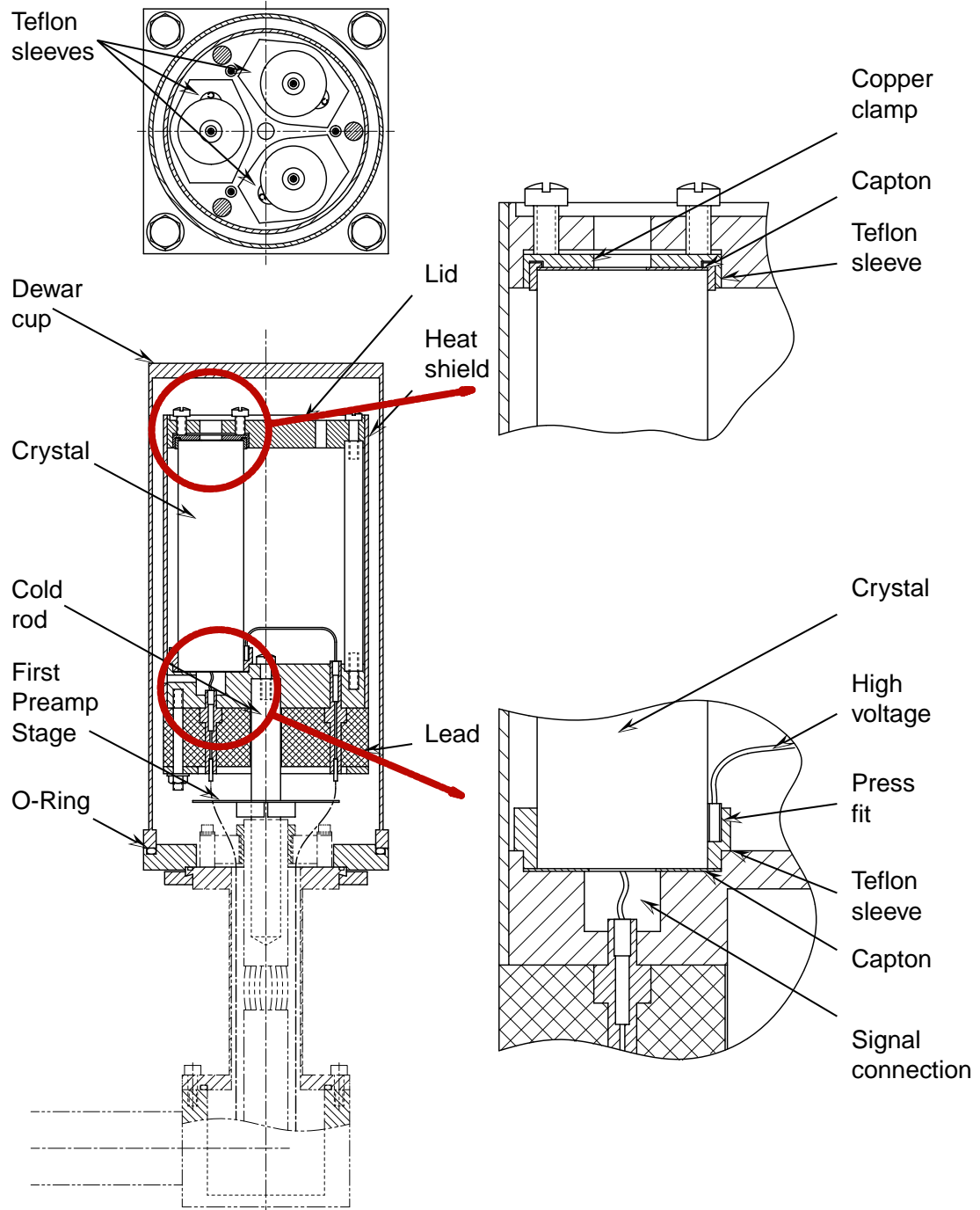
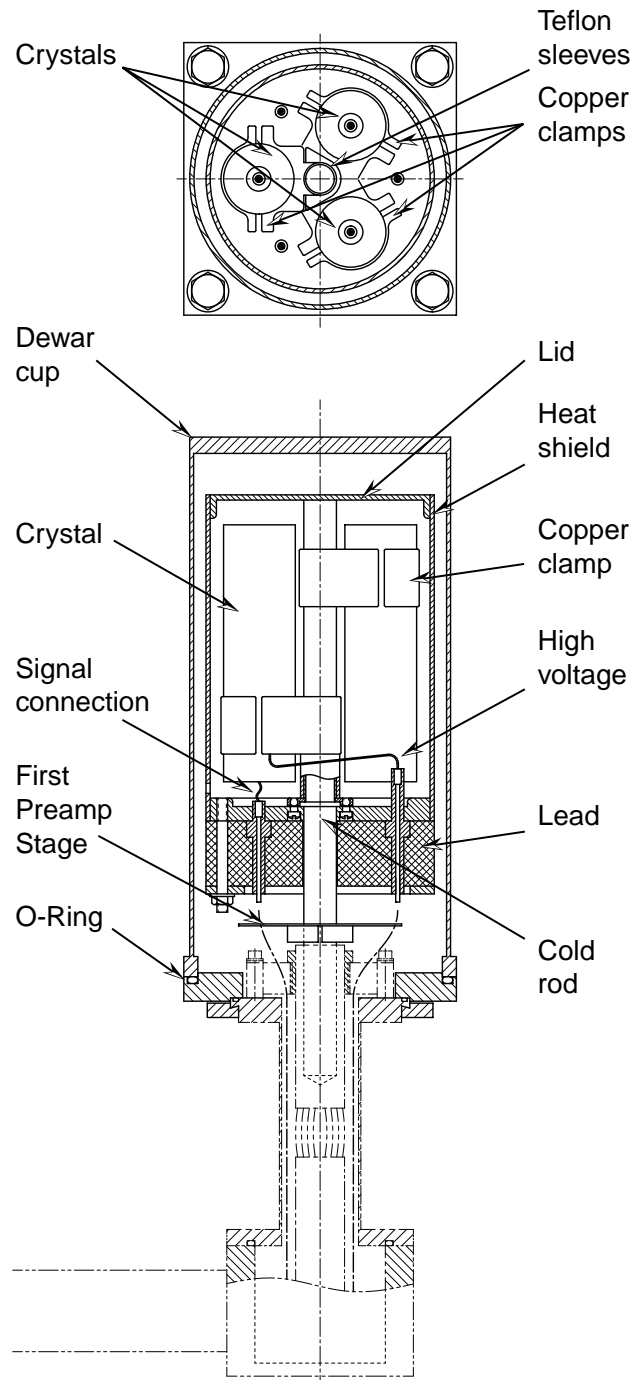
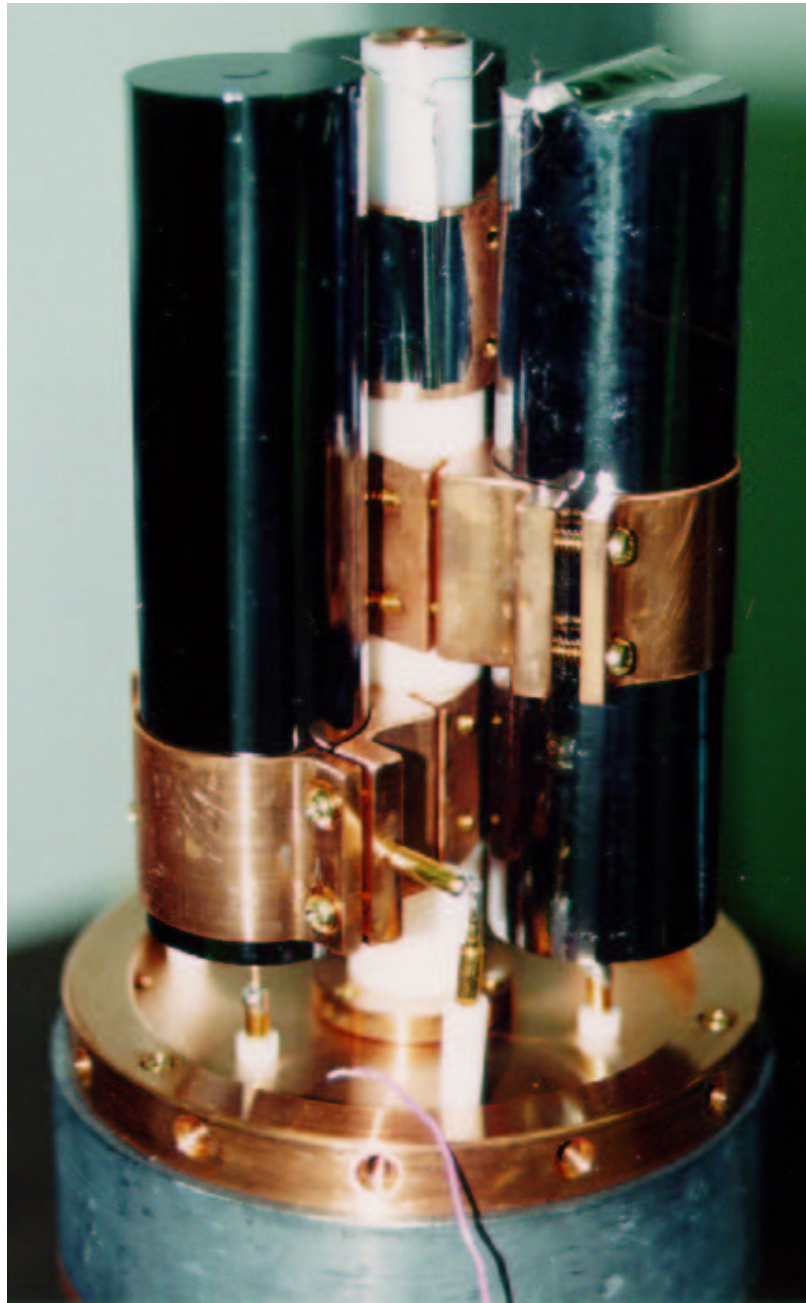


Figure 3.7: Schematic drawing of the crystal holder.



**Figure 3.8:** Schematic drawing of the crystal holder.



**Figure 3.9:** Setup of a three crystal prototype detector in a clean-room at Los Alamos National Laboratory (LANL). To determine the intrinsic contamination and the noise levels three crystals (serial numbers 219, 371 and 636) were setup in a prototype cold-finger.

all three crystals. The dewar was made by EG&G-ORTEC. It was a standard liquid nitrogen dewar with an attached cold-finger and three feed-throughs that allowed enough electrical connections to support three first stage pre-amplifiers with cooled FETs. Furthermore, the dewar was equipped with a shock absorber in the cold-finger to prevent micro-phonic noise generated by the nitrogen boil-off. The crystal holder was designed and built at Los Alamos National Laboratories. The following section is a detailed technical description of the two different holders that were constructed.

### 3.3.1 COMMON DESIGN ELEMENTS

The two different designs (see Figure 3.7 and 3.8) for the crystal holder at Los Alamos National Laboratories have common elements which are described in this paragraph. The material of choice to do the main construction was oxygen free copper. The decision for oxygen free, 101 grade copper instead of the lighter aluminum which is usually used for photon detectors due to its lower density and its small atomic weight was made because of its very low intrinsic background. As table 4.3 documents, the 101 grade copper has a factor of 23 to 400,000 less radioactive contamination than aluminum. Since there is no interest in the detection of gamma ray peaks the disadvantage of the high  $Z$  was not a high priority. The copper builds a good Faraday cage around the electronic and the crystal and at the same time provides a relatively cheap and easy-to-machine material. Unless otherwise noted the material of the part described is oxygen free 101 grade copper. The base of the holder consists of a solid cold rod which fits tightly into the cold-finger of the EG&G-ORTEC dewar. The purpose of the cold rod was to allow a good heat conduction from the crystals and detector setup to the liquid nitrogen bath. The holder itself is enclosed in a dewar cup which is vacuum tight. The seal of the dewar cup with the base plate of the cold-finger was chosen to be an O-Ring seal. The O-Ring was a butyl rubber O-ring whose contamination was expected to be more than a factor of ten lower in contamination than silicone [BOW97]. The crystals were shielded from radiative heat by a second cup built around the holding device. This way good heat flow could be achieved. The front end electronics of the pre-amplifier described in subsection 3.3.2 was mounted on a Teflon plate directly attached to the cold rod. A low background lead shield of 2 inches thickness was mounted above the electronics to prevent gamma rays originating from the cold finger, the electronics and the O-ring to enter the crystals. The high voltage and the detector signal were fed encapsulated in a Teflon sleeve through the lead.

## 3.3.2 THE FIRST STAGE OF THE PRE-AMPLIFIER

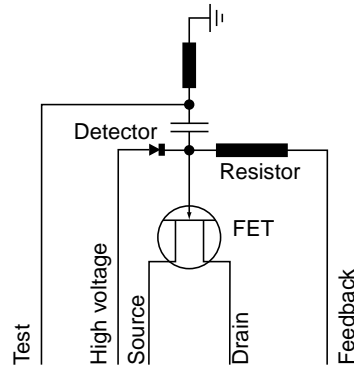


**Figure 3.10:** Schematics of front-end electronics in the dewar.

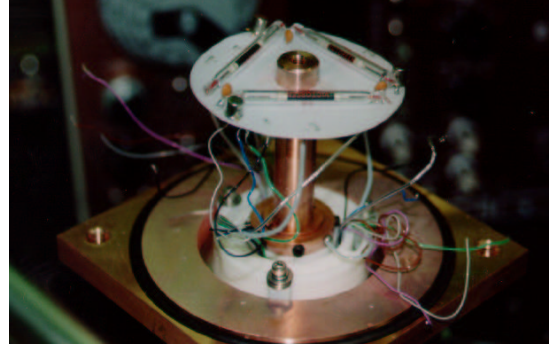


**Figure 3.11:** Picture of front-end electronics in the dewar.

To reduce electronic noise from the FET in the first stage of the 1170 EG&G-ORTEC pre-amplifier the whole first stage of the pre-amplifier was mounted on a Teflon sheet underneath the crystal-holder. This way the FET was cooled and thermal noise generated was reduced. Figure 3.10 shows the electronics diagram of the mount. Figure 3.11 shows a picture of the assembled electronics on the Teflon sheet. Teflon was chosen instead of a conventional electronics layer due to its very good vacuum properties since the electronics layer material has a strong tendency for out-gassing. The electronics for the main pre-amplifier loop consists of a FET purchased from EG&G-ORTEC (serial number SNJ132L14). The gate was connected to the detector signal and the resistor for the feedback loop of the amplifier. The resistivity of the feedback resistor was chosen to be  $10^9\Omega$  according to the specs given by EG&G-ORTEC.

A test signal was also connected to the gate of the FET. The test circuit consisted of a  $50\Omega$  resistor to ground and a capacitive coupling to the gate of the FET. This ensured the possibility to test the pre-amplifier circuit during the cold, warm and cool-down phases. Since the time for assembly, evacuation and cool-down is on the order of days, the test circuit provided a strong tool during that time period. With this configuration the pre-amplifier acts as a relatively fast integrating amplifier. The minimum integration time was  $30ns$ , the maximum integration time was  $100ns$ . The output pulse from the EG&G-ORTEC pre-amplifier had a maximum rise-time of  $100ns$ . The fall time was  $400ns$ . The maximum dynamic range observed from the pre-amplifier was 2 Volts.

### 3.3.3 FIRST HOLDER DESIGN

The design of the first crystal holder, shown in figure 3.7 was similar to the single crystal holder design and had similar holding mechanisms as commercial crystal holders. The signal connection to the crystal was made, by a tension loaded metal inserted into the connector hole at the bottom. The crystal itself sat on a thin film of capton foil inside a Teflon sleeve to isolate it against the copper holder (see magnified area of the bottom in Figure 3.7). The high voltage connection to the crystal was made by a wire with a spring loaded plug pressed against the outside of the crystal. Great care was taken to extend the possible breakdown path as much as possible by touching the surface of the crystal as little as possible. Even the copper wire carrying the high voltage for the detector was bent in a smooth curve to prevent high electric field points.

The lid for the housing of the inner cup which was used as a heat shield was mounted on top of three pillars. This way a good heat flow inside the heat shield to the lid was ensured. The detector was held in place at the top by snug fitting copper clamps. The clamps were again insulated by a capton foil and a Teflon sleeve to prevent high voltage discharge. Since the three prototype detectors differ in their length on the order of  $2mm$  the clamp construction became necessary to ensure a stable fit and a good heat flow. The silicon detector was then held in place by tightening the copper clamps.

After assembling and cooling this first design, high voltage breakdown was observed for every crystal. After warming the detector up, disassembling the holder and taking out the crystals high voltage was applied to the empty housing. The result for that test was that the high voltage did not breakdown in the supply line. With this conclusion the decision was made that the crystal had some surface contamination. An attempt to eliminate the contamination by cleaning the crystal and the copper parts in even more detail was undertaken. A new test delivered the same high voltage breakdown problem. At that point an aluminum dummy was machined to simulate the detector crystal inside the holder during room temperature and at atmospheric pressure. The dummy was not connected to the pre-amplifier circuit and high voltage was applied and the leakage current was observed at the Bertran high voltage power supply. At  $400V$  the leakage current started to increase, first slightly then faster until it tripped the internal current switch of the supply which was set to  $1\mu A$ . This observation lead to the conclusion that the high voltage was discharging through holes in the capton foil punched into the foil by dust particles collected on the capton while set under pressure to clamp the crystals. Therefore the old foil was replaced by thicker capton foil. But

even with the new capton foil the breakdown occurred. After using 5 layers of capton the breakdown was shifted to voltages above 1100V. The idea that the capton through its high static electrical field attracted dust particles out of the air which then puncture the foil when tightened to support the crystal was thereby confirmed and the conclusion to redesign the holder was drawn.

### 3.3.4 SECOND HOLDER DESIGN

To avoid the breakdown problem that occurred in the first design of the holders the second holder (see Figure 3.8) was manufactured in such a way that the crystal was only held by its high voltage connection. Since it was not known how the surface of the crystal was manufactured, whether it was ion implanted like the sides<sup>2</sup> or just passivated like the bottom, one of the design goals was to remove any contacts from the possible electric gradient bearing surfaces at the top and bottom of the crystal. The cold rod was extended to the top of the inner heat shield cup and a snug fitting Teflon sleeve for electrical insulation was pulled over the rod. The Teflon sleeve was chosen even though the radioactive contamination was with  $0.34 - 8/10 \times 10^{-5} Bq/kg$  relative high. The idea was to substitute the sleeve after the crystals were working again with three shorter sleeves that would only cover the point of contact from the copper clamps to the cold rod. Each crystal was then attached to the Teflon covered cold rod by a clamp that clamped on one side to the cold rod and on the other side held the crystal in place. The high voltage connection was made with a copper cable from the feed-through directly to the clamp. The signal cable was attached like before with a bent metal sheath under a spring load inside the connection hole. This construction left the crystal suspended free and undisturbed at its ends. To test the insulation of the holding device the aluminum dummy was instead of the crystal inserted into the holding clamp. High voltage was applied and uncovered no breakdown or increase of leakage current up to a voltage of 1500V. Thereby the conclusion was drawn that the insulation technology used in this design was working.

---

<sup>2</sup>This is usually the way commercial crystals are mounted (see also Appendix A).

### 3.4 MEASUREMENTS AT WIPP

After the second triple crystal holder was designed and it was possible to run the crystals at a voltage of 400 Volts the decision was made to bring the cryostat underground and make a first preliminary differential shielding test at the underground site at WIPP. Figure 3.8 shows a simplified yet to scale drawing of the same. The drawing shows a copper shield with a thickness of 2 inches. Due to size constraints, the lithium drifted silicon detector could only be run with one inch of copper. A picture of the cold finger and holder is displayed in Figure 3.9.

The first underground experiment was planned with different combinations of shielding material. Three different measurements were planned. The first one was a measurement with a shielding of 1 inch copper surrounded by 4 inches of lead. The second measurement added an additional layer of 4 inches of lead to the outside of the shielding. In the third measurement a layer of 2 inches of borated polyethylene was to be added to the shielding. A schematic drawing of the shielding can be seen in Figure 3.12. The different shielding materials were used to absorb the gamma ray energy from outside radioactive sources. The lead was mainly used as shielding against  $1.4MeV$  gamma rays coming from the  $^{40}K$  and the gamma contamination from U and Th chains contained in the salt at WIPP. It can also be used as a mirror for incoming fast neutrons. The copper inside was placed there to shield the detector from the low energy x-rays generated by the gamma rays in the lead.

By that time, crystal 219 and 371 revealed micro discharge and voltage breakdown at voltages higher than 400 Volts. With a voltage above 400 volts the remaining crystal would work for a short time, typically on the order of one minute, and then the noise would increase from  $10-20mV$  peak to peak, which is an equivalent energy of  $13keV$  to  $15keV$  to more than  $300mV$  ( $>350keV$ ) peak to peak with a rate greater than  $2Hz$ . Therefore the decision was made to run the crystals in the underground at a voltage of 400 Volts instead of the specified voltage of 800 Volts. That would reduce the depleted volume of the crystal by only 5%. The detector was setup underground with the maximum shielding, so that it was possible to derive the count rate of the lowest background first. One hour into the first run crystal 219 was breaking down at voltages of 400 Volts. Therefore the measurement conducted at the WIPP was made with crystal 371 only. Crystal # 371 displayed micro discharge problems at 400 Volts after running in the maximum shield configuration under high voltage for almost eight days.

Figure 3.6 shows the only data taken in the WIPP underground. The shielding consisted of 1 inch copper surrounded by 8 inches of lead. The spectrum was cal-

ibrated to the energy scale by using a  $^{57}\text{Co}$  source. The FWHM increased from the value of  $2.35\text{keV}$  at  $122\text{keV}$  to  $\sigma = 3.52\text{keV}$ . The calibration spectrum and its fit is shown as inlay inside the data spectrum. The background spectrum is histogrammed with a bin normalization of counts per  $\text{keV}$  per day per  $\text{kg}$ . The runtime of the experiment was 681492 seconds. The integrated count rate between 10 and  $100\text{keV}$  in the detector was  $6.71 \pm 0.01 \times 10^{-3}\text{Hz}$  which amounts to a count rate of  $579.7 \pm 0.9 \frac{1}{\text{kg d}}$ . This is a background rate that is similar to the measurement quoted by the crystal owners [POP97]. Since only one measurement has been made with one crystal no differential shield data is available. Therefore it is not possible to establish whether the background rate is due to intrinsic detector radioactivity or due to background penetrating and coming from the surrounding shield. The rate can also be dominated by the micro discharges that might have occurred in lower frequency during the data run. Due to the degrading of the crystal it was not possible to conduct the planned differential background measurements. The rate achieved in the measurement is much too high for a dark matter experiment. The micro discharge problem has to be solved before a more accurate background analysis or even a dark matter experiment can be conducted.

### 3.5 THE BREAKDOWN PROBLEM

To determine the nature of the breakdown problem the silicon crystal was shipped back to Los Alamos National Laboratory and set up in the weak interactions laboratory. The biasing voltage was held at the edge of micro discharge at 200 Volts. The setup was equipped with a data acquisition program that was able to record the height of the pulse and the time in  $\frac{1}{60}\text{s}$  steps from the last occurring pulse. The time interval of  $\frac{1}{60}\text{s}$  represents the shortest time interval possible to be measured with a Macintosh computer without external time processor. The reason for the use of this data acquisition was to study possible time dependencies of the breakdown effect. Figure 3.13 shows a histogram of breakdown events recorded over a time interval of 12 hours. The width of the bins are one minute. The rate is calculated as average rate in Herz for one bin. The black histogram shows the pure event rate during a 12 hour run. The red line shows the same data after cutting every event that took place within 0.3 seconds of the next event. The expected background rate from background for the silicon detector was estimated to be 1 – 2  $\text{Hz}$  which is about 10 to 30 times higher than the shielded background measured at WIPP. The average event rate during the test was  $2.87\text{Hz}$ . The experimental life

time was 12 hours. It was not possible to see a degradation of the discharge problem nor did the situation improve over time. The larger part of the breakdown events appeared to occur in bursts of events during fractions of a second rather than randomly distributed over time. The bursts itself do not follow a time pattern or frequency. They appear to be random in their generation. Figure 3.14 shows a histogram representing a zoom of the data set from Figure 3.13. The bin width in this histogram is  $\frac{1}{60}s$ . The graph shows very clearly that the noise bursts are generated in time intervals smaller than  $\frac{1}{60}s$ . In Figure 3.15 the dependency of energy and time interval is shown. It can be concluded that the noise bursts occur within small time scales, have multiple pulses and each pulse output signal height is in the regime of energy threshold to approximately  $200keV$ . This discharge problem is randomly distributed in time and the pulses are of bursting nature. It is not possible to distinguish radiation events from electrical events.

## 3.6 MODIFICATIONS AND TESTS OF THE SI-DETECTOR

### 3.6.1 VACUUM TEST

To explain the breakdown symptoms of the Si-detector at a bias voltage of 200 Volts one can pursue different theories. The possible explanations for the breakdown are: high pressure in the vacuum system, high temperature of the crystal, a surface contaminated crystal, bad contacts or a crystal in which the Lithium has drifted. Several tests to determine the cause of the breakdown were conducted.

The first test is a vacuum test to determine where the vacuum pressure inside the crystal lies. The setup for this test is shown in Figure 3.16. Valve (1) is the outlet valve of the cold-finger, valve (2) is the pump-out-port valve. Valve (3) is the valve to cut off the pump from the system. Valve (1) in the pump-out port is o-ring sealed whereas valve (2) is a copper sealed valve. Every component between valve (2) and valve (3) contains only con flat vacuum parts. This was done to minimize the risk of a leak in the outer system. Valve (2) was put into the system to be able to leak check the con-flat parts without worrying about the two o-rings in the pump-out port valve (1). To measure the pressure inside the cold-finger valve (1) is closed, valves (2) and (3) are open and the pump is running. When the pressure reaches  $10^{-6}torr$  valve (3) is closed and valve (1) is opened and a connection to the vacuum inside the cold-finger is established. This way it is possible to measure the vacuum pressure inside the detector housing and determine whether the breakdown is induced by too high a pressure or not. The known risk with this system is

valve (1). The valve and the pump-out port contain three o-ring seals. One of them is attached to a moving part. A second one is likely to be moved. The operation had to be carefully conducted and it had to be ensured that while changing the valve-status no pressure or torque was applied onto the two o-ring seals. If torque or pressure was applied, the o-ring seals could leak and the readout of the pressure inside the cold-finger was too high. This implies that the readout is just an upper limit of the pressure inside the cold-finger. The whole part from valve (1) to the pump was pumped out and baked out to a final pressure of  $5 \times 10^{-6}$  torr. Then the tightness of the upper o-ring was checked by moving the feed-through that opens valve (1) up and down. Simultaneously the pressure displayed by the ion gauge was read. The ion gauge revealed no change in the pressure readout. Finally valve (3) was closed and valve (1) to the cold dewar was opened. The pressure jumped into the  $10^{-4}$  torr region and decreased immediately down to  $2.2 \times 10^{-5}$  torr. Over two days the pressure decreased to  $6.3 \times 10^{-6}$  torr. Table 3.4 shows the times and readouts of the vacuum pressure. The value of the pressure resembles a normal vacuum value for cold-finger dewars. Since the highest risk for micro discharges lies between  $0.1\text{mbar}$  and  $1\text{mbar}$ , the pressure should be deep enough to prevent micro discharges at 1000 Volts.

Date	Time	Pressure [torr]
11/10/1999	15:49	$5 \times 10^{-6}$
11/10/1999	15:50	$\approx 10^{-4}$
11/10/1999	15:50	$4.0 \times 10^{-5}$
11/10/1999	15:54	$2.2 \times 10^{-5}$
11/11/1999	13:15	$7.5 \times 10^{-6}$
11/12/1999	13:25	$6.2 \times 10^{-6}$

**Table 3.4:** Vacuum pressure readout for the Si-detector.

### 3.6.2 TEMPERATURE TEST

To monitor the temperature of the crystals and the cryostat the cold-finger was opened and platinum resistors were installed. Two resistors<sup>3</sup> were used for this

---

<sup>3</sup>RTD 2PT100KN3027CL

task. One was mounted directly at the copper column that holds the crystals. The second one was attached to the top of the crystal itself. A third thermocouple<sup>4</sup> was mounted on the outside of the cold-finger cup to monitor the temperature drop during cool-down. Figure 3.17 shows the temperature measurements during this time period of 48 hours. After 24 hours the temperature inside the cold-finger dropped to a low of  $-165 \pm 3^\circ C$ . The outside dropped by  $3^\circ C$  from  $25^\circ C$  to  $22^\circ C$ . The detector appears to be cooled sufficiently by the liquid nitrogen.

### 3.6.3 SURFACE CONTAMINATION TESTS

Since the detector passed the vacuum and cool down tests a theory was developed that favored a surface contamination of the detector. In order to make sure the crystal was the part causing the problem and not the design of the cold finger holder (shown in Figure 3.8) each crystal was built into the single crystal holder ( see figure 3.7) and tested for breakdown. The tests demonstrated that the crystals would breakdown in the same manner in the single crystal holder as well as triple crystal holder. The holders are designed with different mechanisms to hold a crystal. The connection made to the high voltage as well as to the signal wire is in both cases of different design. Furthermore, the crystals use to work without micro discharge the first time in the single crystal holder. This strongly suggests that something happened over time with the crystals. To make sure that the cold-finger design was insulated and was not the reason for the high voltage breakdown an aluminum dummy in the shape of the crystal was designed to take its place in the holder and high voltage was applied through the dewar feed through to the aluminum block. The electronics was not connected. It was not possible to detect any leakage current which leads to the conclusion that the insulation of the detector holder does not provide a shorting path for the high voltage to ground. Since the outside of the aluminum dummy represents the outer surface of the high voltage area of the crystal, it can be concluded that the breakdown does not occur from the high voltage surface of the crystal to the grounded copper material of the cryostat. This leads to the conclusion that the breakdown occurs either over the crystal's surface or through the crystal itself to the electronics connection.

The breakdown theory assumed that the contamination contains mainly water. The idea was that remains of water were present on the surface of the crystal itself after the vacuum pumping had been done. Then, while the detector was cooled down, the water would freeze out on the surface of the crystal allowing the electri-

---

<sup>4</sup>This one was a RTD 2PT100KN3027CLA

cal field to breakdown. To out gas the water one had to bake out the crystal or etch its surface. Since the preparation and consistency of the surface was unknown the decision was made to try the out gassing method. The problem for out gassing a lithium drifted silicon detector is its low damage threshold to high temperature. Specialists at EG&G ORTEC advised not to exceed a temperature of  $60^{\circ}C$  in order to prevent the lithium from diffusing into the crystal. The crystals were reassembled in the triple crystal holder and a vacuum pump was attached to the pump-out port. When the vacuum reached its minimum of  $5 \cdot 10^{-6} torr$  the dewar was filled with water which was then heated and kept at a temperature of  $40^{\circ}C$  for about 6 months. The pressure rose to  $2 \cdot 10^{-4} torr$  and came over a period of 6 months down to  $7.5 \cdot 10^{-6} torr$  (see table 3.5). After the water was extracted from the dewar and the vacuum pump was switched off the dewar was cooled down and the detector was tested again. Micro discharges of the voltage were observed in each detector after a runtime of approximately two minutes. A more detailed analysis in which an attempt to determine the minimum breakdown voltage was conducted. Breakdown was defined as the state in which the detector generates noise at a level of  $100mV$  while under bias. The noise was observed with an oscilloscope. The time from application of bias to breakdown was recorded. The first set of measurements revealed a breakdown voltage of 330 Volts. After warming the detector up and cooling it back down the breakdown voltage was determined to be 500 Volts. The detector was then heated up and cooled down four more times and the breakdown voltage was measured. The measurement showed a breakdown voltage randomly distributed between  $280V$  and  $500V$ . The breakdown voltages are an improvement over the damaged crystal before the heating which had a breakdown voltage of less than 50 Volts. The random change could have its reason in the change of the surface properties of the crystal. With the experiments conducted, one obtains a strong case for crystal problems, possibly surface contamination. If surface contamination is the problem, a possibility to resurrect the physical properties of the crystals is to etch a thin layer off the surface. This way ridding the crystal of the contamination. Due to unresolved value and ownership questions concerning the crystals this decision is pending.

Date	Pressure [torr]	Temperature [°C]	Comment
02/10/2000	$2.1 \times 10^{-4}$	20.5	Switched pump and heater on
02/11/2000	$1.0 \times 10^{-4}$	40.0	
02/14/2000	$7.2 \times 10^{-5}$	39.8	
02/24/2000	$3.0 \times 10^{-5}$	39.9	
03/21/2000	$1.5 \times 10^{-5}$	39.7	
04/19/2000	$1.0 \times 10^{-5}$	39.6	Problems with ion gauge baking of filament
04/19/2000	$1.5 \times 10^{-4}$	39.7	After heating filament
04/19/2000	$1.2 \times 10^{-5}$	36.3	Adding water
05/01/2000	$7.5 \times 10^{-6}$	39.5	
05/10/2000	$2.6 \times 10^{-4}$	37.5	Cerro Grande Fire, 12 hours power outage
05/20/2000	not Available	39.4	Ion gauge died decision was made to continue.
06/01/2000	not Available	39.4	
06/20/2000	not Available	39.1	
07/15/2000	not Available	40.1	
08/01/2000	not Available	40.2	
09/05/2000	not Available	37.3	Added water
09/19/2000	not Available	40.3	Switched heater off
10/09/2000	not Available	20.3	Emptied water
10/19/2000	not Available	n/a	Dewar dry, disconnected from pump and cooling

**Table 3.5:** Temperature and pressure during silicon bake out phase.

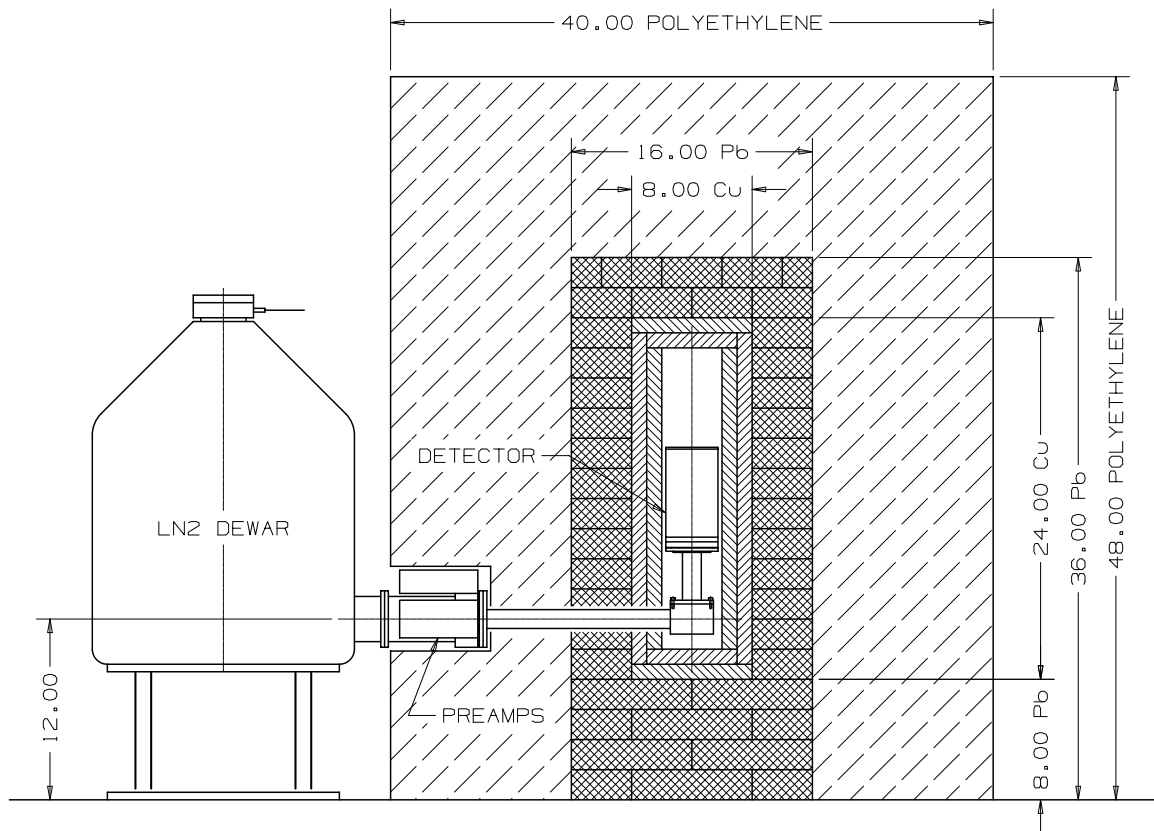


**Figure 3.12:** Design of the differential shielding. The detector was engulfed by one/two inches of copper eight inches of lead and 12 inches of wax. The wax was used to moderate neutrons, the lead to stop  $\gamma$ -rays and the copper to suppress the x-rays from the  $\gamma$ -ray induced fluorescence of the lead.

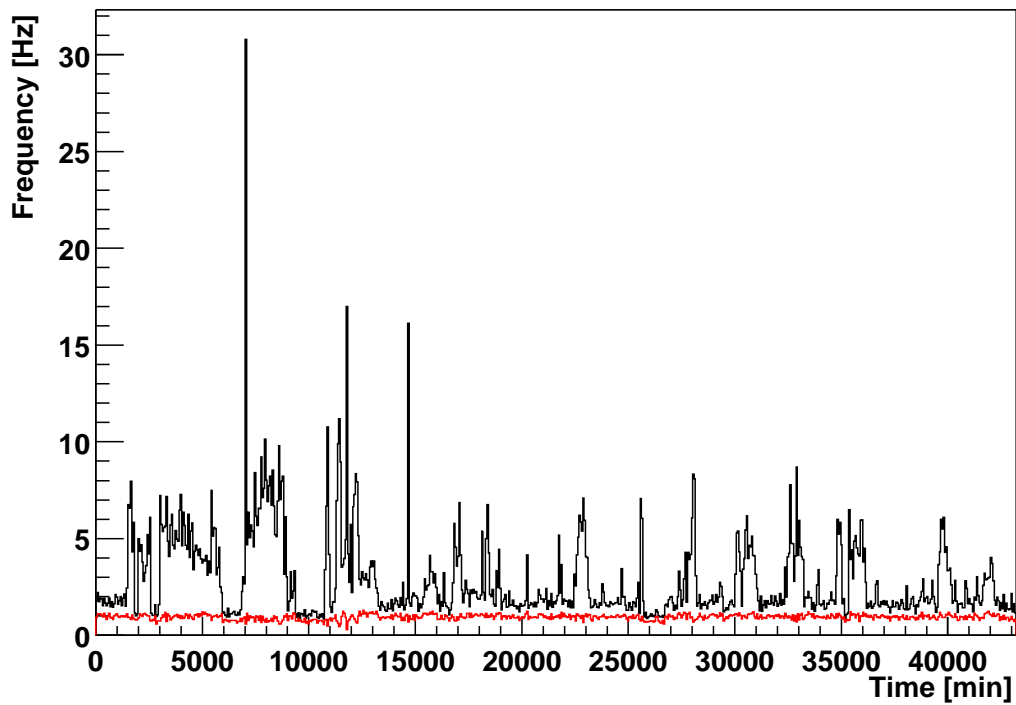


**Figure 3.13:** To determine the time characteristics of the breakdown problem an energy spectrum with time index for each event was recorded. The shortest time interval was  $\frac{1}{60} s$ . The width of the bins are one minute. The rate is calculated as average rate in  $Hz$  for one bin. The black histogram shows the pure event rate during a 12 hour run. The red line shows the same data after cutting every event that took place within 0.3 seconds of the next event.

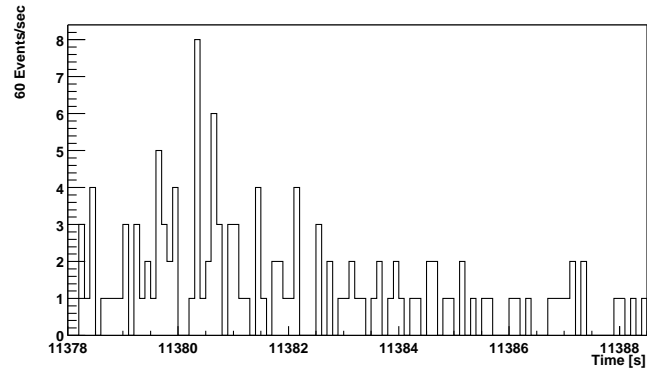


**Figure 3.14:** Zoom into a 10 second interval of a noise burst. The interval contains all occurring pulses. The bin width is  $\frac{1}{60} s$ .

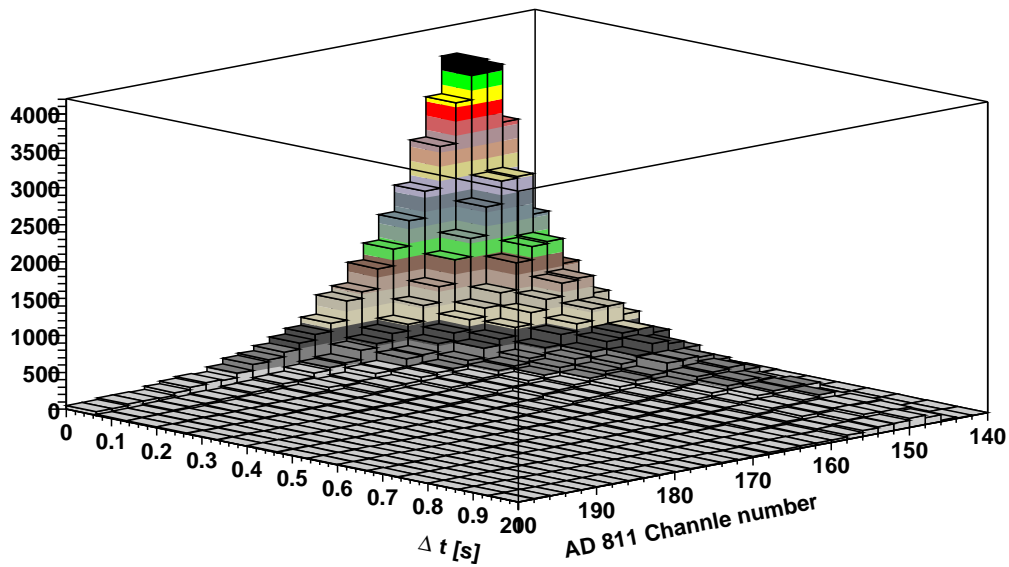


**Figure 3.15:** Events are set in a histogram according to the time difference from their neighbors in  $s$  and their ADC channel height in ADC bins.

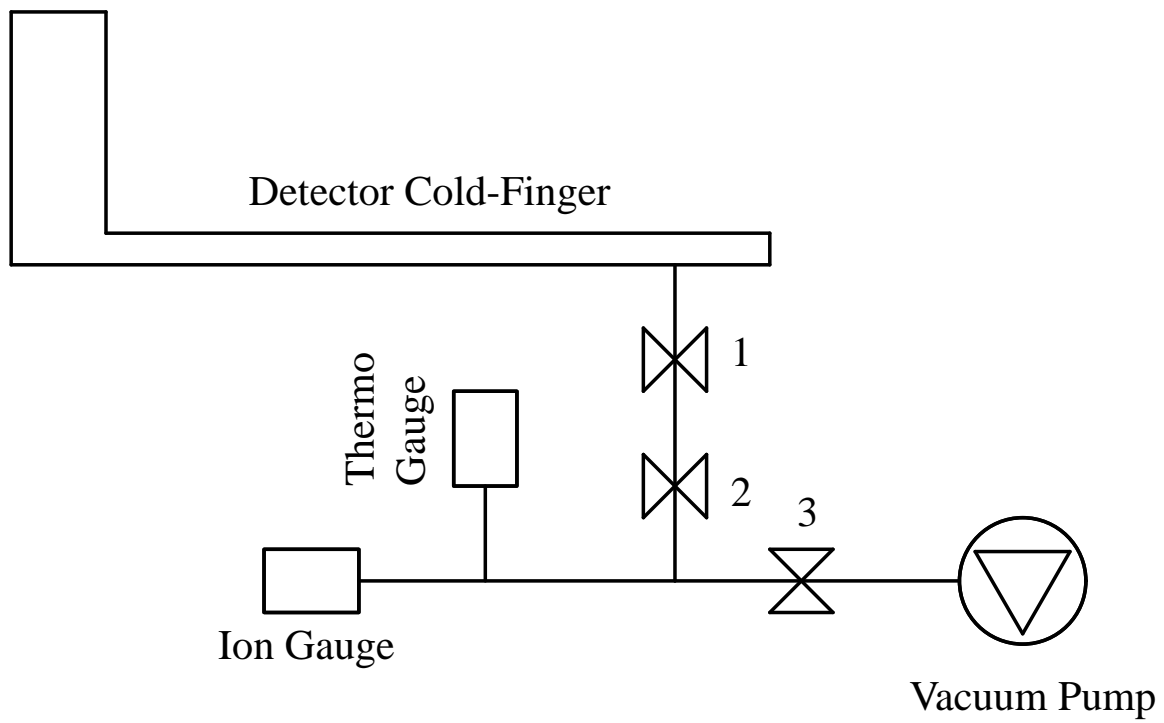
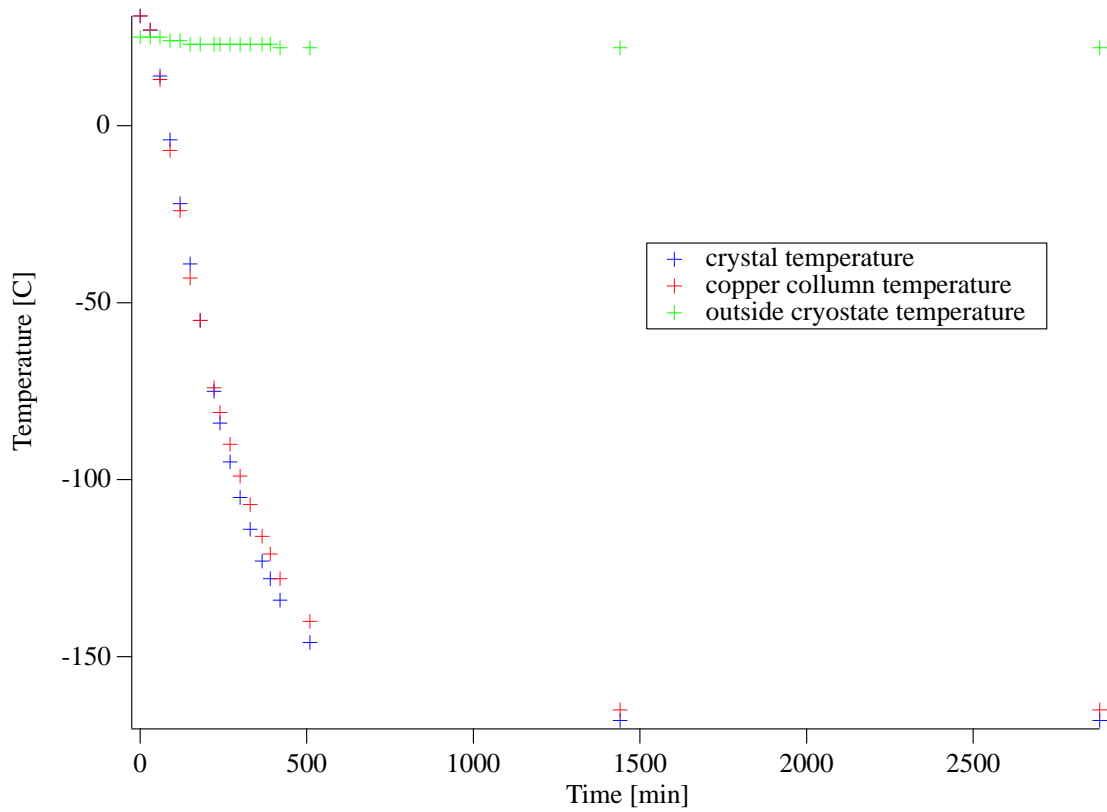


Figure 3.16: Vacuum check system for Si-detector.



**Figure 3.17:** Temperature test for Si-detector.



# BACKGROUNDS AT THE WASTE ISOLATION PILOT PLANT

---

## 4.1 BACKGROUND

To detect the very weak signal of WIMPs with a nuclear recoil event (see Section 2.1) it is necessary to shield the detector from background radiation. The background can be divided into two different classes, namely the detector intrinsic background which consists of internal radioactivity in the detector itself and the environmental background including gamma rays and neutrons produced by the surrounding environment as well as cosmic rays and their induced background.

## 4.2 INTRINSIC BACKGROUND

The intrinsic background is strongly dependent on the material used as detector and support structure. In this case a lithium drifted silicon detector was chosen (see Section 3.1). The intrinsic activity of such a detector is the main obstacle for setting a limit on WIMP interactions.

## 4.3 ENVIRONMENTAL BACKGROUNDS

### 4.3.1 PHOTON BACKGROUND

The main source for gamma rays in the environment is the natural abundance of the uranium and the thorium chains and the  $^{40}\text{K}$  decay. Figure 4.1 and 4.2 show the decay scheme of the uranium and thorium chains. The chains start with  $^{238}\text{U}$  and  $^{232}\text{Th}$ , go through a chain of  $\alpha$  and  $\beta$  decays and finally decay into the stable

isotopes of lead ( $^{208}\text{Pb}$  and  $^{206}\text{Pb}$ ). The gamma energies released during the decay are shown in table 4.1 and 4.2. In the case of isotopes with long half-lives, the daughters build up an equilibrium and decay from then on at a constant rate. The decay-chain is then in secular equilibrium. If the chain is in secular equilibrium the intensity number in the tables reflects the probability (in percent) for the gamma ray to occur during one decay process.

A second large source of gamma rays is potassium. Natural potassium contains 0.0117%  $^{40}\text{K}$  [FIR96].  $^{40}\text{K}$  decays with a probability of 89.3% in a beta decay branch and with 10.67% in an electron capture branch which subsequently emits a  $1460.83\text{keV}$  gamma ray.  $^{40}\text{K}$  has a half-life of  $1.26 \times 10^9$  years.

The radioactive concentrations vary from material to material significantly (see [FEI68], [ADA62], [FLO88], [CAM74], [BRO85]). Table 4.3 shows the radio nuclide concentration in various construction materials. Therefore it is important to choose the material that composes the detector, support structure, shielding and environment very carefully. The contamination with these elements is usually given as a relation by weight as  $\frac{\text{ng}}{\text{g}}$  or ppb, or in the units of  $\frac{\text{Bq}}{\text{kg}}$ . Equation 4.1 shows the conversion factors.

$$\begin{aligned} 1\text{Bq}\frac{^{238}\text{U}}{\text{kg}} &= 81\frac{\text{ngU}}{\text{g}}(81\text{ppbU}) \\ 1\text{Bq}\frac{^{232}\text{Th}}{\text{kg}} &= 246\frac{\text{ngTh}}{\text{g}}(246\text{ppbTh}) \\ 1\text{Bq}\frac{^{40}\text{K}}{\text{kg}} &= 32.3\frac{\text{ng}^{40}\text{K}}{\text{g}}(32.3\text{ppb}^{40}\text{K}) \end{aligned} \quad (4.1)$$

The uranium and thorium chains need not be in secular equilibrium. Both decay chains contain a radon isotope. The produced gas has the ability to migrate in solid materials. Radon is therefore the strongest natural radioactive airborne source. Since it emerges out of the earth surfaces, it is found to be concentrated in dwellings, especially basements and laboratories. Radon contamination can occur through two radon isotopes, the  $^{222}\text{Rn}$  with a half-life of 3.82 days and  $^{220}\text{Rn}$  with a half-life of 55.6 seconds. Due to the short half-life of  $^{220}\text{Rn}$  the diffusion length of the isotope is rather small. Because of that the radon contamination is mainly due to the  $^{222}\text{Rn}$  isotope. The radon contamination can be handled by sealing the detector and purging its volume with radon-free gas such as liquid nitrogen boil-off or old compressed air.

A third gamma ray source are radio nuclides produced in the atmosphere from cosmic rays. Table 4.4 shows the isotopes which have a half-life greater than one

Energy [keV]	Intensity [%]	Element	Parent	Energy [keV]	Intensity [%]	Element	Parent
92.8	2.8	<sup>234</sup> Pa	<sup>234</sup> Th	67.7	4(23)	<sup>226</sup> Ra	<sup>230</sup> Th
92.4	2.8	<sup>234</sup> Pa	<sup>234</sup> Th				
63.3	4.8	<sup>234</sup> Pa	<sup>234</sup> Th	186.1	3.5	<sup>222</sup> Rn	<sup>226</sup> Ra
964.8	5.11	<sup>228</sup> Th	<sup>228</sup> Ac	351.9	35.8	<sup>214</sup> Bi	<sup>214</sup> Pb
984.2	1.6	<sup>234</sup> U	<sup>234</sup> Pa	295.2	18.5	<sup>214</sup> Bi	<sup>214</sup> Pb
831.4	4.1	<sup>234</sup> U	<sup>234</sup> Pa	242	7.5	<sup>214</sup> Bi	<sup>214</sup> Pb
925.9	1.6	<sup>234</sup> U	<sup>234</sup> Pa	2204.2	4.86	<sup>214</sup> Po	<sup>214</sup> Bi
925.9	1.8	<sup>234</sup> U	<sup>234</sup> Pa	2118.5	1.1	<sup>214</sup> Po	<sup>214</sup> Bi
980.3	2.7	<sup>234</sup> U	<sup>234</sup> Pa	1509.2	2.1	<sup>214</sup> Po	<sup>214</sup> Bi
880.5	4.2	<sup>234</sup> U	<sup>234</sup> Pa	1407.8	2.8	<sup>214</sup> Po	<sup>214</sup> Bi
946	13.4	<sup>234</sup> U	<sup>234</sup> Pa	1401.5	1.5	<sup>214</sup> Po	<sup>214</sup> Bi
925	7.8	<sup>234</sup> U	<sup>234</sup> Pa	1281	1.4	<sup>214</sup> Po	<sup>214</sup> Bi
825.1	1.9	<sup>234</sup> U	<sup>234</sup> Pa	1847.4	2	<sup>214</sup> Po	<sup>214</sup> Bi
819.2	1.9	<sup>234</sup> U	<sup>234</sup> Pa	1238.1	5.9	<sup>214</sup> Po	<sup>214</sup> Bi
666.5	1.2	<sup>234</sup> U	<sup>234</sup> Pa	1764.5	15.4	<sup>214</sup> Po	<sup>214</sup> Bi
926.72	7.2	<sup>234</sup> U	<sup>234</sup> Pa	1155.9	1.6	<sup>214</sup> Po	<sup>214</sup> Bi
883.2	9.6	<sup>234</sup> U	<sup>234</sup> Pa	1729.6	2.9	<sup>214</sup> Po	<sup>214</sup> Bi
805.8	2.5	<sup>234</sup> U	<sup>234</sup> Pa	1120.3	14.8	<sup>214</sup> Po	<sup>214</sup> Bi
705.9	2.3	<sup>234</sup> U	<sup>234</sup> Pa	1661.3	1.1	<sup>214</sup> Po	<sup>214</sup> Bi
742.8	2.06	<sup>234</sup> U	<sup>234</sup> Pa	934.1	3	<sup>214</sup> Po	<sup>214</sup> Bi
1352.9	1.2	<sup>234</sup> U	<sup>234</sup> Pa	806.2	1.1	<sup>214</sup> Po	<sup>214</sup> Bi
569.5	8.2	<sup>234</sup> U	<sup>234</sup> Pa	1377.7	3.9	<sup>214</sup> Po	<sup>214</sup> Bi
506.5	1.3	<sup>234</sup> U	<sup>234</sup> Pa	768.4	4.8	<sup>214</sup> Po	<sup>214</sup> Bi
369.5	2.5	<sup>234</sup> U	<sup>234</sup> Pa	665.5	1.3	<sup>214</sup> Po	<sup>214</sup> Bi
458.6	1.1	<sup>234</sup> U	<sup>234</sup> Pa	609.3	44.8	<sup>214</sup> Po	<sup>214</sup> Bi
293.8	3	<sup>234</sup> U	<sup>234</sup> Pa	2447.8	1.5	<sup>214</sup> Po	<sup>214</sup> Bi
249.2	2.5	<sup>234</sup> U	<sup>234</sup> Pa				
226.5	4.2	<sup>234</sup> U	<sup>234</sup> Pa	480	2	<sup>210</sup> Pb	<sup>210</sup> Tl
898.7	3.2	<sup>234</sup> U	<sup>234</sup> Pa	2010	6.9	<sup>210</sup> Pb	<sup>210</sup> Tl
876	2.5	<sup>234</sup> U	<sup>234</sup> Pa	2430	9	<sup>210</sup> Pb	<sup>210</sup> Tl
272.3	1.1	<sup>234</sup> U	<sup>234</sup> Pa	1210	17	<sup>210</sup> Pb	<sup>210</sup> Tl
656.2	1	<sup>234</sup> U	<sup>234</sup> Pa	2360	8	<sup>210</sup> Pb	<sup>210</sup> Tl
1393.9	2.1	<sup>234</sup> U	<sup>234</sup> Pa	1590	2	<sup>210</sup> Pb	<sup>210</sup> Tl
568.9	3.6	<sup>234</sup> U	<sup>234</sup> Pa	2270	3	<sup>210</sup> Pb	<sup>210</sup> Tl
372	1.2	<sup>234</sup> U	<sup>234</sup> Pa	860	6.9	<sup>210</sup> Pb	<sup>210</sup> Tl
738	1.2	<sup>234</sup> U	<sup>234</sup> Pa	1316	21	<sup>210</sup> Pb	<sup>210</sup> Tl
692.6	1.2	<sup>234</sup> U	<sup>234</sup> Pa	1410	4.9	<sup>210</sup> Pb	<sup>210</sup> Tl
796.1	2.5	<sup>234</sup> U	<sup>234</sup> Pa	1110	6.9	<sup>210</sup> Pb	<sup>210</sup> Tl
755	1.2	<sup>234</sup> U	<sup>234</sup> Pa	1070	12	<sup>210</sup> Pb	<sup>210</sup> Tl
227.3	5.8	<sup>234</sup> U	<sup>234</sup> Pa	80	20	<sup>210</sup> Pb	<sup>210</sup> Tl
186.15	1.8	<sup>234</sup> U	<sup>234</sup> Pa	97.9	4	<sup>210</sup> Pb	<sup>210</sup> Tl
733.4	6.9	<sup>234</sup> U	<sup>234</sup> Pa	298	79	<sup>210</sup> Pb	<sup>210</sup> Tl
				799.7	99	<sup>210</sup> Pb	<sup>210</sup> Tl
53.2	12(28)	<sup>230</sup> Th	<sup>234</sup> U				
				46.5	4.25	<sup>210</sup> Bi	<sup>210</sup> Pb

Table 4.1: Gamma rays produced by the uranium chain.

# Decay of <sup>238</sup>U to <sup>206</sup>Pb

Alpha Lines			
	KeV	%	Level
<sup>238</sup> U	4.196	77	0
	4.149	23	50
<sup>234</sup> U	4.777	72	0
	4.723	28	53
<sup>230</sup> Th	4.688	76.3	0
	4.621	23.4	67
<sup>226</sup> Ra	4.784	94.5	0
	4.602	5.5	186
<sup>222</sup> Rn	5.490	99.9	0
<sup>218</sup> Po	6.002	99+	0
<sup>214</sup> Po	7.687	99.9	0
<sup>210</sup> Po	5.305	99+	0

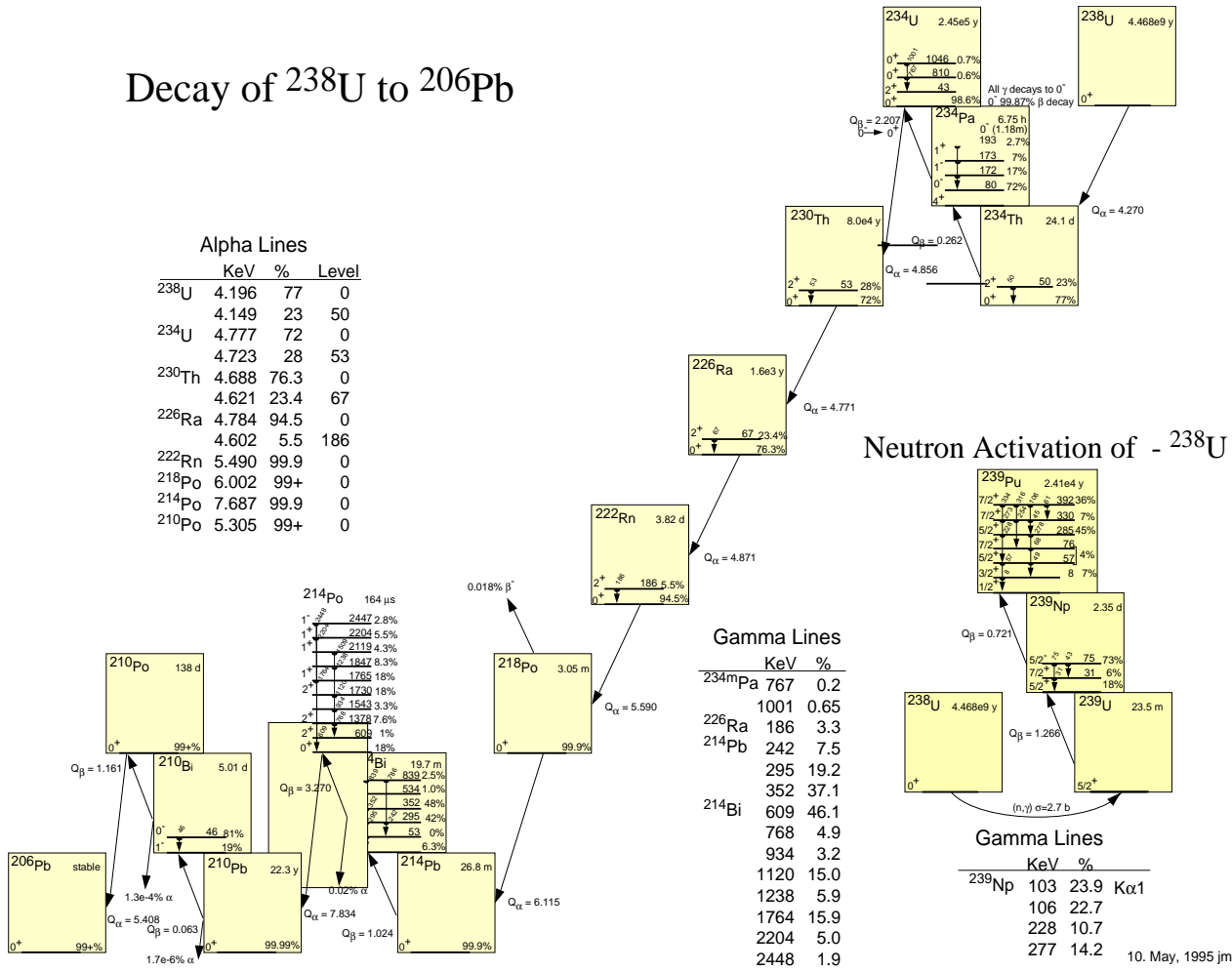


Figure 4.1: <sup>238</sup>U decay chain from [WOU99].

10. May, 1995 jmw

# Decay of $^{232}\text{Th}$ to $^{208}\text{Pb}$

Alpha Lines

	KeV	%	Level
$^{232}\text{Th}$	4.011	77	0
	3.957	23	59
$^{228}\text{Th}$	5.423	72.7	0
	5.340	26.7	85
$^{224}\text{Ra}$	5.686	95.0	0
	5.449	5.0	241
$^{220}\text{Rn}$	6.288	99.9	0
$^{216}\text{Po}$	6.778	99+	0
$^{212}\text{Bi}$	6.090	27.2	0
	6.051	69.9	40
$^{212}\text{Po}$	8.785	??	0

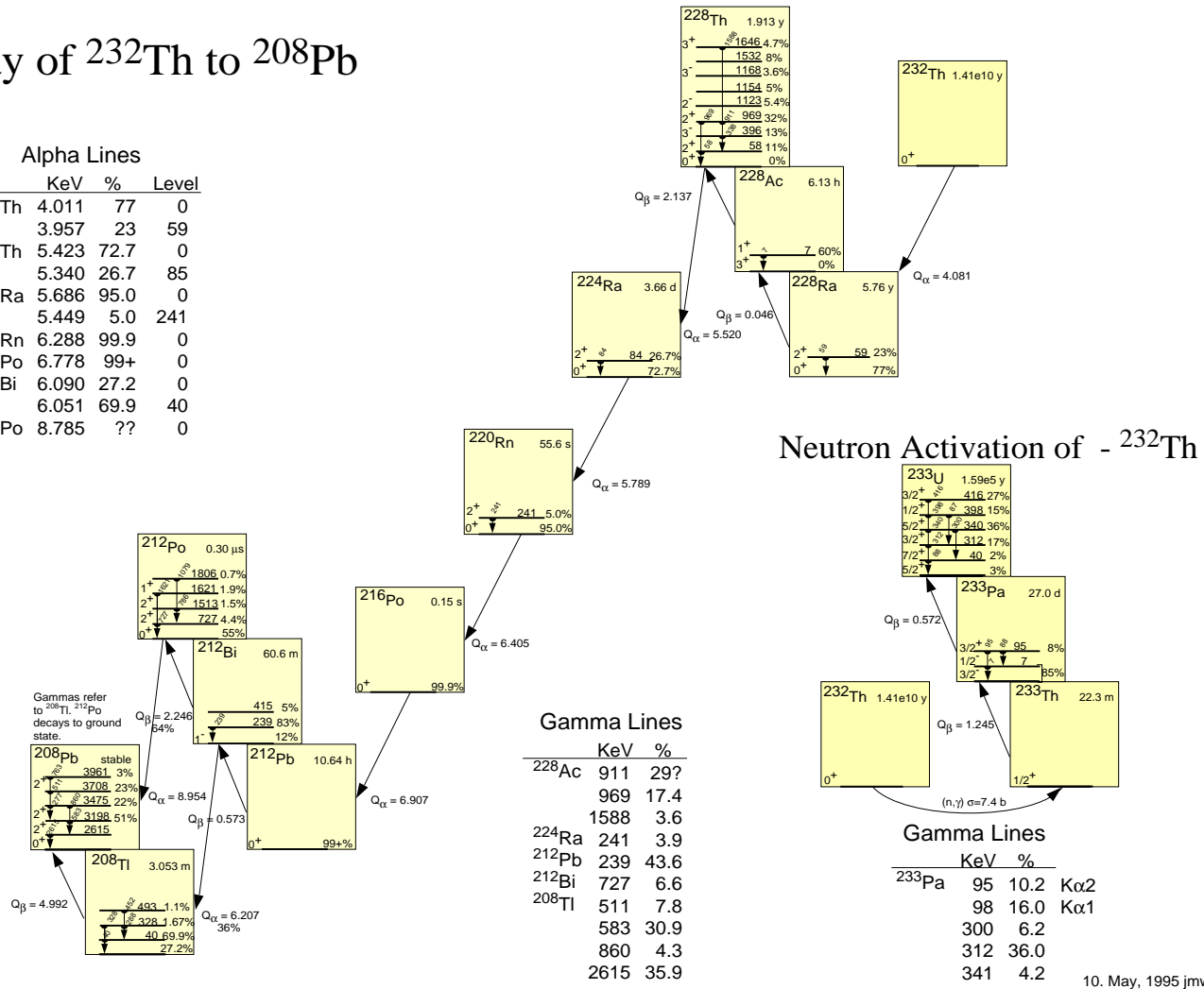


Figure 4.2:  $^{232}\text{Th}$  decay chain from [WOU99].

Energy [keV]	Intensity [%]	Element	Parent	Energy [keV]	Intensity [%]	Element	Parent
6.67		<sup>228</sup> Ac	<sup>228</sup> Ra				
				240.9	4	<sup>220</sup> Rn	<sup>224</sup> Ra
794.9	4.3	<sup>228</sup> Th	<sup>228</sup> Ac				
964.8	5.11	<sup>228</sup> Th	<sup>228</sup> Ac	300	3.3	<sup>212</sup> Bi	<sup>212</sup> Pb
835.7	1.7	<sup>228</sup> Th	<sup>228</sup> Ac	238.6	43.3	<sup>212</sup> Bi	<sup>212</sup> Pb
969	16.2	<sup>228</sup> Th	<sup>228</sup> Ac				
911.2	26.6	<sup>228</sup> Th	<sup>228</sup> Ac	1620.5	1.5	<sup>212</sup> Po	<sup>208</sup> Pb
338.3	11.3	<sup>228</sup> Th	<sup>228</sup> Ac	727.3	6.5	<sup>212</sup> Po	<sup>208</sup> Pb
209.2	3.8	<sup>228</sup> Th	<sup>228</sup> Ac	785.3	1.1	<sup>212</sup> Po	<sup>208</sup> Pb
327.9	2.9	<sup>228</sup> Th	<sup>228</sup> Ac				
270.4	3.4	<sup>228</sup> Th	<sup>228</sup> Ac	328		<sup>208</sup> Tl	<sup>212</sup> Bi
129.1	2.45	<sup>228</sup> Th	<sup>228</sup> Ac	288		<sup>208</sup> Tl	<sup>212</sup> Bi
409.5	1.9	<sup>228</sup> Th	<sup>228</sup> Ac	39.9		<sup>208</sup> Tl	<sup>212</sup> Bi
463	4.4	<sup>228</sup> Th	<sup>228</sup> Ac				
755.3	1	<sup>228</sup> Th	<sup>228</sup> Ac	763.13	1.8	<sup>208</sup> Tl	<sup>208</sup> Pb
1630.6	1.6	<sup>228</sup> Th	<sup>228</sup> Ac	510.8	22.6	<sup>208</sup> Tl	<sup>208</sup> Pb
1588.2	3.3	<sup>228</sup> Th	<sup>228</sup> Ac	860.6	12.4	<sup>208</sup> Tl	<sup>208</sup> Pb
				277.4	6.3	<sup>208</sup> Tl	<sup>208</sup> Pb
84.4	1.2	<sup>224</sup> Ra	<sup>228</sup> Th	2614.5	99	<sup>208</sup> Tl	<sup>208</sup> Pb

**Table 4.2:** Gamma rays produced by the thorium chain.

day. Column 3 shows the target nuclei which are responsible for the production of the isotope. Since argon is in rather small abundance in the atmosphere, only the isotopes generated from nitrogen and oxygen are of importance. The table was taken from [LAL67]. Man made radioactivity from nuclear testing and major reactor accidents such as Tchernobyl can also contribute to the gamma background. Levels of <sup>3</sup>H, <sup>14</sup>C, <sup>90</sup>Sr and <sup>137</sup>Cs have increased due to these events and can become a significant source of background in low background experiments. The first three of these isotopes are pure beta decay isotopes and can be shielded easily as long as they are not contributing to the intrinsic background of the detector. The fourth isotope (<sup>137</sup>Cs) also emits a gamma ray with an energy of 661.66keV and provides an external background to be shielded.

### 4.3.2 NEUTRON BACKGROUND

Neutron background is generated by four different processes. The production processes are ( $\alpha,n$ )-reactions, fission, the hadronic component of cosmic rays and the production through muons. Each component is dependent on the depth of the experiment. Figure 4.3 shows neutron fluxes for the different sources as a function of depth.

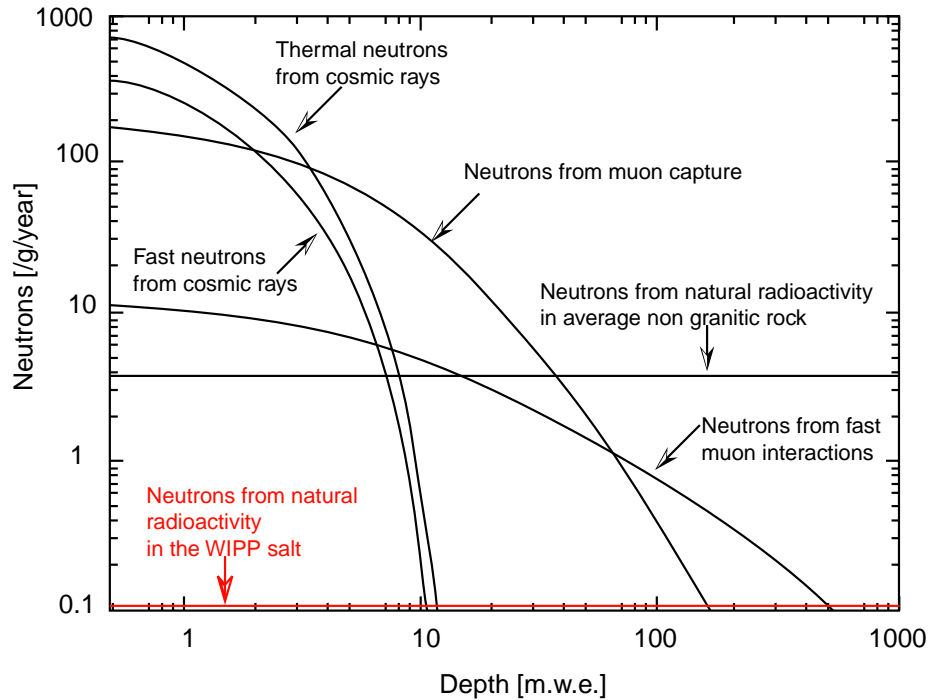


**Figure 4.3:** Neutron flux for different neutron sources. The cosmic ray data are from [LAL67]. The data for  $(\alpha,n)$  are taken from [FLO88] and from [BEZ73]. The data for the WIPP salt origins from [WEB98]. The depth is shown in meters water equivalent or hectogram per gram.

#### NEUTRONS FROM $(\alpha,N)$ -REACTIONS AND FISSION

Uranium and thorium can be found as impurities in all materials including geological formations. The abundance of these elements is responsible for the generation of the intensity of the neutron flux in the material. The highest energy  $\alpha$ -particle in the uranium and thorium decay has an energy of  $8.78\text{MeV}$  and originates from the decay of  $^{212}\text{Po}$  in the thorium chain. The threshold energy of the  $(\alpha,n)$  reaction in  $^{16}\text{O}$ ,  $^{28}\text{Si}$  and  $^{40}\text{Ca}$ , which make up more than 79% of the earth crust, is much higher. Therefore an  $(\alpha,n)$ -reaction can only occur with elements like Na and Al. This means the consistency of the rock plays a significant role in the determination of the neutron flux. Table 4.5 from [FLO88] shows the fluxes generated by different rocks. Table 4.21 shows the Uranium and Thorium contaminations in the WIPP salt.

Uranium and thorium also have the ability to undergo a spontaneous fission process. The rate of neutrons emitted from 1kg of natural uranium are estimated by several authors such as [FLO88] and [BEZ73] as  $\approx 16 \frac{\text{neutrons}}{\text{kg s}}$ , which converts to a neutron production rate of  $2000 \frac{\text{neutrons}}{\text{y}}$  in 1kg of rock with an impurity of 1ppm. The neutron production from the fission of Th can be neglected since the half-life is much larger than the half-lives for U. The half-lives are:

$$\begin{aligned} T_{1/2} \text{ fission}(^{238}\text{U}) &= 1.01 \times 10^{16} a \\ T_{1/2} \text{ fission}(^{235}\text{U}) &= 1.8 \times 10^{17} a \\ T_{1/2} \text{ fission}(^{232}\text{Th}) &= 5 \times 10^{19} a \end{aligned} \quad (4.2)$$

These equations show that the neutrons generated by fission are negligible relative to  $(\alpha, n)$  reactions.

#### NEUTRONS FROM THE HADRONIC COMPONENT OF COSMIC RAYS

Figure 4.3 shows that the neutrons from the hadronic components generate the largest background for experiments at shallow depths. However, if the experiment exceeds a depth of more than 10 m.w.e. (meters water equivalent) the contribution falls by 4 orders of magnitude and other backgrounds are of higher importance, namely neutrons from natural radioactivity and cosmic ray interactions.

#### NEUTRONS FROM MUONS

Muons can interact in two different ways with the target nucleus. They can either interact directly through their electromagnetic field with the nuclei or through photo-nuclear interaction of real photons contained in showers. The photons are generated by  $\delta$  electrons, pair annihilation and bremsstrahlung produced in the showers. Slow muons with negative charge can be captured by the target nucleus and be forced onto a Bohr orbital. In the orbital, they cascade very fast ( $\approx 10^{-11} s$ ) and can either decay as

$$\mu^- \longrightarrow e^- + \bar{\nu}_e + \nu_\mu \quad (4.3)$$

or be captured by the nucleus and transform a proton into a neutron

$$\mu^- + p \longrightarrow n + \nu_\mu. \quad (4.4)$$

Once the muon is captured and the neutron is produced, the nucleus has two branches to emit the energy. One possibility is for the created neutron to be directly emitted without further interactions with the remaining nucleons. The probability for this reaction decreases for increasing nucleus mass. The reaction creates neutrons varying in energy from a few  $1MeV - 2MeV$  to  $40MeV - 50MeV$ . The branching ratio for this interaction lies between 8% and 25%. As Singer shows in [SIN74] the energy distribution is proportional to an exponential

$$\frac{dN(E)}{dE} \sim e^{-\frac{E}{E_0}} \quad (4.5)$$

where the constant  $E_0$  has been experimentally measured ([KRI69], [SCH71]) and its value for different materials lies between  $7MeV$  and  $15MeV$ . The majority of the muons generate the neutron inside the nucleus and the energy generated is shared with the nucleons. The nucleus boils off several low energy neutrons. This process is called neutron evaporation. The evaporation spectrum can be written as [SIN74]

$$\frac{dN(E)}{dE} \sim \left( \frac{E}{1 MeV} \right)^{\frac{5}{11}} e^{-\frac{E}{\Theta}}. \quad (4.6)$$

$E$  is the energy of the emitted neutron in  $MeV$ ,  $\Theta$  is the nuclear temperature and typically has the order  $1MeV$ .  $\Theta$  decreases slightly with increasing mass of the target nucleus. To determine the neutron flux from capture, one can write [SIN62]

$$\Phi_{\mu^-} = \frac{d\Phi_{\mu stop}}{dh} \Delta_{\mu^-} f_c f_n. \quad (4.7)$$

$\frac{d\Phi_{\mu stop}}{dh}$  is the stopping rate of muons at a certain depth  $h$  measured in *m.w.e.* and can be achieved from [MIY73].  $\Delta_{\mu^-} = \frac{\mu^-}{\mu^- + \mu^+}$  and represents the charge ratio for muons at that depth (see [GON85]).  $f_c$  represents the capture ratio for a muon and  $f_n$  the multiplicity factors for the neutrons. The multiplicity factor  $f_n$  for some materials derived from MacDonald's Experiment [MCD65] are displayed in table 4.6. A detailed comparison with the theory from [SIN62] can be found in [SIN74]. The number of neutrons produced by muons at a certain depth has been measured and extrapolated by Bezrukov [BEZ73]. Figure 4.4 displays the overall number of neutrons generated by one muon in  $\frac{g}{cm^2}$  dependent upon the depth in *m.w.e.*

### 4.3.3 COSMIC RAY BACKGROUND

The cosmic ray background consists of several different particles such as muons, pions, electrons, protons, etc. They are coming either from space or are generated in reactions in the high atmosphere. The most numerous particles in this flux are the muons generated in the atmosphere by cosmic protons hitting atoms in the air producing pions and muons. They are also the major component of the cosmic ray flux to be detected underground. The largest fraction of the muons are produced in the atmosphere about  $15\text{km}$  high and lose on their way down to sea level an average of  $2\text{GeV}$ . At sea level the overall angular distribution of muons is approximately  $\cos^2 \Theta$ . The vertical intensity of muons integrated above  $1\text{GeV}$  is  $\approx 70 \text{ m}^{-2}\text{s}^{-1}\text{sr}^{-1}$  or roughly  $1\text{cm}^{-2}\text{min}^{-1}$  [PAS93], [ALL97]. The energy spectrum for vertical muons is described by the empirically fit formula developed by De et. al. [DEK72] (see also [WOL73]):

$$\begin{aligned} N(P)dP &= AP^{-\alpha} dP \text{ with} & (4.8) \\ \alpha &= 0.5483 + 0.3977 \ln P \text{ and} \\ A &= 3.09 \times 10^{-3} \text{cm}^{-2}\text{s}^{-1}\text{sr}^{-1}(\text{GeV}/c)^{-1}, \end{aligned}$$

where  $P$  is the momentum in  $\text{GeV}/c$ . Figure 4.5 shows this spectrum. Since the muon spectrum shifts in intensity and peak position for larger angle, the spectrum in figure 4.5 can only be used in an energy range up to  $10\text{GeV}/c$  and for steep angular incidence. For higher energies and larger angles the spectrum intensity can be written as [RAS84]

$$\frac{dN_\mu}{dE_\mu} = \frac{0.14 E_\mu^{-2.7}}{\text{cm}^2 \text{ s sr GeV}} \times \left\{ \frac{1}{1 + \frac{1.1 E_\mu \cos \Theta}{115 \text{ GeV}}} + \frac{0.054}{1 + \frac{1.1 E_\mu \cos \Theta}{850 \text{ GeV}}} \right\}. \quad (4.9)$$

Here  $E_\mu$  is the energy of the muon and  $\Theta$  represents the incident angle of the muon. Muons are able to penetrate the earth to a significant depth. They are able to traverse through rock and other materials to a great depth due to their high energy. They lose energy mainly by ionization but also by the radiative processes of bremsstrahlung, pair production and photo nuclear interactions. One can calculate the average energy loss for a muon and traversing through matter by aid of the following formula:

$$-\frac{dE_\mu}{dX} = a + bE_\mu. \quad (4.10)$$

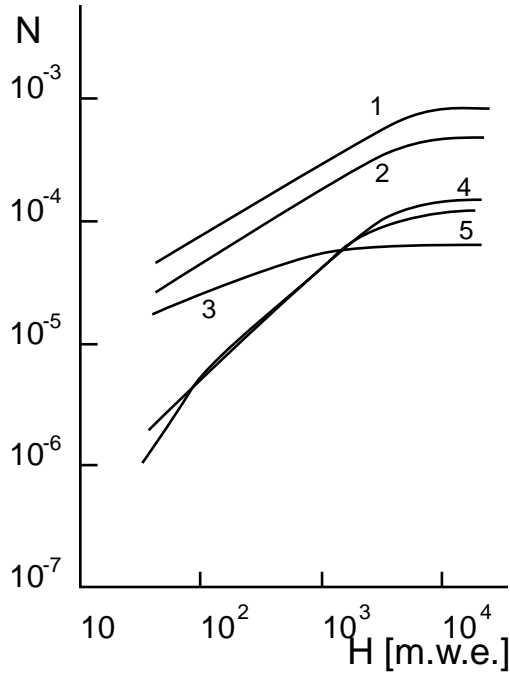


**Figure 4.4:** Neutrons created per muon at a certain depth in [ $\frac{hg}{cm^2}$ ]. 1. total neutron generation. 2. neutrons produced by virtual photons. 3-5 neutrons from cascades generated by  $\delta$  electrons, pair annihilation and bremsstrahlung.

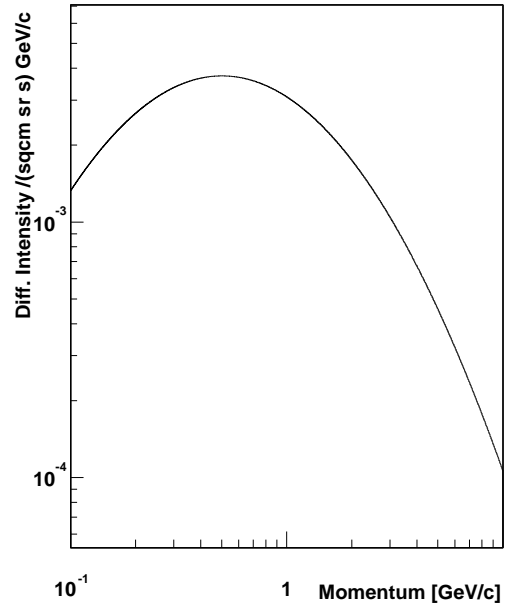


**Figure 4.5:** Differential muon intensity versus muon momentum. The spectrum is an empirical fit of the momentum distribution of vertical muons at sea level. The empirical fit was done by [DEK72]. The spectrum has a flat maximum at about 0.5 GeV/c.

$E_\mu$  is again the energy of the muon,  $X$  is the depth of the penetration. Here  $a$  represents the ionization loss and  $b$  the fractional energy loss due to the three radiation processes. The parameters  $a$  and  $b$  are functions of energy. Table 4.7 shows the average muon range  $R$  with a certain energy in standard rock together with the different  $b$ -parameters. With the energy spectrum from the surface in equation 4.9 and equation 4.10 it is possible to calculate the energy  $E_\mu$  of a muon that started at the surface with the energy  $E_{\mu,0}$  at a certain depth  $X$ :

$$E_\mu = (E_{\mu,0} + \epsilon)e^{-bX} - \epsilon, \text{ where} \quad (4.11)$$

$$\epsilon = \frac{a}{b}.$$

The total muon intensity and the angular dependence of the muons in the underground has been fit by Miyake [MIY73] to the empirical formula of

$$\Phi(h, 0) = \frac{174}{h + 400} (h + 10)^{-1.53} e^{-8.0 \times 10^{-4} h}, \quad (4.12)$$

$$\Phi(h, \theta) = \Phi(h, 0) \cos^{1.53} \theta e^{-8.0 \times 10^{-4} h (\sec \theta - 1)}. \quad (4.13)$$

Where  $h$  is the depth in *m.w.e.* or  $\frac{hg}{cm^2}$  and  $\Phi(h, 0)$  represents the vertical flux of muons in the underground at a certain depth and/or angle in  $\frac{1}{cm^2 s sr}$ .

## 4.4 THE WASTE ISOLATION PILOT PLANT

To improve the signal rate from cosmic rays it was necessary to choose an underground facility for the experiments. The Waste Isolation Pilot Plant (WIPP) near Carlsbad, New Mexico represented a fair candidate for the undertaking. WIPP is a Department of Energy (DOE) owned facility designed for trans-uranic (TRU) waste storage. It's location is about 560 kilometers south of the Los Alamos National Laboratory. WIPP hosts a mine which is driven 650 meters into a more than 600 meter thick bed of sodium chloride (salt) beneath the salado formation. With its depth, the WIPP mine represents a good shield for cosmic radiation. With a density of  $2.3 \frac{g}{cm^3}$  and equation 4.12 the estimated flux of muons is  $3.81 \times 10^{-7} \frac{1}{s cm}$ . This is five orders of magnitude lower than the surface. The WIPP is the world's first underground repository licensed to safely and permanently dispose of trans-uranic radioactive waste left from the research and production of nuclear weapons. Due to the small distance to the Los Alamos National Laboratory and its relatively large depth the WIPP was chosen as the underground site for our research and development activities.

### 4.4.1 THE WIPP LAY-OUT

Figure 4.6 shows a cross section of the WIPP. The mine has one level 650 meters underground. Four shafts connect the underground level with the surface. The salt shaft (1) is a small shaft equipped with a hoist to haul small equipment, 9 people, or the mined salt. The dimensions of the cage are roughly 119cm long by 130cm wide. The waste handling shaft (2) is equipped with a large smooth running hoist to carry the waste barrels and other large equipment into the underground. The cage is rated for hoisting up to 45 tons. Its dimensions are 287cm by 467cm and the door is 414cm high. The salt and waste shaft are in combination with the air intake shaft

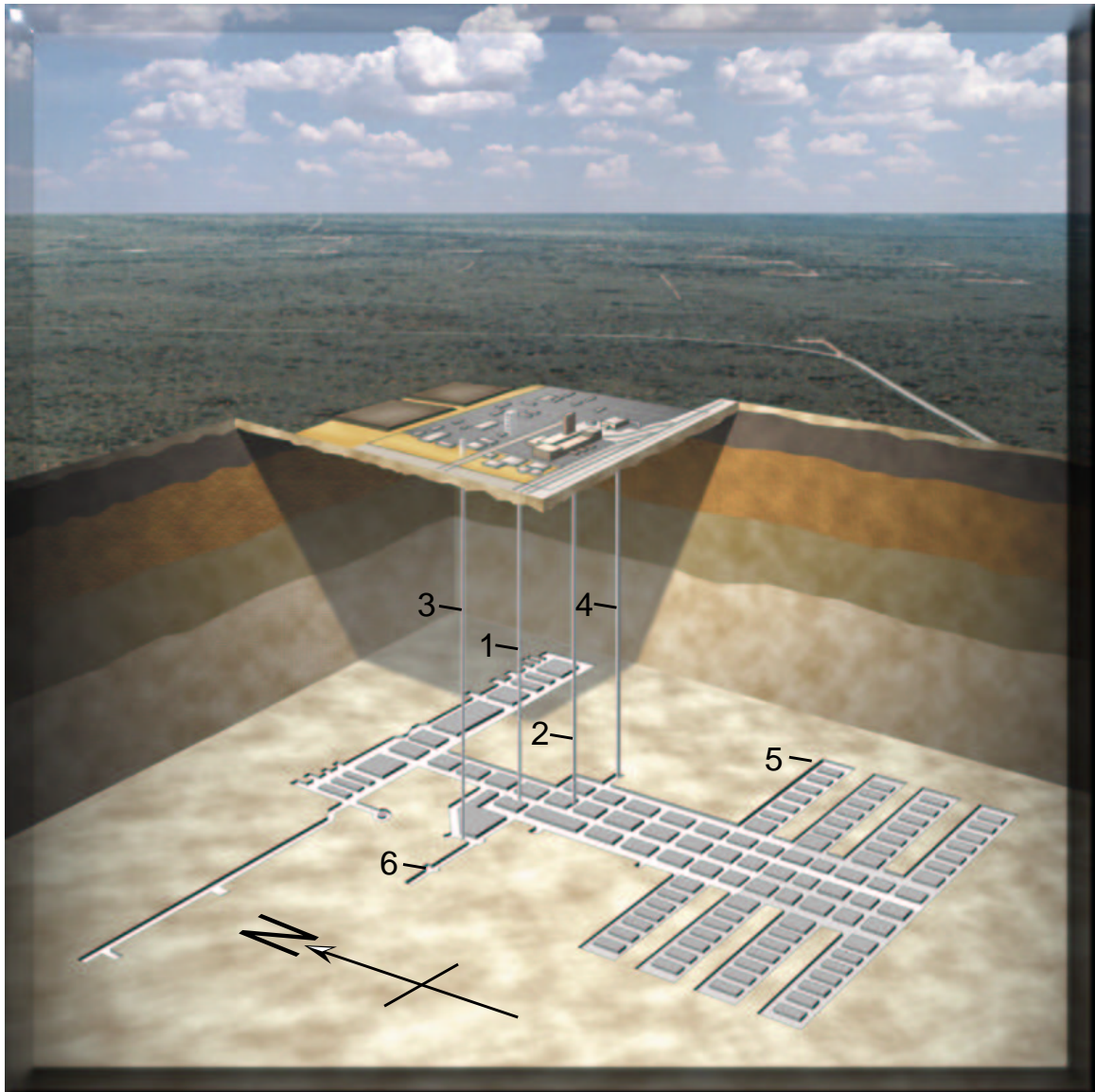


**Figure 4.6:** The layout of the WIPP. (1) salt shaft, (2) waste shaft (3) air intake shaft, (4) exhaust shaft, (5) waste panel and (6) Q-area.



**Figure 4.7:** The layout of Q-area. At the left the experimental building, at the right the shed that contained the computer system and the electronics.

(3) the input for the underground ventilation system. WIPP operates by default in a suction mode. The air needed for ventilation is sucked into the three intake shafts through the exhaust shaft (4). The pumps working in the exhaust shaft are equipped with high-efficiency particulate air (HEPA) filters which can be put into the ventilation loop within seconds. This way a possible airborne contamination from the TRU-waste can be kept in the mine. The airflow in the mine is directed in a way that the air first runs from the intake into the experimental (6) and working area and later through the waste panels (5) (see Figure 4.6). Thereby even in the event of air contamination the experimental area will stay clean.

#### 4.4.2 THE EXPERIMENTAL AREA

The Los Alamos National Laboratory experimental area is located about 600 meters from the waste depository. The 600 meters are a natural shield of pure sodium chloride (salt). The area for the Los Alamos National Laboratory experiments is called Q-Area (see figure 4.7). It is located in the far east end of the S90 drift in the alcove. WIPP personnel first set up a shed to host the LANL electronics equipment. The so called Q-shed is a insulated shed, constructed like a walk in refrigerator equipped with two air conditioning units to cool the electronics and computer systems used for the experiments. A sealed door is installed to keep the salt dust out which can exist as airborne contamination when mining is bee-

ing done. The shed is furthermore furnished with an air dryer to extract moisture from the atmosphere to prevent corrosion of the electronics and computer parts. Connected through a  $76\text{mm}$  diameter conduit, a Los Alamos National Laboratory manufactured experimental building is used for setup of the different types of detectors. The building is RF-shielded by being a uni-strut construction on a  $32\text{mm}$  thick aluminum floor. Uni-strut is a steel construction material that is easy to use with bolt able connections. Its versatility makes it an easy to use and modify material. The floor was chosen to be that thick to guarantee the support of up to 15 tons of shielding material. The walls are  $3\text{mm}$  aluminum sheet double walls with an  $18\text{mm}$  foam insulation inside them. An air conditioning unit was installed to keep the experimental equipment cooled. In order to keep the salt dust outside, the whole construction is pressurized by a large HEPA-filter that delivers up to 700 cubic feet of air per minute. Four,  $2.6\text{cm}$  diameter, electrical feed-through connectors were installed to ensure any possible future access to the building such as more electrical power, gas, or liquid nitrogen supply. The building also hosts an overhead hoist crane to provide the ability to lift and move up to one ton of shielding material. Since the building was designed to host dewar based detectors cooled with liquid nitrogen oxygen displacement was a potential hazard. The airflow outside in the drift was large enough to ensure no hazard existed for the rest of the mine. Therefore, the experimental facility was equipped with an oxygen detector that was coupled to an audio visual alarm integrated into the WIPP underground alarm response.

The whole building was designed and completely assembled at the Los Alamos National Laboratory. The building's outside dimensions are  $174\text{cm}$  by  $366\text{cm}$  by  $249\text{cm}$  of height. The floor dimensions were chosen to be  $213\text{cm}$  wide by  $427\text{cm}$  long. The floor plates were mounted on three  $102\text{mm}$  aluminum I-beams that were run across the length of the floor to be used as a sledding device and support structure. The reason for the over dimension of the floor plates was to ensure that the building would not suffer any damage in form of scraping or bending the walls while being moved around in the mine. The oversized bottom plate served as a bumper. After construction the building was loaded onto a flatbed truck and shipped to the WIPP. Since the design was such that it would fit perfectly into the waste shaft cage, it was moved completely assembled into the underground.

Material	Radio nuclide concentration ( <i>mBq/kg</i> )		
	<sup>208</sup> Tl	<sup>214</sup> Bi	<sup>40</sup> K
Aluminum	81-2,315	< 46-23,140	< 230-11,600
Beryllium 10	8,102	< 11,575	
Copper	< 3.5	< 9.3-35	< 115
Copper (grade 101)	< 0.35	< 0.6	< 5.8
Copper (OHFC)	< 3.5	< 9.3-12	< 116
Epoxy	579-46,296	926-601,851	< 11,600 - 83,300
Grease (HV)	< 11.6	< 81	< 93
Indium	< 11.6	< 35	< 230
Lead	< 0.23	< 0.5	< 1.2
Molecular sieve	4,629-5,787	11,575-34,722	92,600-104,200
Mylar, aluminized	1,157	2315	< 23,100
Oil, cutting	< 4.6	< 35	< 23
Plastic, tubing	46	< 46	< 9,260
Printed circuit board	23,148	46,296	463
Quartz	69-694	< 231-11,574	< 2,300
Reflector materials	< 1.1-1,157	< 8-2,315	< 58-3,500
Rubber sponge	579-2,314	926-13,888	< 4,600-23,100
Silica fused	< 231	< 116	< 1,157
Silicone, foam	231	579	< 2,315
Sodium iodide (TI)	< 35	< 46	< 347
Solder	< 3.5	< 9	< 116
Steel, stainless	< 23	< 69	< 2,315
Steel, pre WW II	< 5.8	< 10	< 116
Teflon	< 3.5	< 12-81	231
Wire, Teflon coated	< 46	< 12	< 231

**Table 4.3:** Primordial radio nuclide concentration in various materials.

Isotope	Half-life	Main Target	Produced Radioactivity
$^3\text{H}$	12.3 <i>y</i>	N,O	$\beta$ 18.59
$^7\text{Be}$	53 <i>d</i>	N,O	EC 861.8 $\gamma$ 477.6
$^{10}\text{Be}$	$2.6 \times 10^6$ <i>y</i>	N,O	$\beta$ 555.9
$^{14}\text{C}$	5730 <i>y</i>	N,O	$\beta$ 156.5
$^{22}\text{Na}$	2.6 <i>y</i>	Ar	EC 2842.1 $\gamma$ 1274
$^{26}\text{Al}$	$7.5 \times 10^5$ <i>y</i>	Ar	EC 4004 $\gamma$ 29380 $\gamma$ 1129 $\gamma$ 1808
$^{32}\text{Si}$	50 <i>y</i>	Ar	$\beta$ 224.4
$^{32}\text{P}$	14.3 <i>y</i>	Ar	$\beta$ 1710.6
$^{33}\text{P}$	25 <i>d</i>	Ar	$\beta$ 248.5
$^{35}\text{S}$	87 <i>d</i>	Ar	$\beta$ 167.16
$^{36}\text{Cl}$	$3.0 \times 10^5$ <i>y</i>	Ar	EC 1142.1 $\beta$ 708.6
$^{37}\text{Ar}$	35 <i>d</i>	Ar	EC 813.5
$^{39}\text{Ar}$	270 <i>y</i>	Ar	$\beta$ 565

**Table 4.4:** Isotopes with half-lives longer than one day produced by cosmic rays. The column with the produced radioactivity shows the type of radiation ( $\beta$ ,  $\gamma$  and electron capture) emitted by the Isotope.

Rock Type	U(ppm)	Th(ppm)	neutron production in [ $\frac{n}{yg}$ ]		
			U( $\alpha,n$ )	Th( $\alpha,n$ )	fission
granite	5	11	7.85	7.755	2.33
limestone	1	1	0.64	0.285	0.467
sandstone	1	1	0.837	0.38	0.467
granite A	1.32	7.79	2.24	5.92	0.62
granite B	6.25	4.59	10.62	3.49	2.92
granite C	1.83	4.38	3.11	3.33	0.85
salt I	0.30	2.06	1.60	4.77	0.14
salt II	0.13	1.80	4.17	0.69	0.06

**Table 4.5:** Neutron production in different types of rock. Data is taken from [FLO88].

Target nucleus	Average multiplicity
AL	1.262±0.0059
Si	0.864±0.0072
Ca	0.746±0.0032
Fe	1.125±0.041
Ag	1.615±0.060
I	1.436±0.056
Au	1.662±0.044
Pb	1.709±0.066

**Table 4.6:** Neutron multiplicity factors from [SIN74] in different materials.

$E_\mu$ GeV	$R$ km.w.e.	$a_{ionization}$ MeV g <sup>-1</sup> cm <sup>2</sup>	$b_{pair}$ —	$b_{brem_s}$ 10 <sup>-6</sup> g <sup>-1</sup> cm <sup>2</sup>	$b_{nucl}$ —	$\sum b_i$ —
10	0.05	2.15	0.73	0.74	0.45	1.91
100	0.41	2.40	1.15	1.56	0.41	3.12
1000	2.42	2.58	1.47	3.20	0.44	4.01
10000	6.30	2.76	1.65	2.27	0.50	4.40

**Table 4.7:** Average muon range in rock with the  $a$  and  $b_i$  parameters for equation 4.10.

## 4.5 GAMMA BACKGROUND AT WIPP

A hyper pure germanium (HPGe) detector from Princeton Gamma Tech (PGT) was used to measure the gamma-ray reduction and background at the WIPP. The advantages of a Ge detector are given by its high energy resolution and high efficiency for Gamma-rays. The detector used was an N-type, intrinsic coaxial Germanium detector with a 22% efficiency at  $1.4\text{MeV}$  gamma energy. It had a  $2.0\text{keV}$  resolution at  $1392\text{keV}$ . It was made in 1985 with an outer diameter of  $51\text{ mm}$  and a height of  $41\text{ mm}$ . Fully depleted with 2300 Volts, the detector has an active volume of  $82\text{ cm}^3$ . The mount was constructed so that the crystal is only  $5\text{ mm}$  away from the thin beryllium window at the top of the cryostat.

### 4.5.1 THE DATA ACQUISITION

The Data acquisition electronics consisted of the Ge detector with a PGT pre-amplifier. The pre-amplifier output was then fed into a 672 ORTEC spectroscopic amplifier. The shaping time used was the one suggested by the manufacture,  $4\text{ }\mu\text{s}$ . The signal output was then carried into a TRUMP-8k multi channel buffer card mounted in an IBM-PC. The card has an internal 13 bit ADC. The technical features of the card are shown in table 4.8. The Data acquisition was done with the Maestro software from EG&G-ORTEC.

ADC	Successive-approximating type with sliding scale linearisation.
Resolution	Software select able as 512, 1024, 2048, 4096, 8192.
Dead time per event	$8\text{ }\mu\text{s}$ , including memory transfer.
Data memory	8k channels of battery backed-up memory.

**Table 4.8:** TRUMP-card technical data

### 4.5.2 DETECTOR ENERGY CALIBRATION AT LANL

The energy calibration of the Ge-Detector was done with two radioactive sources. The low end of the energy spectrum was calibrated with a  $^{57}\text{Co}$  source, the high end with a  $^{22}\text{Na}$  source. Table 4.9 shows the gamma lines that are expected from the sources. For the cases at LANL the  $^{57}\text{Co}$  source provides the  $122.06\text{keV}$  and the  $136.47\text{ keV}$  peak and the  $^{22}\text{Na}$  supplied the  $1274.53\text{keV}$  peak. The analysis was done in ROOT, an analysis tool from CERN [ROO01].

The energy calibration for both the experiments at LANL and at WIPP was done with the same approach. First a Gaussian was fit to each peak of the calibration

Source	Energy [keV]
<sup>22</sup> Na	1274.53
<sup>40</sup> K	1460.85
<sup>57</sup> Co	14.40
	122.06
	136.47
<sup>60</sup> Co	1173.24
	1332.516
<sup>133</sup> Ba	80.997
	302.853
	356.017
<sup>241</sup> Am	59.537

**Table 4.9:** The table shows the sources and their gamma ray energies. The peaks are sorted in a ascending energy order.

source. Then the channel values of the means of the Gaussian with their  $\frac{\sigma}{\sqrt{n}}$  as error were used for a linear fit

$$Channel = a + b \times Energy \quad (4.14)$$

of the energy to the channel number. Figure 4.8 shows the data points of the fit with the fitted line in the upper plot. The residual of the data points to the line fit is shown in the lower plot. The residual is plotted in keV. The error bar markers a  $\frac{\sigma}{\sqrt{n}}$  deviation.

### 4.5.3 THE BACKGROUND SPECTRA AT LANL

To establish an initial background baseline at the surface, background measurements were performed with different shielding configurations at LANL. The measurements conducted at Los Alamos are shown in table 4.10. The table shows the shield thickness and the run time over which the spectra were taken. Figure 3.12 shows a schematic drawing of the fully-shielded experiment. Three spectra were

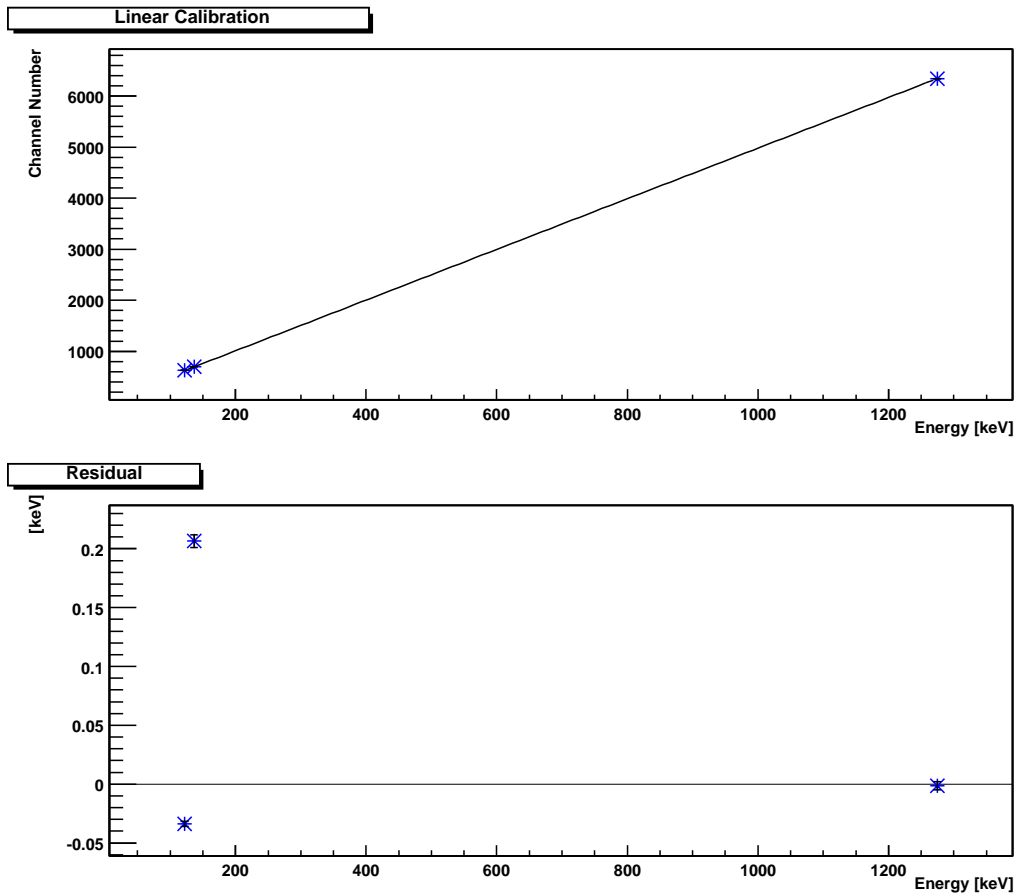


**Figure 4.8:** Linear fit of the gamma spectra taken at LANL. The upper plot shows the data points of the sources used for the fit. The lower plot shows the residual of the data points from the fit.

Spectrum name	Copper [in]	Lead [in]	Time [s]
bkg_10k	0	0	10,000
Cu_50k	2	0	50,000
Pb_100k	2	4	100,000

**Table 4.10:** Germanium spectra taken at LANL. The table shows the shield thickness and time over which the spectra were taken. The Energy ranged between 22 *keV* and approximately 1600 *keV* .

taken. A plain background spectrum (bkg\_10k) over a time interval of 10,000 seconds to determine the unshielded background in the basement D-3, Building 1, TA-53 at LANL. Figure 4.9 shows the spectrum as an energy histogram. The left axis shows the count rate per *keV* . The bottom axis is scaled to the energy in *keV* . Above the peaks are the fitted energy values, followed by the nominal energy of the peak, and the symbol of the element producing the gamma rays. The spectrum peaks are dominated by the uranium and thorium chains. The second spectrum (Figure 4.10) consists of a 50,000 second background run in which the detector was shielded by 2 inches of oxygen free 101 copper. The low energy peaks are strongly diminished by the copper as expected.

The third spectrum was taken with a 2 inches thick shield of copper around the detector and a 4 inches thick lead enclosure around the copper. Figure 4.11 shows the spectrum. The reason for detecting low and high energy gamma lines in this spectrum is given by the large decrease (a factor of 105) of count rate from a plain background spectrum to a fully shielded version. Note the two peaks at 596 and 669 *keV* . They are due to inelastic scattering from the fast neutrons in the background flux on Germanium and Copper.  $^{74}\text{Ge}$  as a stable isotope has an excited state with an energy of 595.852 *keV* and a lifetime of 12.35 pico seconds.  $^{63}\text{Cu}$  is also stable and has an excited state at 669.69 *keV* with a lifetime of 0.198 pico seconds.  $^{72}\text{Ge}$  has two meta-stable states with energies of 691.55 *keV* (444 nano seconds) and 962.1 *keV* (834 pico seconds life time). The comparatively large width of the peak results from the additional recoil of the Ge nucleus in the crystal. Since the meta stable states are short lived compared to the integration time of the pulse, the energy released from the meta-stable state and the recoil energy, which is dependent of the scattering angle and the initial energy of the neutron, is added. Therefore, the peak becomes much wider than a conventional gamma peak. Since

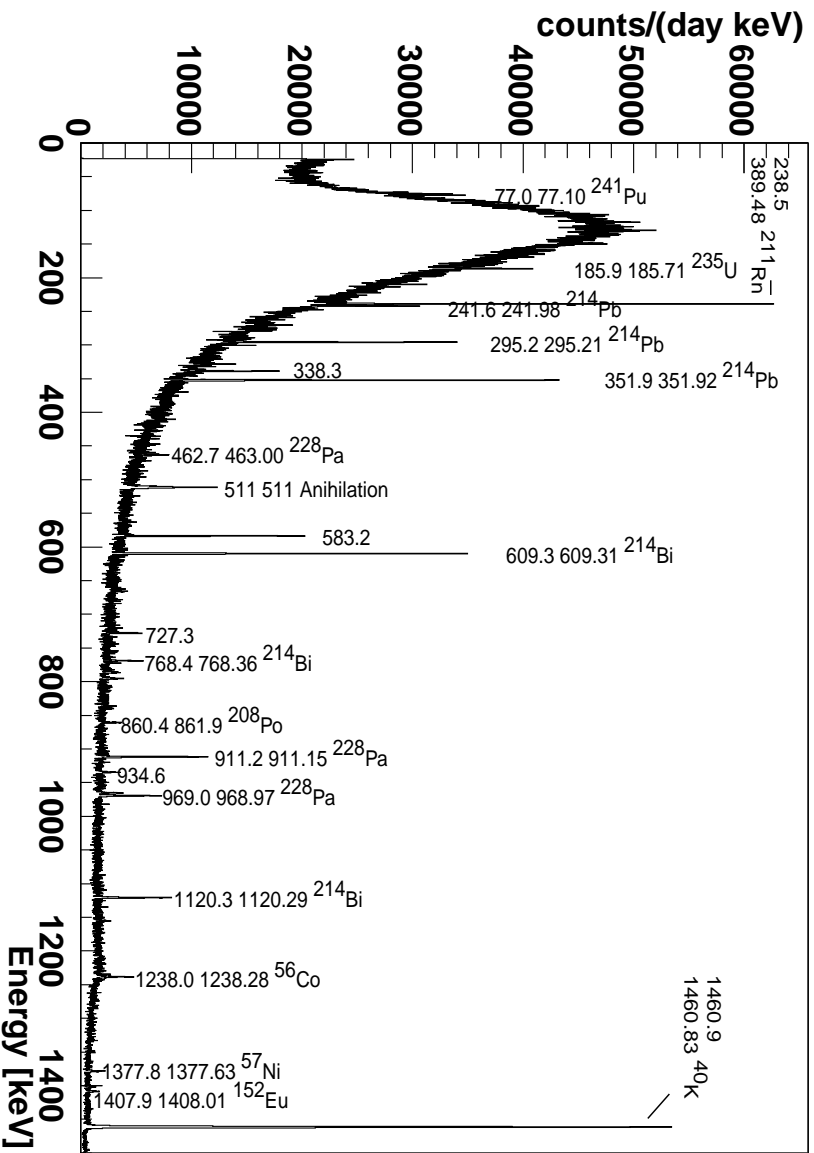


Figure 4.9: Pure background spectrum at LANL. The Germanium detector was set up without any shielding around it. The run time was 10,000 seconds long.

this broadening can only be detected in the crystal itself, the copper peak does not show this behavior. The nuclear recoil of the copper cannot be detected in this way. The continuum in the spectra taken at LANL is mainly generated by elastic scattering of fast neutrons from muons in the germanium detector. Since the expected neutron flux at the WIPP site is not dominated by fast neutrons from muon spallation it is not visible at the WIPP site.

In each spectrum the events between 25 *keV* and 1600 *keV* were integrated and a count rate was specified (see Table 4.11).

The integration for this interval took place from bin 142 to bin 7958. The same integral was done in an interval of 25 *keV* to 700 *keV* to be able to compare it with the silicon detector. In this case, the integration interval was from bin 142 to bin 3491. Table 4.11 shows that the count rate is reduced from the non-shielded background to the 2 inches of surrounding copper by a factor of 10.5. The reduction from 2 inches of surrounding copper to 4 inches of lead surrounding 2 inches of copper is another reduction factor of 10. This adds up to a total reduction of 105 (see Table 4.16)

Name	Time [s]	Events 25-1600	Count rate 25-1600 [Hz]	$\Delta$ 25-1600 [Hz]	Events 25-700	Count rate 25-700 [Hz]	$\Delta$ 25-700 [Hz]
bkg_10k	10,000	1,209,930	136.9	$\pm 0.1$	1,209,930	121.9	$\pm 0.1$
Cu_50k	50,000	652694	13.05	$\pm 0.02$	552,767	11.06	$\pm 0.01$
Pb_100k	100,000	130365	1.304	$\pm 0.004$	110,248	1.102	$\pm 0.003$

**Table 4.11:** Count rates for germanium spectra taken at LANL. Shown is the name of the spectrum, the runtime in seconds, the events between 25 *keV* and 1600 *keV*, their count rate and its error. Also shown is the count rate between 25 *keV* and 700 *keV*, its count rate and its error.

#### 4.5.4 DETECTOR ENERGY CALIBRATION AT THE WIPP

At the WIPP the energy was calibrated twice. Once for a differential shielding measurement for copper and lead shielding. The second energy calibration was done after a wax shield was put in place. The totally shielded detector is shown in figure 4.18. The first calibration was done with a  $^{57}\text{Co}$  source and a  $^{133}\text{Ba}$  source. The energies used for calibration were 122.06 *keV*, 136.47 *keV* from  $^{57}\text{Co}$ , 366.06 *keV* from  $^{133}\text{Ba}$  and due to the lack of high energy sources, the 1460.85 *keV* peak from

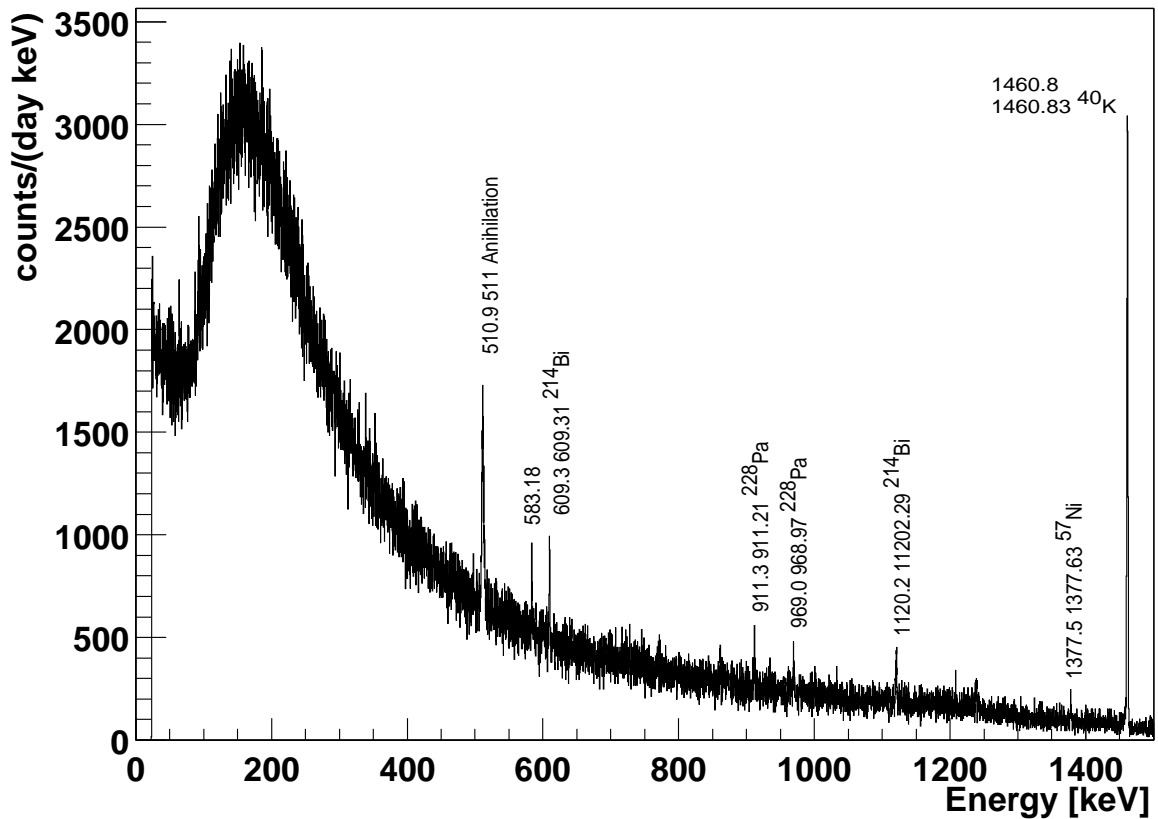


**Figure 4.10:** Copper background spectrum at LANL. The Germanium detector was set up with 2 inches of oxygen free copper 101 around it. The run time was 50,000 seconds. The left axis shows the frequency per  $keV$ . The bottom axis is scaled to the energy in  $keV$ .

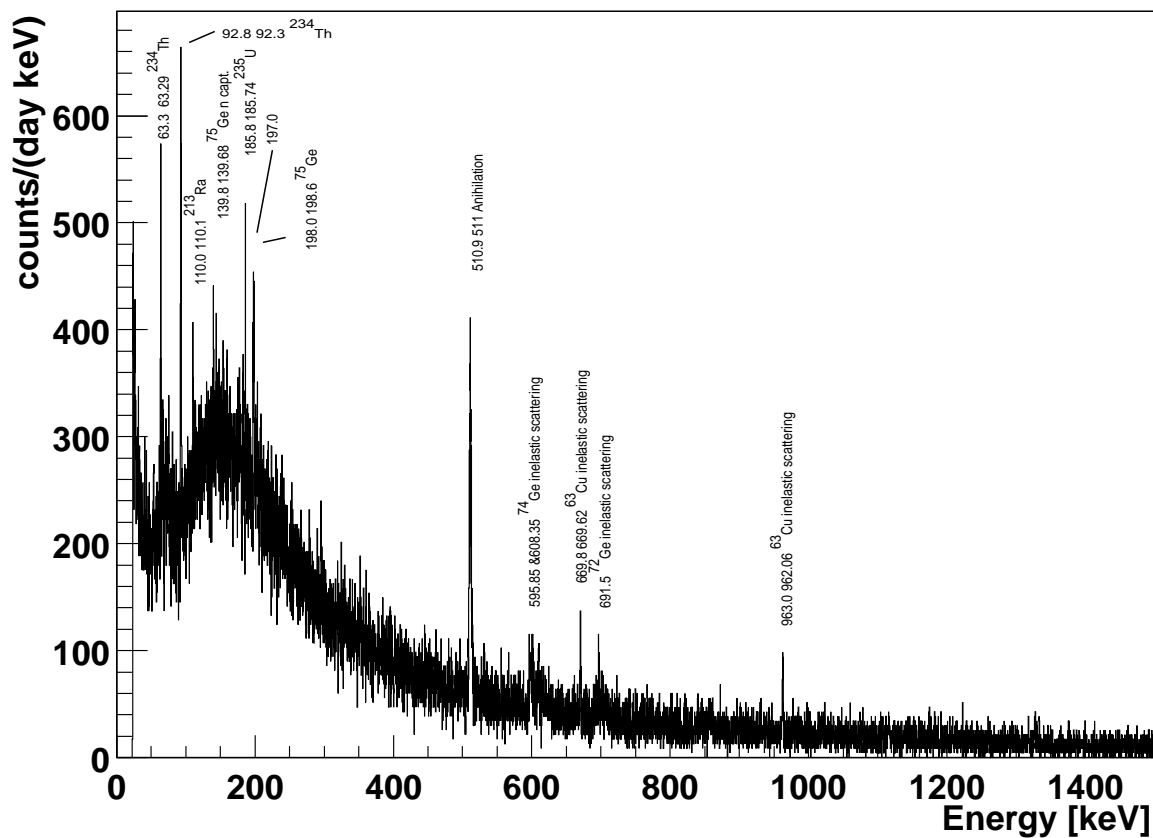


**Figure 4.11:** Full shielded background spectrum at LANL. Full shielded background spectrum at LANL. The Germanium detector was surrounded by 2 inches of oxygen free copper 101 followed by 4 inches of lead shielding. The duration of the run time was 100,000 seconds. The left axis shows the count rate per  $keV$ . The bottom axis is scaled to the energy in  $keV$ .

$^{40}\text{K}$ . The calibration during the run with the wax shield was performed with  $^{57}\text{Co}$ ,  $^{133}\text{Ba}$  sources from the Carlsbad environmental monitoring and research center (CEMRC) team at NM-State in Carlsbad, NM. The energies are 81.00 keV, 122.06 keV, 136.47 keV, 302.85 keV, 356.02 keV and 1460.85 keV. The Energy calibration was done as described in Section 4.5.2. Figure 4.12 shows in the upper plot the data points and their fit. In the lower plot the residual of the data points with their  $\frac{\sigma}{\sqrt{n}}$  error are shown. To double check on the calibration a second calibration after the first run was made. The first calibration was used to determine the values of the peaks present in the background spectra taken. Then the intrinsic peaks of the spectra were fitted and used for a new calibration. The peaks used are 63.29 and 93.38 keV of  $^{234}\text{Th}$ , 185.74 keV of  $^{235}\text{U}$  and 1460.85 of  $^{40}\text{K}$ . Their fits and residuals are listed in Table 4.12.

Energy [keV ]	fitted Energy [keV ]	$\Delta$ Energy [eV ]
63.29	63.88	590
93.38	92.81	570
185.74	185.70	40
1460.85	146.85	0

**Table 4.12:** Energy fit compared to the real energy with intrinsic peaks. The energy values are taken from the table of isotopes. The fitted energies are deduced through the fitted line.

#### 4.5.5 THE BACKGROUND SPECTRA AT THE WIPP

At the WIPP the goal was to determine the background radiation in the mine itself and to evaluate different shielding materials. Five background spectra were taken. A plain spectrum with no shielding, a spectrum with a one inch copper shield (cu\_1in) around the detector, a spectrum with a 2 inch copper shield around the detector (cu\_2in), a spectrum with a 2 inch copper shield enclosed in a 4 inch lead shield (pbsum). In a second run a spectrum where the lead shield is surrounded on five of six sides with approximately twelve inches of wax was gathered (wax1). The wax was put in place to thermalize and capture possible fast neutrons. A count rate decrease in the two integral intervals could not be found. Since the neutron count rate is expected to decrease from Los Alamos to WIPP by 5 orders of magnitude it was not surprising to see no change in the count rate of the two spectra.

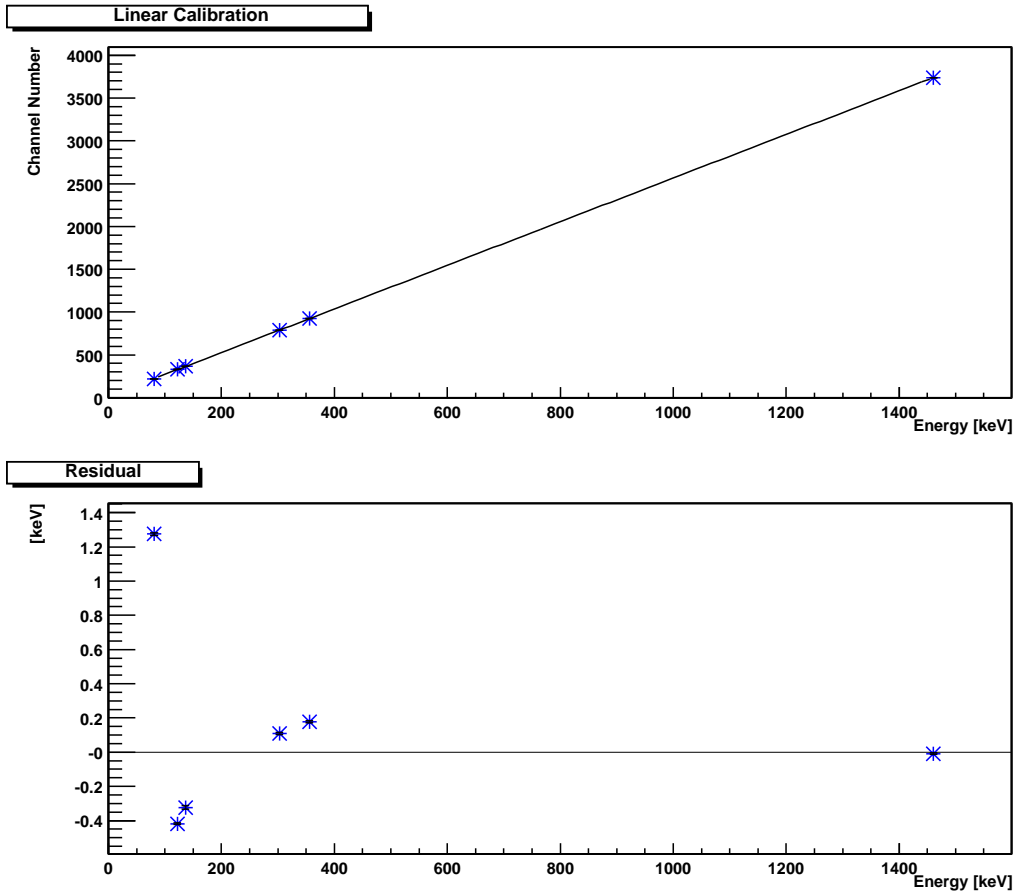


**Figure 4.12:** Linear fit of the gamma spectra taken at WIPP. The upper plot shows the data points of the sources used for the fit. The lower plot shows the residual of the data points from the fit.

Table 4.13 shows the lifetime and the thickness of each shield component for each configuration.

The first spectrum was taken over a time of 60,500 seconds. It is displayed in

Name	Copper [in]	Lead [in]	Wax [in]	Time [s]
noshield	0	0	0	60,500
cu.1in	1	0	0	5,000
cu.2in	2	0	0	337,911
pbsum	2	4	0	1,278,581
wax1	2	4	12	668,553

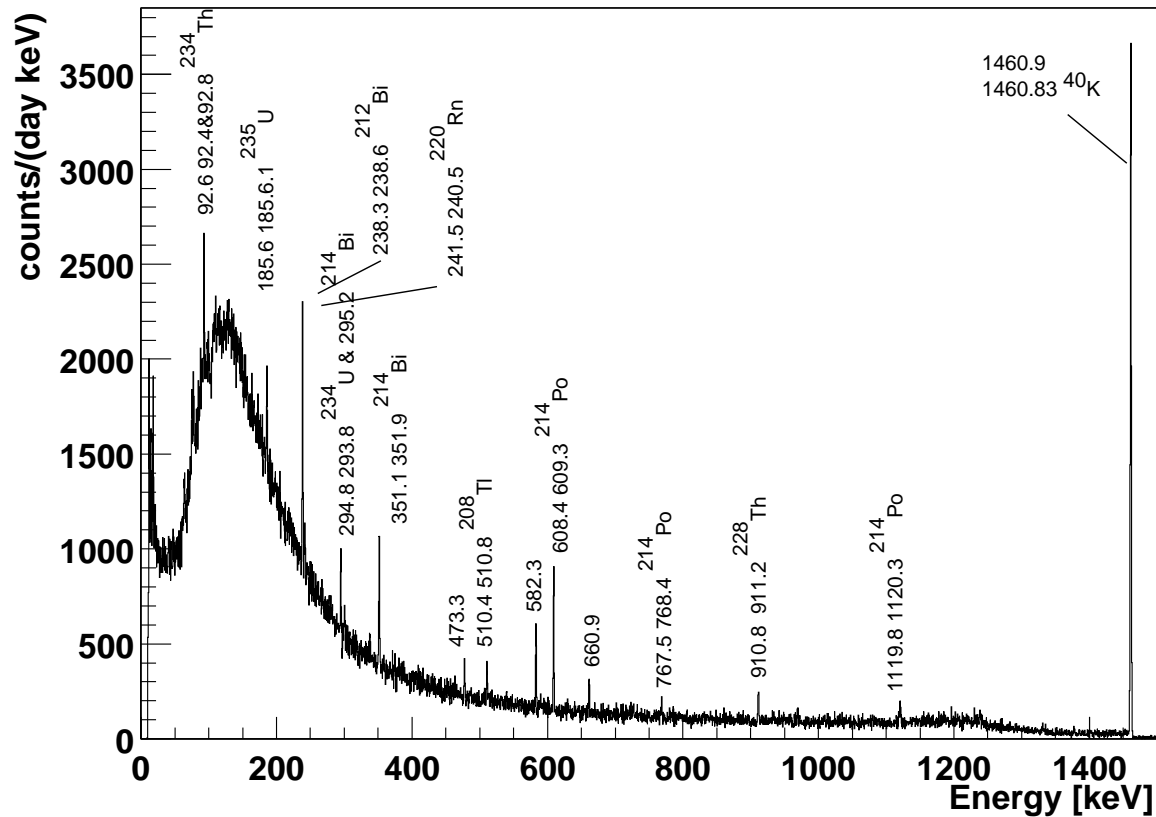
**Table 4.13:** Germanium spectra taken at WIPP. The table shows the shield thickness and run time during which the spectra were taken. The Energy ranged between 12 *keV* and approximately 3100 *keV* .

figure 4.13. The Germanium detector was set up without any shielding around it inside the experimental building at the WIPP.

The second spectrum (cu.1in) is a spectrum taken over a time interval of 5,000 seconds. Here the detector was surrounded by a layer of 1 inch oxygen free 101 copper. The spectrum (cu.2in) was taken over a time-period of 337,911 seconds and the detector was shielded by 2 inches of oxygen free 101 copper. It is shown in figure 4.15. After that the detector with the copper shield was enclosed in 4 inches of lead (pbsum). Figure 4.17 shows the spectrum with the full shielding and 1 foot of wax around it. The spectrum is shown in figure 4.16. Figure 4.19 shows all spectra from LANL and WIPP in a comparison plot. To better show the improvement from shielding and underground site, the count rate is shown on a logarithmic axis.

In each spectrum the events between 25 *keV* and 1600 *keV* were taken and a count rate was specified (see table 4.14). The same integral was done in an interval of 25 *keV* to 700 *keV* to be able to compare it with the silicon detector.

For the second run with the wax, the spectrum was integrated in the same way, once from 25 to 1600 *keV* and once from 25*keV* to 700 *keV* . Table 4.14 shows that the count rate is reduced from the non-shielded background to the one inches of surrounding copper by a factor of 3.32. The reduction from 1 inch of copper to 2 inches of copper is 2.32. From 2 inches of surrounding copper to 4 inches of lead surrounding 2 inches of copper around the detector the reduction factor is 5.4. This adds up to a total reduction of 41.6 which is about half as much reduction



**Figure 4.13:** Pure background spectrum at the WIPP. The Germanium detector was set up without any shielding around it inside the counting room at the WIPP. The run was 60,500 seconds long. The left axis shows the count rate per  $keV$ . The bottom axis is scaled to the energy in  $keV$ .

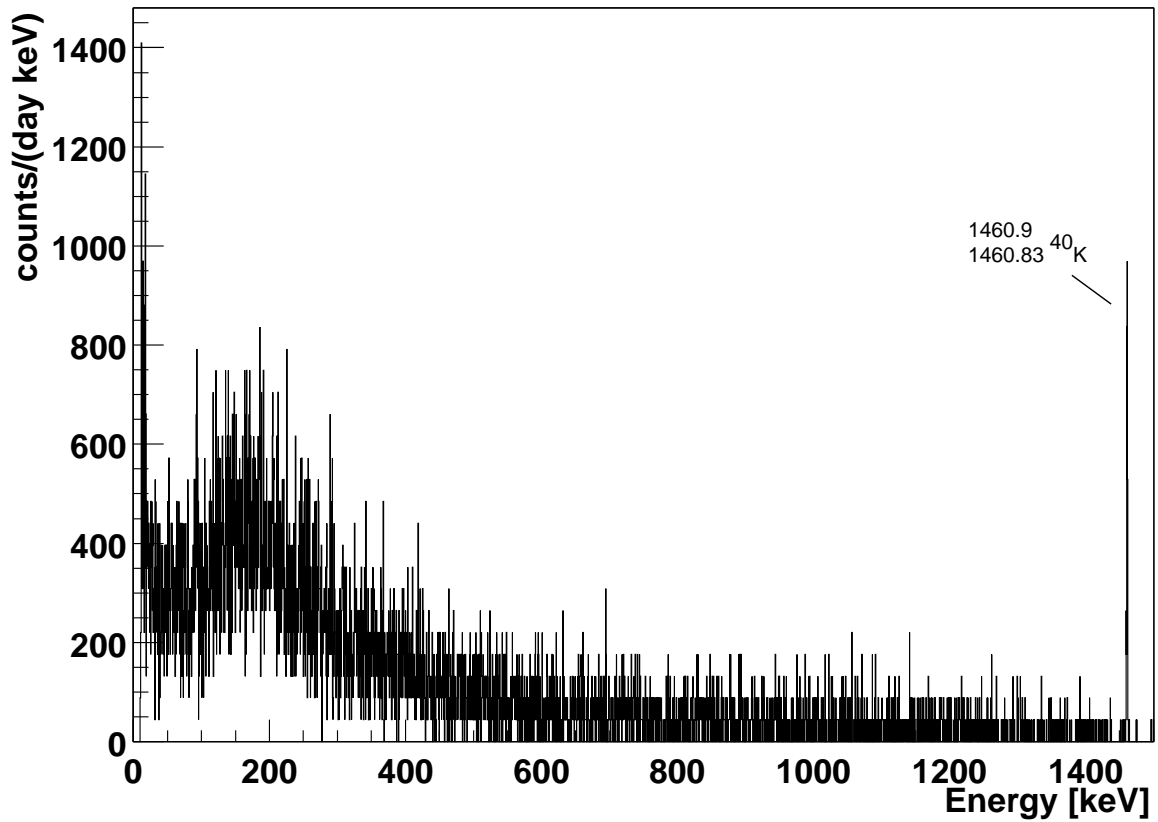


**Figure 4.14:** The Germanium detector was put into a copper enclosure with a thickness of 1 inch. The run time was 5,000 seconds long. The left axis shows the count rate per  $keV$ . The bottom axis is scaled to the energy in  $keV$ .

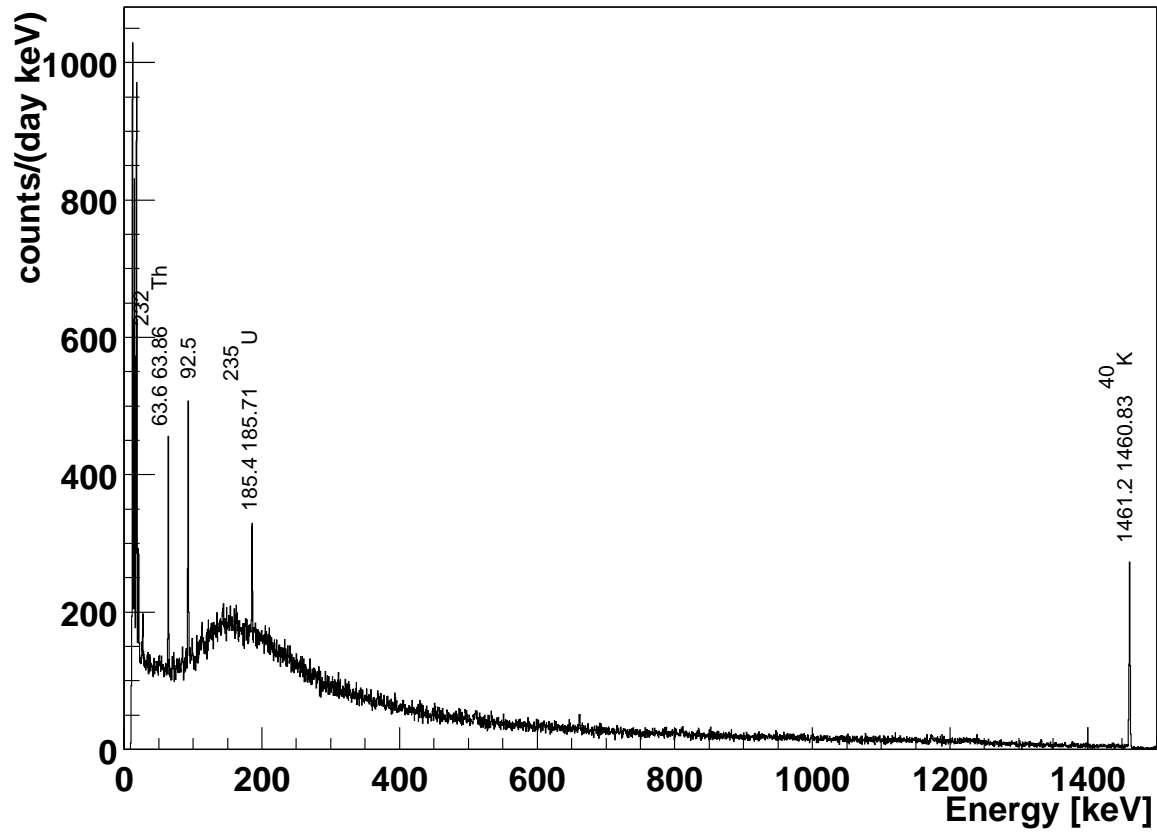


**Figure 4.15:** The Germanium detector was put into a copper enclosure with a thickness of 2 inches. The run time was 337,911 seconds long. The left axis shows the count rate per  $keV$ . The bottom axis is scaled to the energy in  $keV$ .

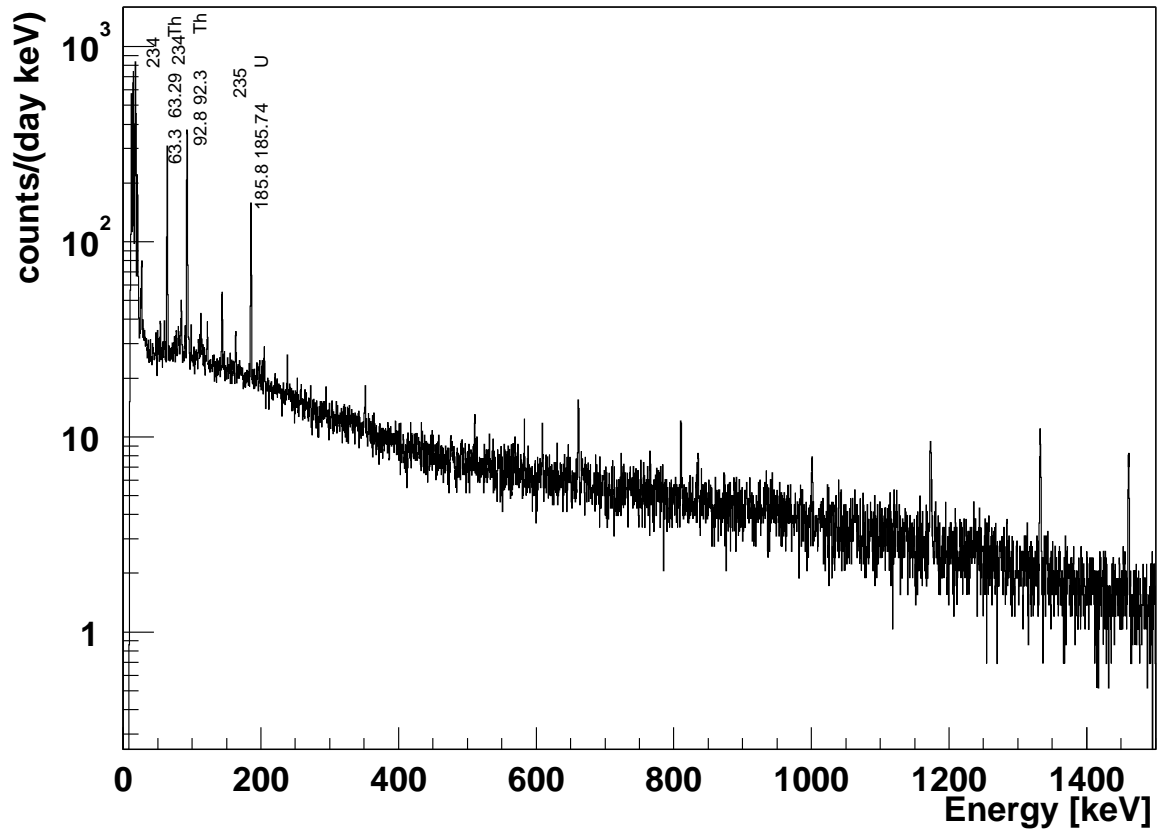


**Figure 4.16:** The germanium detector was enclosed in 4 inches of lead around 2 inches of copper. The run time was 1,278,581 seconds long. The left axis shows the count rate per  $keV$ . The bottom axis is scaled to the energy in  $keV$ .

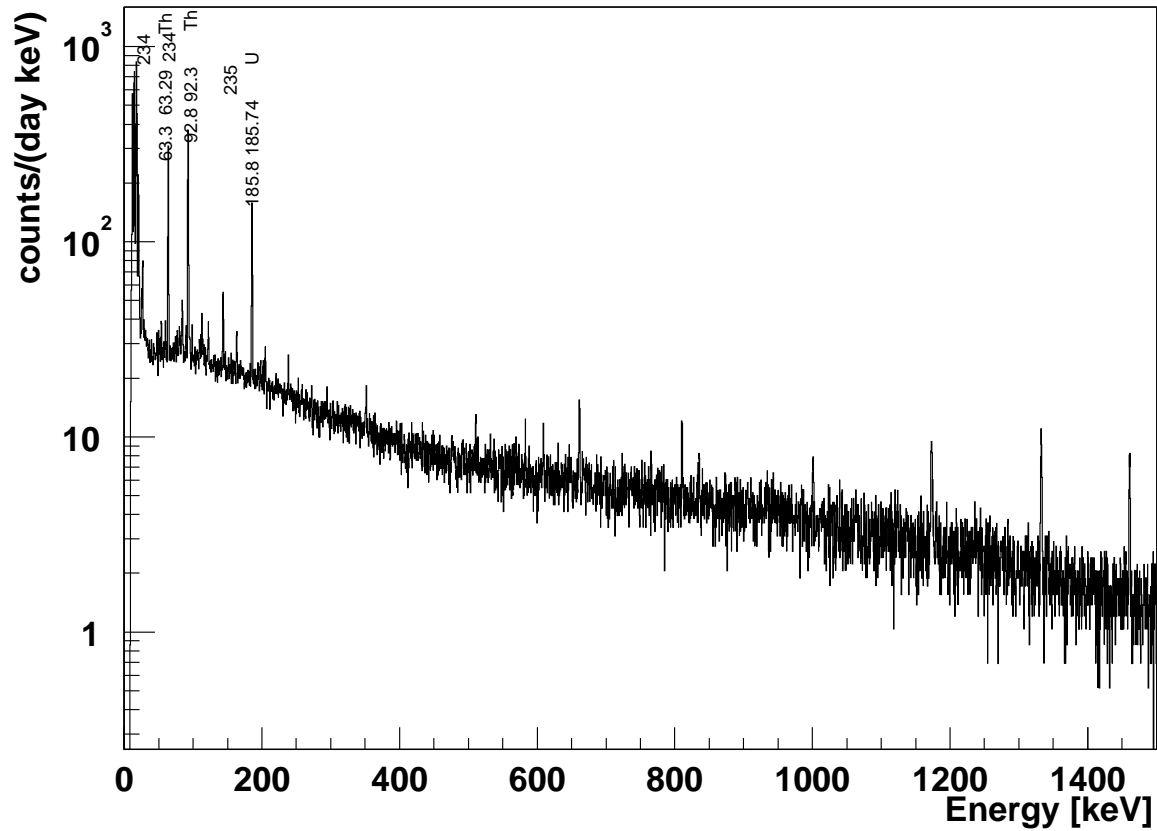


**Figure 4.17:** The germanium detector was enclosed in 12 inches of wax, 4 inches of lead around 2 inches of copper. The run time was 668,553 seconds long. The left axis shows the count rate per  $keV$ . The bottom axis is scaled to the energy in  $keV$ .



**Figure 4.18:** Detector inside full shielding at the WIPP underground.

Name	Time [s]	Events 25-1600	Count rate 25-1600 [Hz]	$\Delta$ 25-1600 [Hz]	Events 25-700	Count rate 25-700 [Hz]	$\Delta$ 25-700 [Hz]
noshield	60,500	383,893	6.345	$\pm 0.01$	333,777	5.517	$\pm 0.01$
Cu .1in	5,000	9,557	1.911	$\pm 0.02$	8,001	1.60	$\pm 0.02$
Cu .2in	337,911	278,778	0.825	$\pm 0.001$	232,262	0.687	$\pm 0.001$
pbsum	1,278,581	195,228	0.1527	$\pm 0.0003$	153,400	0.1200	$\pm 0.0003$
wax1	668,553	6640	0.1483	$\pm 0.002$	5,162	0.11529	$\pm 0.002$

**Table 4.14:** Count rates for germanium spectra taken at the WIPP. Shown is the name of the spectrum, the runtime in seconds, the events between 25 and 1600 keV , their count rate and its error. Also shown is the count rate between 25 and 700 keV , count rate and its error.

as recorded in Los Alamos. (see Table 4.16). It is interesting to see that the factor from the shielded background at LANL to the non-shielded background at LANL is 105 whereas in the underground at the WIPP. the factor is only 41.6. Focusing on the factors of equal shielding above and below ground and assuming similar gamma-ray background one would expect the same reduction rate. This is not the case. The reduction from non-shielded background is a factor of 21.6, the reduction from 2 inches of copper derive a factor of 15.8 and the full shield finally delivers a reduction factor of only 8.53. This strongly suggests that the Germanium detector is dominated by intrinsic contamination which is visible due to the increased shield. Another evidence for the internal contamination of the Ge-detector can be found in the low energy uranium and thorium peaks in the front of the spectrum shown in figure 4.16. Inside the copper shield the uranium and thorium peaks are of nearly the same count rate as inside the copper and lead shield. The peaks (63, 95, 183 keV ) are also visible in the fully shielded experiment at the surface at Los Alamos National Laboratory. Table 4.15 shows the rates achieved from the peaks. The ratio of the 92.5 keV to the 63.3 keV peak is with a ratio of 1.5 slightly higher than the ratio quoted by the table of isotopes which is 1.2. This effect is explained by the strong dependency of the gamma-attenuation at such low energies. After extracting the integral under the peaks one can calculate the possible internal contamination of the germanium detector. The frequency of  $^{235}\text{U}$  decay was measured as  $1.9 \pm 0.5 \text{ mHz}$ , its half life is  $7.3 \times 10^8$  years. The decay branch in  $^{235}\text{U}$  has a probability of 57%.  $^{235}\text{U}$  is present in natural uranium with a percentage of 0.72%.

With the activity law

$$N = \frac{T_{\frac{1}{2}}}{\ln 2} A, \quad (4.15)$$

one can calculate the number of uranium atoms present.  $N$  represents the total number of atoms,  $A$  the present activity and  $T_{\frac{1}{2}}$  the half life. With this number one can then calculate the amount of uranium mass present to generate this signal. The number comes out to  $6 \mu g$  of uranium. One can compare this to the contamination numbers of table 4.3 and derive an Al mass present near the detector between roughly  $50g$  to  $300g$ . This is an expected mass for a detector holder cup. Another candidate for this contamination is the beryllium window in the cup of the detector which has a contamination similar to aluminum. The beryllium window was put into the cup to ensure the penetration of low energy x-rays. The activity in the cryostat is a significant contribution to the germanium detector.

Since the neutron flux is expected to be reduced by 5 orders of magnitude by going underground (see Figure 4.3) the neutron peaks visible in the spectrum taken at Los Alamos National Laboratory cannot be detected in the underground. Therefore the ratio of the flux can only be stated as an upper limit. The count rate in the three germanium peaks are measured to have a frequency of  $4.89 \pm 0.16 \times 10^{-2} Hz$ . In the WIPP underground spectrum the statistical error on the backgrounds spectrum was used for an upper limit for the reduction. The flux was  $0 \pm 1.14 \times 10^{-4} Hz$  which sets a lower limit for the reduction factor of  $>415$ .

Name	Energy [keV]	Count rate copper [mHz]	Count rate lead [mHz]
$^{235}\text{U}$	185.7	$2.0 \pm 0.2$	$1.9 \pm 0.05$
$^{234}\text{Th}$	92.5	$5.6 \pm 0.2$	$5.0 \pm 0.07$
$^{234}\text{Th}$	63.3	$3.7 \pm 0.2$	$3.4 \pm 0.06$

**Table 4.15:** Peak intensities inside copper and lead shield. The table shows the peak intensities measured once inside 2 inches of copper shielding and once inside 2 inches of copper and 4 inches of of lead.

Name		LANL			WIPP				
		bk_10k	Cu_50k	Pb_100k	noshield	Cu_1in	Cu_2in	pbsum	wax1
LANL	bkg_10k	1	10.4	105	21.6	71.6	166	897	923
	Cu_50k		1	10.0	2.06	6.82	15.8	85.5	88.0
	Pb_100k			1	0.205	0.682	1.58	8.53	8.79
WIPP	noshield				1	3.32	7.69	41.6	42.8
	Cu_1in					1	2.32	12.5	12.9
	CU_2in						1	5.40	5.56
	pbsum							1	1.03
	wax1								1

**Table 4.16:** Reduction rates for all spectra. The table provides the relative reduction factor for each spectrum to each spectrum. The rate in the spectrum of each row is by that factor larger than the spectrum shown in the column. The count rate was determined between 25 keV and 1600 keV .

#### 4.5.6 REDUCTION OF $^{40}\text{K}$ FLUX

To determine the reduction of the  $^{40}\text{K}$  flux, the area under the peak of each spectrum was calculated. The peak was first fit to a Gaussian in order to determine a good value for  $\sigma$ . A baseline average ( $avg_1$ ) was taken in the region

$$\mu - (3\sigma + 10) \leq x \leq \mu - 3\sigma. \quad (4.16)$$

Here  $\mu$  represents the channel number of the peak. The baseline was then averaged over the first ten bins in front of the  $3\sigma$  region. The same was done with ( $avg_2$ ) in the region

$$\mu + 3\sigma \leq x \leq \mu + (3\sigma + 10). \quad (4.17)$$

The area under the peak was then integrated within the  $\pm 3\sigma$  region and the background was removed by subtracting the trapezoid under the peak given by the averages for the two baselines:

$$B = 3\sigma (avg_1 + avg_2). \quad (4.18)$$

Table 4.17 shows the values for the  $^{40}\text{K}$  peaks in the different shields at LANL and at the WIPP. The reduction factors are shown in Table 4.18. The reduction factor of the  $^{40}\text{K}$  flux from the non-shielded background to a shield consisting of 2 inches of copper at LANL is 18. At LANL it was not possible to make out a  $^{40}\text{K}$  peak in the

Name	$^{40}\text{K}$ area [counts]	$\sigma$ area [counts]	Time [s]	Count Rate [Hz]	$\Delta$ [Hz]
bkg_10k	11711	$\pm 108$	10,000	1.17	$\pm 0.01$
Cu_50k	3174	$\pm 56$	50,000	.0634	$\pm 0.001$
Pb_100k	NA	NA	100,000	NA	NA
noshield	4966	$\pm 70$	60,500	0.082	0.001
Cu_1in	108	$\pm 10$	5,000	0.021	0.002
Cu_2in	2079	$\pm 45$	337,911	0.0061	0.0001
pbsum	172	$\pm 13$	1,278,581	0.00013	0.00001
wax1	85	$\pm 9$	668,553	0.00006	0.00001

**Table 4.17:** The table shows the area under the  $^{40}\text{K}$  peak, the statistical error for the area, the runtime of the spectrum and the count rate and its error in Hz.

spectrum that had a shielding of 4 inches of lead around 2 inches of copper.

At the WIPP the  $^{40}\text{K}$  line was diminished by a factor of 13 going from a non-shielded detector to a 2 inch thick layer of copper surrounding the detector. This is thirty percent less reduction than at LANL.

The overall reduction of the  $^{40}\text{K}$ -flux from Los Alamos to the WIPP is also varying. The reduction from non-shielded background at LANL to the one in the underground is given as a factor of 14. The spectrum with a shield of 2 inches of copper is only reduced by a factor of 10 from LANL to the WIPP underground. A conservative approach would be to take the lower reduction factor and claim that the  $^{40}\text{K}$  flux is 10 times smaller at the WIPP than it is at Los Alamos. The reduction in the underground from no shield to one inch of copper is 3.9 and the count rate from one inch of copper to 2 inches of copper is 3.4. These factors are comparable which gives evidence for the fact that the shield works as expected and the contamination is inside the copper shield. Considering the much lower underground reduction factors in Table 4.16 it seems unlikely that what is seen is intrinsic contamination to the detector. It can be concluded that the inner shield surface and/or air was contaminated with salt dust. This limits the  $^{40}\text{K}$  rate reduction factor from a non-shielded detector above ground to a detector which is shielded by 2 inches of copper and 4 inches of lead to 9000.

The attempt to extract a potassium contamination in the salt can be made as follows. The total unshielded rate of the potassium peak in the energy spectrum at WIPP is  $1.17 \pm 0.01 \text{ Hz}$ . The amount of potassium atoms in the detectable range of

Name		LANL			WIPP				
		bk_10k	Cu_50k	Pb_100k	noshield	Cu_1in	Cu_2in	pbsum	wax1
LANL	bkg_10k	1	18	NA	14	56	192	9000	NA
	Cu_50k		1	NA	0.77	3.0	10	490	NA
	Pb_100k			1	NA	NA	NA	NA	NA
WIPP	noshield				1	3.9	13	630	NA
	Cu_1in					1	3.4	160	NA
	CU_2in						1	47	NA
	pbsum							1	NA
	wax1								1

**Table 4.18:** Reduction rates for the  $^{40}\text{K}$  peak for all spectra. The table provides the reduction factor for each spectrum to each spectrum. The rate in the spectrum of the line is by that factor larger than the spectrum shown in the column. In the rows where NA is quoted the  $^{40}\text{K}$  peak could not be distinguished from the background.

the germanium detector can then be calculated as

$$N = \frac{R \ln 2}{t_{1/2, \text{eff}_{det} \text{eff}_{\gamma} m_r}} \quad (4.19)$$

with  $N$  as the total number of potassium atoms,  $R$  the measured decay rate in the peak,  $t_{1/2}$  the half live of  $1.277 \times 10^9$  y,  $\text{eff}_{det}$  the efficiency to detect the 1.4 MeV gamma,  $\text{eff}_{det} = 22 \pm 1\%$ ,  $\text{eff}_{\gamma} = 10.6 \pm 0.05\%$  is the branching ration of the  $^{40}\text{K}$  1.4MeV gamma branch and  $m_r$  as the abundance of  $^{40}\text{K}$  in K with 0.0117. With these numbers N can be derived as

$$N = 2.46 \pm 0.11 \times 10^{22}. \quad (4.20)$$

To determine the number of salt molecules in the same region the following formula was used:

$$N_s = \frac{V \rho N_a}{Z}. \quad (4.21)$$

Here  $V$  represents the gamma ray contributing volume,  $\rho$  the density of the salt with  $2.3 \pm 0.1$ ,  $N_a$  the Avogadro constant of  $6.022 \times 10^{23}$  and  $Z = 58.35$  the molecular weight of NaCl in units U. It is obvious that one has to make a few assumptions for the volume  $V$ . The assumptions made here are:

- The germanium detector has a cylindrical shape with a radius of  $r = 2.5 \pm$

0.01cm and a height of  $4.0 \pm 0.1\text{cm}$

- The volume in the salt contributing to the gamma ray flux is calculated by the area of the detector cross section times the attenuation length  $\lambda = 8.4 \pm 0.1\text{cm}$  for NaCl.

This way  $V$  can be calculated as

$$V = 2\lambda (r^2\pi + 2rh) \quad (4.22)$$

$$= 1000 \pm 62\text{cm}^3 \quad (4.23)$$

Combining this with equation 4.21 one obtains

$$N_s = 2.36 \pm 0.18 \times 10^{25} \text{ and} \quad (4.24)$$

$$\frac{N}{N_s} = 1.04 \pm 0.09 \times 10^{-3} \quad (4.25)$$

With the mass ratio of K to NaCl one obtains a mass ratio of

$$C = 694 \pm 61 \frac{\mu\text{g}}{\text{g}}. \quad (4.26)$$

The error on this number does not reflect the error on the volume assumption, this can be different. However the number calculated is close to the numbers achieved by the CEMERC-team [WEB98]. Their radio assay measurements revealed  $784 \frac{\mu\text{g}}{\text{g}}$  of potassium in the salt.

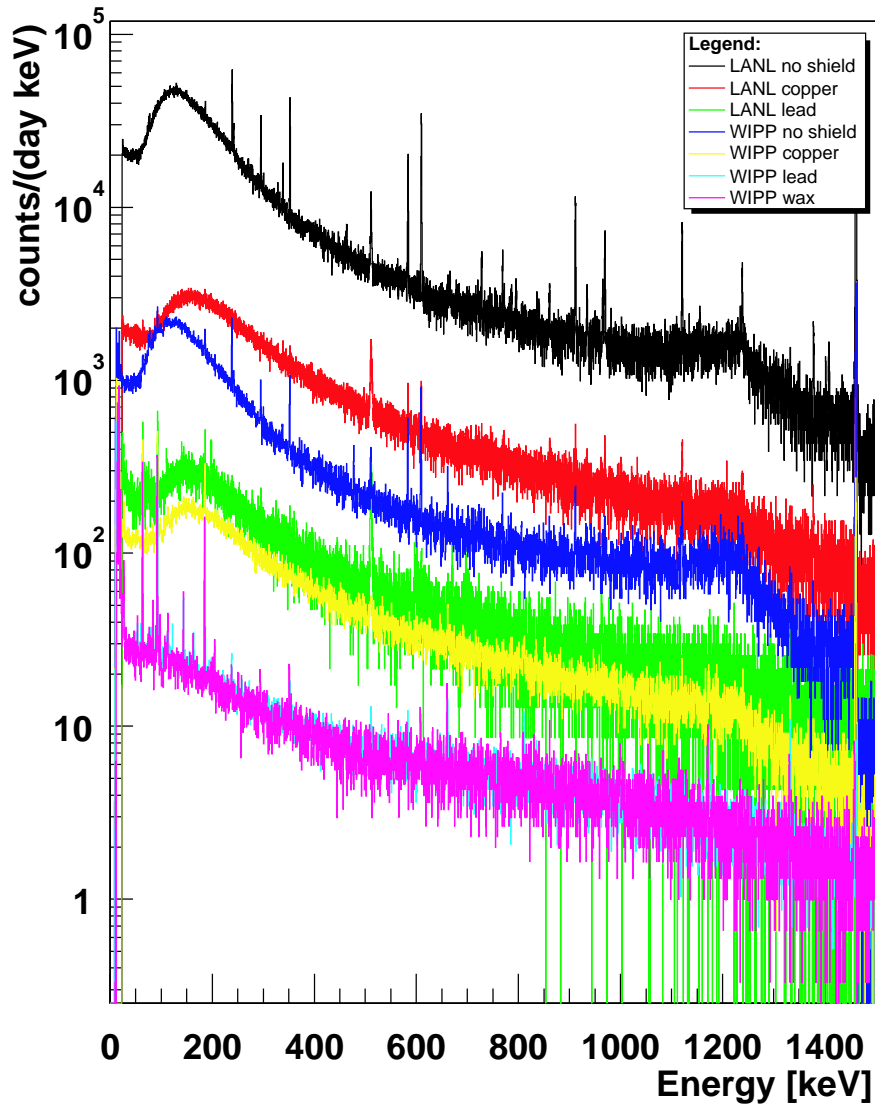


**Figure 4.19:** All spectra taken with the Ge detector. The figure shows the surface and underground spectra measured with the germanium detector in comparison. It is visible that the spectrum with the wax shield is no different than that with lead and copper only.

## 4.6 MUON BACKGROUND AT THE WIPP

### 4.6.1 EXPERIMENTAL SETUP

The experiment to measure the muon flux in the underground of WIPP was conducted 650 meters below the surface in Q-Area (see Figure 4.6). The Detector consisted of two plastic scintillator paddles each 304.8 *cm* long, 76.2 *cm* wide and 2.56 *cm* thick. Each paddle had two light-guides mounted on the two narrow ends. A 12.7*cm*-diameter photo-tube with an operating voltage of 800 volts was mounted on each light-guide thereby a double ended readout was possible. The efficiencies of the photo-tubes were tested by demanding a coincidence in two separate photo-tubes placed with each having its own scintillator atop and below the large paddle (see figure 4.20). Every time a muon did pass the two scintillators a coincidence occurred between the top and bottom photo-tube and the signals from the two photo-tubes on the large panel were acquired. When a coincidence event from the test tube occurred a counter was triggered and the output of the two photo tubes from the big scintillator were acquired. Each position was tested with 10,000 coincidence events. After the test the signal heights from the two large scintillator photo tubes were combined by adding the up and the events above 3*MeV* were counted. Each position on both paddles displayed a total count rate of 10,000 counts at each test position. The two test-tubes were placed in three different positions on the paddles width and on 5 different positions on the panels length. Figure 4.20 shows the positions of the test-tubes on the panel. The result was a detector efficiency for a muon in the scintillator of >99%. Panel 1 was then mounted on top of the lower panel in a distance of 30.5 *cm* (see figure 4.21). A four way coincidence was required to record the four pulses from the photo-tube. The high voltage on each photo-multiplier (PMT) was chosen in such a way that the pulse-height in all photo-tubes for a  $^{90}\text{Sr}$  source in the middle of the panel was of equal value. The ADC recorded the pulse height of each signal. In addition to the four pulse-heights, the time of the event was recorded. As can be seen from figure 4.22 the signal from each PMT was amplified by a factor of twenty. The pre-amplifier signal had a rise time of 10 to 20*ns*. It was then split up and the data signal was fed through a spectroscopic amplifier with a shaping time of 0.25 $\mu\text{s}$  and connected to an AD811 ADC. The other signal was put into a discriminator with a 175*mV* threshold which is equivalent to an energy of 1.1*MeV*. The steep NIM pulses from the discriminators were used as input for a coincidence unit. Figure 4.23 displays the timing used for electronics. The coincidence demanded a quadruple coincidence meaning each photo tube had to see a signal. The coincidence window had a

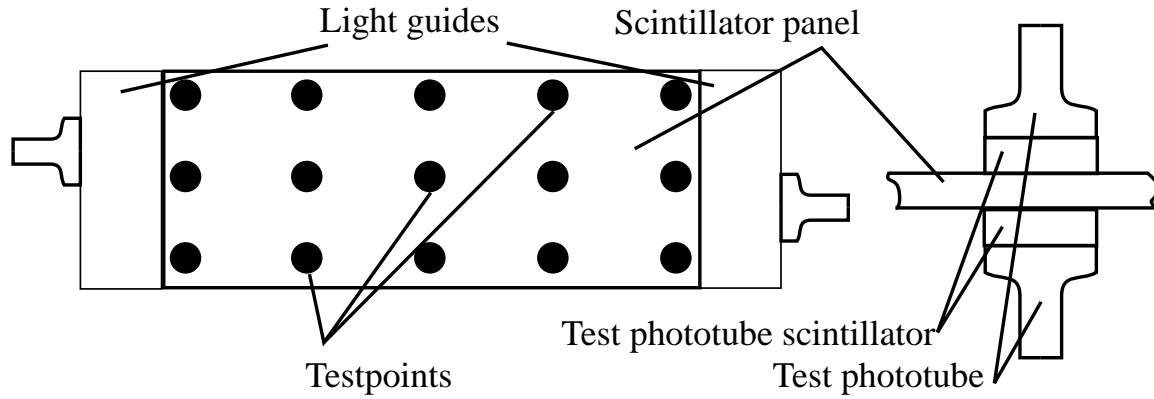


**Figure 4.20:** Setup of the efficiency test. The left side shows the panel setup, each dot marks the test positions on the large panel. On the right side the schematic setup of the test photo-tubes is displayed.

width of  $100ns$ . The output of the coincidence was then processed by a gate/delay generator and used as strobe for the ADC. The strobe window was chosen to be  $.5\mu s$  wide. This ensured that the peak from the spectroscopic amplifier was inside the ADC strobe window.

#### 4.6.2 DATA ANALYSIS

The experiment was conducted during a run-time of 532800 seconds. Figure 4.24 shows the raw coincidence data from each photo tube. It is visible that panel one has a slightly better resolution than panel two. This is the result of photo tube 3 which has the most noisy spectrum (see figure 4.24). The total charge in a panel was calculated as the sum of the outputs of the two attached PMTs. The energy calibration was done by fitting the maximum of the muon peak to the maximum of the Monte-Carlo for the detector. The Monte-Carlo was done in Genat 4. The input parameters for the Monte-Carlo assumed the energy distribution of muons at the surface by the spectrum from the formula cited in [WOL73]

$$N(p) dP = AP^{-\alpha} dP, \quad (4.27)$$

with

$$\alpha = 0.5483 + 0.3977 \ln P \quad (4.28)$$

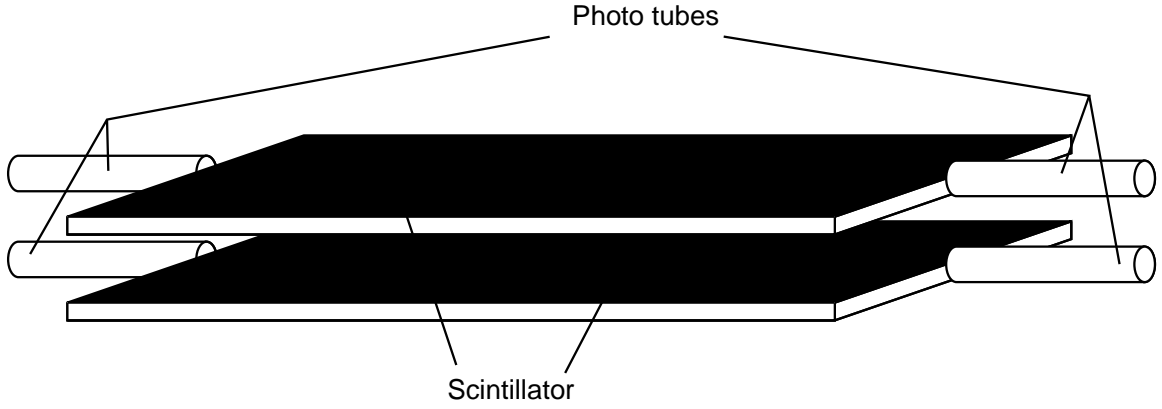


**Figure 4.21:** Setup of the scintillator panels. They were placed on top of each other with a distance of 30cm.

$$A = 3.09 \times 10^{-3} \text{ cm}^{-2} \text{ s}^{-1} \text{ sr}^{-1} (\text{GeV}/c)^{-1} \quad (4.29)$$

and  $P$  being in  $\frac{\text{GeV}}{c}$ . The intensity distribution of  $\theta$  was taken from equation 4.12. The angular distribution for medium depth is displayed in equation 4.13. In a less complex way it can be written as [MIY73]

$$\Phi(h, \theta)_s = \Phi(h, 0) \cos^n \theta \quad (4.30)$$

$$n = 1.53 + 8.0 \times 10^{-4} h \quad (4.31)$$

with  $\theta$  as the polar angle and  $\Phi(h, \theta)$  as the flux for a specific angle in  $\text{cm}^{-1} \text{ s}^{-1} \text{ sr}^{-1}$ . The data and Monte-Carlo in Figure 4.25 displays the calibrated energy spectrum in both panels. The total muon spectrum for each panel was achieved by adding the ADC values of both photo tubes up on an event-by-event base. This optimizes the muon signal and the muon peak rises above the PMT-noise. Then the Monte-Carlo was used to fit the measured muon peak in the energy spectrum to the simulated energy spectrum. The small discrepancies between the spectrum shape and the Monte-Carlo are due to extrapolation errors in the energy spectrum and the analytical approach to calculate the average energy loss through limestone and salt. The muon peak with its maximum around  $4.8 \text{ MeV}$  is clearly visible. The Monte-Carlo was corrected for the energy resolution in the two panels, smeared out randomly on an event by event base. This was done by smearing each energy deposition with a random Gaussian distribution. The mean of the distribution was

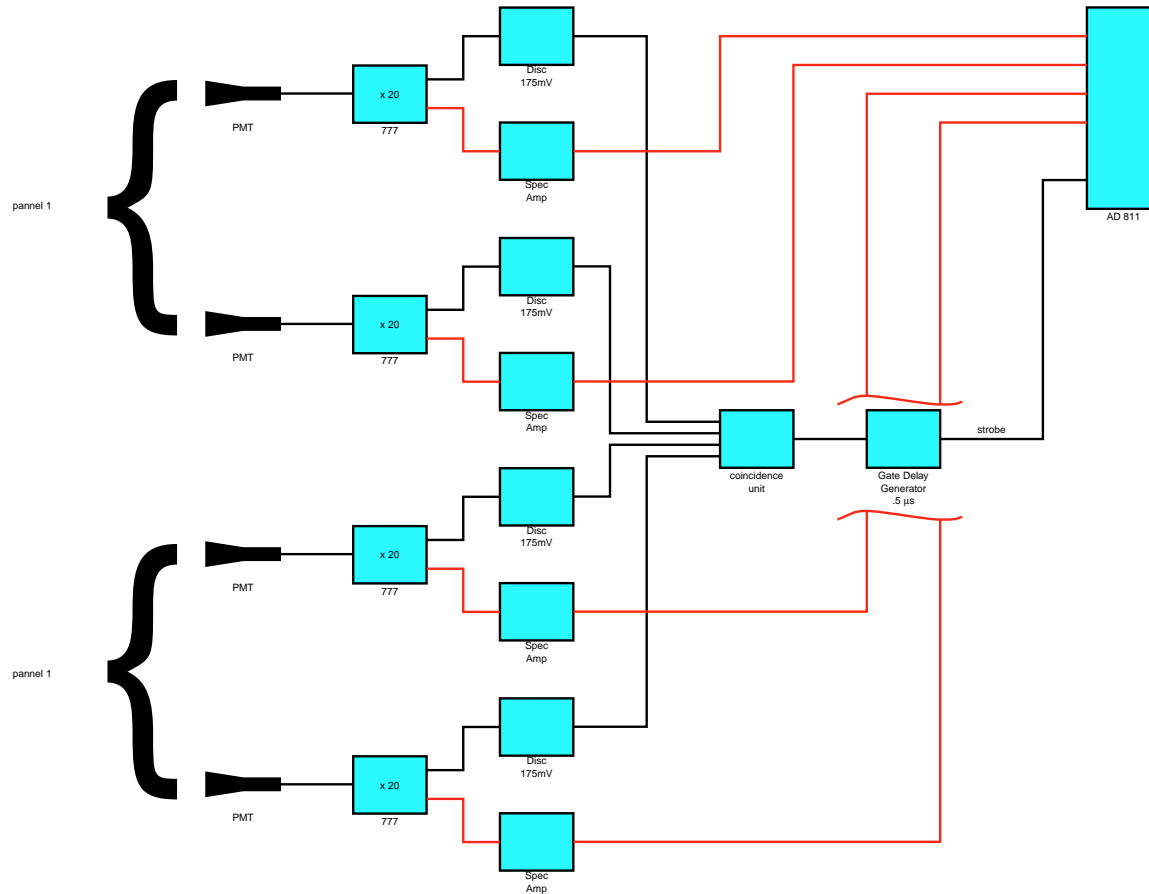


**Figure 4.22:** Setup of the scintillator-electronics. The electronics was setup in a quad coincidence mode.

the energy deposited and the sigma was calculated as

$$\sigma = \sigma_0 \sqrt{\frac{E_{dep}}{1 MeV}}. \quad (4.32)$$

Data sets for  $\sigma_0$  between 0 and 100% were created and the energy histogram that fitted the data in each panel best was chosen for the energy calibration.

The absolute muon number for the flux calculation was obtained as follows. Figure 4.26 shows a two dimensional plot of an event by event energy distribution for the two panels. The x-axis shows the energy deposition in the lower panel the y-axis the energy deposition in the upper panel. The muon peak is clearly visible

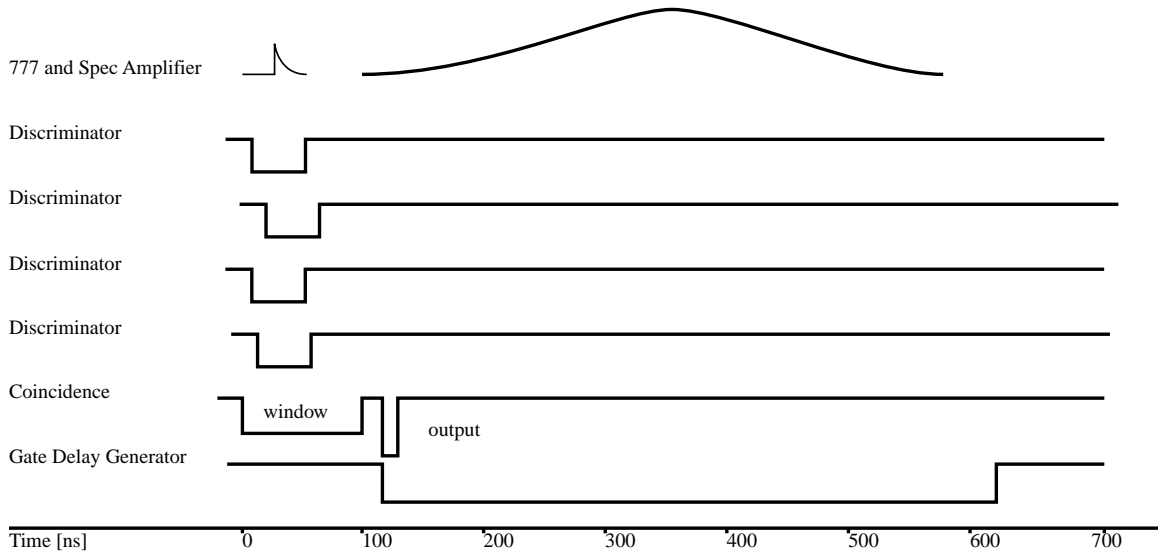


Figure 4.23: Timing of the scintillator Coincidence.

as the blue events. A cut above  $2MeV$  energy deposition for each panel was chosen to determine the muon number. Figure 4.27 shows the same cut applied to the Monte-Carlo simulations. From the Monte-Carlo one can derive that the number of muons outside the cut region represent  $1.24 \pm 0.01\%$ . This number is due to edge effects and muon spallation products. An edge effect is an event that deposits less energy in one panel due to clipping an edge and thereby reducing the path length in the detector to less than the thickness of the panel. The cut is represented by the blue event markers. The black line shows the cutting border in both figures. Comparing figure 4.27 with figure 4.26 one can see that the area where both energies are smaller than  $2MeV$  has no events in the simulation whereas these events exist in the real data plot. These low energy events are due to the random coincidence noise of the PMTs. Table 4.19 shows the different cuts applied to the muon spectrum. The errors quoted are purely statistical errors. The total muon peak cut is shown by cut 4 and the muon number derived from the cut is

$$N_{\mu} = 5202 \pm 72, \quad (4.33)$$

where the uncertainty is statistical only.

Figure 4.28 shows the total calibrated energy spectrum from the two panels. The blue spectrum represents the energy histogram achieved due to the cut shown in figure 4.26.

Cut Upper Panel	Cut Lower Panel	Events	Count rate [Hz]
—	—	11226± 106	2.11±0.02 × 10 <sup>-2</sup>
E<2MeV	—	5881±77	1.10±0.014 × 10 <sup>-2</sup>
—	E<2MeV	5350±73	1.00±0.014 × 10 <sup>-2</sup>
E>2MeV	—	5345±73	9.7±0.14 × 10 <sup>-3</sup>
—	E>2MeV	5876±77	9.8±0.14 × 10 <sup>-3</sup>
E>2MeV	E>2MeV	5202±72	9.9±0.14 × 10 <sup>-3</sup>

**Table 4.19:** Cuts applied to determine event numbers in muon peak.

The next step is to determine how many counts of the background contributed into the signal and how many counts from the signal were lost into the low energy background due to the cut. To be able to see the low energy background the threshold was turned down as low as possible without having the random coincidence rate overwhelming the energy spectrum. The trigger rate coming from two photo tubes in one panel in coincidence was measured to be 220Hz. Therefore the data was taken demanding a quadruple coincidence. With the event rate from two panels in coincidence one can calculate the produced random coincidence rate with

$$\nu_r = 2\nu_1\nu_2\tau \quad (4.34)$$

where  $\nu_r$  is the random coincidence frequency,  $\nu_1$  and  $\nu_2$  the two frequencies and  $\tau$  the coincidence window. With a rate of  $220 \pm 10\text{Hz}$  and a coincidence window of  $100 \pm 5\text{ns}$  the rate can be calculated to

$$\nu_r = 9.68 \pm 0.79 \times 10^{-3}. \quad (4.35)$$

This can be converted in a total count rate of

$$R = 5158 \pm 43 \text{ counts}. \quad (4.36)$$

Since the main part of the background can be accounted towards random coincidence the tail of the background was assumed to be an exponential tail in the shape

of

$$F = e^{ax+b}. \quad (4.37)$$

To determine the contribution of counts from the background into the cut energy region and the contribution of muon events into the background region an exponential fit of the background and signal tail was made after the data were cut the following way. The event in the lower panel were cut above  $2MeV$  and the signal from the upper panel was plotted into a histogram. Then the background tail of the upper panel was fit to an exponential. For the histogram of the lower panel the process was inverted. The fit over the lower part of the background was made and the fitted function was then integrated. The integration interval for the background was from  $2MeV$  to  $30MeV$ . Table 4.20 shows the tail name, the fitted coefficients  $a$  and  $b$ , the interval of the fit and the contributing events under the tail. The events under the tail were calculated by using the integral multiplied by the number of bins per  $MeV$  (in this case 10). One can see that the signal in the upper panel has a better resolution which shows in the smaller tail contribution of the background of 20 counts instead of 40 from the lower panel. The contribution of the signal into the background was taken from the Monte-Carlo by applying the cut displayed in figure 4.27. To be able to calculate a muon-flux from the detector

Tail Name	$a$	$b$	Fit Interval	counts
Monte-Carlo cut off	—	—	0– $2.0MeV$	62
background upper panel	-3.10	8.03	1.2– $2.1MeV$	20
background lower panel	-1.30	4.39	1.0– $2.4MeV$	40

**Table 4.20:** Tail fits of the background and muon signal.

data it is necessary to know the total geometric efficiency of the detector. The flux can be calculated as follows.

$$\Phi_{total} = \frac{N_0}{e \cdot a \cdot t_{rt}}, \quad (4.38)$$

where  $\Phi_{total}$  is the total flux of muons through the panel,  $N_0$  the measured number muons,  $e$  the efficiency of the detector which includes both the physical efficiency of the scintillator and the geometrical efficiency due to the setup of the detector and the angular distribution of the muons,  $a$  the area covered by the detector (2.33

$m^2$ ) and  $t_{rt}$  the run-time of the experiment which was 532800 seconds.

The geometric efficiency was calculated by using a Monte-Carlo written with the Geant 4 package. The simulated geometry included the two 2.54 *cm* thick scintillator panels with a separation of 30.48 *cm* surrounded by a box. The start-position for the muons were randomly chosen on a surface, 10% longer in each direction than the panel dimensions, located just above the surface of the first panel to include edge effects. The direction was sampled by randomly taking  $\phi$  in an interval between 0 and  $2\pi$ . The direction in  $\theta$  was sampled from several different distributions such as,  $\cos^n \forall n$  in  $[0 \dots 4]$  and the distribution from equation (4.12) for a depth of 650 meters and a density  $\rho$  varying from 1.6 to 3.3  $\frac{g}{cm^3}$ . The determination of the geometric muon-efficiency was calculated by dividing the number of muons having gone through both panels and having deposited an energy in the region of cut 4 in table 4.19 by the number of muons depositing energy in the first panel. Figure 4.29 shows the efficiencies for different densities  $\rho$ . With a measured density of 2.3  $\frac{g}{cm^3}$  [LAB95] and the assumption that the error is not bigger than  $\pm 0.2 \frac{g}{cm^3}$  one can calculate the efficiency as

$$84.35 \pm 0.4\%. \quad (4.39)$$

The vertical flux can be determined by the distribution of the angle  $\theta$ . Using the formula from equation 4.13 one calculates for a depth of 1495 *m.w.e.* the vertical flux to be

$$\Phi_{vert} = (0.65 \pm 0.04) \times \Phi_{tot} \quad (4.40)$$

## BACKGROUNDS

The following estimation of other backgrounds in this detector are presented to strengthen the argument that what we see are muons. In order to generate a coincidence pulse with an energy deposition of more than the threshold of 2.0 *MeV* one has to look at particles with higher energy.

### NEUTRONS FROM MUONS

Neutrons generated from muons traversing through the rock and salt are the highest energy particles expected in the WIPP underground (see subsection 4.3.2). In his paper Bezrukov [BEZ73] estimates the amount of neutrons per muon ( $\frac{n}{\mu}$ ) gen-

erated at a depth of 1500 meter water equivalent (m.w.e.) in  $\frac{hg}{cm^2}$  as

$$N_{n(\mu)} = 7 \times 10^{-4} \frac{n \text{ cm}^2}{\mu \text{ g}}. \quad (4.41)$$

With equation (4.12) this calculates to a total neutron flux of

$$\Phi_{neutron} = 2.9 \times 10^{-2} \frac{n}{kg \cdot d} \quad (4.42)$$

To derive the flux of the neutrons in the detector the following linear assumption was made. With an assumed attenuation length of  $200 \frac{g}{cm^2}$  the neutron flux calculates to

$$\Phi_{neutron} = 58 \frac{1}{m^2 \cdot d} \quad (4.43)$$

Several Monte-Carlos generated to simulate the neutron coincidence in the existing detector symmetry show a total detector efficiency of up to 0.36%. With the experimental lifetime of 532800 seconds and a detector surface of  $2.33 \text{ m}^2$  the total muon-count expected within the duration of the experiment in the panel is

$$N_{neutron} = 3. \quad (4.44)$$

#### NEUTRONS FROM U AND TH

As discussed in subsection 4.3.2 natural radioactivity is present in every geological layer in the earth. An abundance of uranium and thorium in the salt is able to generate neutrons via  $(\alpha, n)$ -reactions and through spontaneous fission. The U and Th contents in the WIPP underground has been measured [WEB98] and are displayed in table 4.21. With the numbers for neutron production of  $(\alpha, n)$ -reaction and spontaneous fission of U and Th in salt from [FLO88] (table 4.5) one can calculate the neutron production rate in the Salt of the WIPP mine. The uranium and thorium numbers for the two different salt data were used to generate a neutron rate per day,  $kg$  and  $ppm$ . These values were then used to calculate the neutron production in the WIPP salt again in units of  $\frac{1}{kg \cdot d}$ . Table 4.22 shows the data. The data is displayed as calculated values for the two different salt measurements of table 4.5 and the two measurement from table 4.21.

The highest rate from table 4.22 was used for U, Th and Fission processes to determine an upper limit for the event rate in the scintillator. As mentioned above the efficiency of the detector is 0.36%. The attenuation length is  $1.2 \text{ cm}$  [NIS01]. With

Element	at the WIPP			Range in Soil			Ratio
	Mass Spec. [ $\frac{\mu g}{g}$ ]	Gamma Spec. [ $\frac{\mu g}{g}$ ]	Avg [ $\frac{\mu g}{g}$ ]	low [ $\frac{\mu g}{g}$ ]	high [ $\frac{\mu g}{g}$ ]	typical [ $\frac{\mu g}{g}$ ]	Soil vs. WIPP
Uranium	0.048	<0.37	0.048	0.5	2.5	1.5	30
Thorium	0.08	0.25	0.25	1.2	3.7	2.4	10
Potassium	784	182	480	500	900	700	1.5

**Table 4.21:** Natural Radioactivity at the WIPP underground [WEB98].

these numbers it is possible to calculate the expected event rate in the detector as

$$N = 2 \times \Phi_n \times t_r \times A \times \lambda \times \rho \times eff, \quad (4.45)$$

where  $N$  is the measured number of neutrons in the detector during the experiment,  $\Phi_n$  the neutron flux per  $kg d$ ,  $t_r$  the runtime of the experiment,  $A$  the area of the detector,  $\lambda = 1.2 cm$  the attenuation length of the neutrons,  $\rho = 2.3 \frac{g}{cm^3}$  the density of the salt. The factor of 2 is due to the symmetry of the detector. The following numbers can be achieved

$$\begin{aligned} N_U &= 93, \\ N_{Th} &= 14 \text{ and} \\ N_{fission} &= 1.3 \end{aligned} \quad (4.46)$$

Process	Salt I		Salt II	
	Mass Spec. [ $\frac{1}{kg d}$ ]	Gamma Spec. [ $\frac{1}{kg d}$ ]	Mass Spec. [ $\frac{1}{kg d}$ ]	Gamma Spec. [ $\frac{1}{kg d}$ ]
U	0.73	4.38	4.2	32.5
Th	5.04	3.65	0.08	0.26
Fiss.	0.065	0.48	0.06	0.46

**Table 4.22:** Calculated neutron fluxes at WIPP.

## GAMMA BACKGROUND

The highest level of gamma background comes from the  $^{40}\text{K}$  in the Salt. The abundance of potassium in the salt is  $784 \frac{\mu\text{g}}{\text{g}}$  (table 4.21) which can be calculated to an abundance of  $1.5 \cdot 10^{14}$   $^{40}\text{K}$  atoms per gram of salt that will decay in the branch of the  $1.46 \text{ MeV}$   $\gamma$ -ray. With a half-life of  $T_{\frac{1}{2}} = 1.28 \times 10^9 \text{ y}$  this averages to a decay rate of approximately  $1.3 \cdot 10^{-3}$  Atoms per second per gram of salt. With the macroscopic scattering cross section from [BER01] of  $5.02 \cdot 10^{-2} \frac{1}{\text{cm}^2}$  in NaCl the attenuation length of  $\lambda = 8.6 \text{ cm}$  is computed. The amount of salt contributing gamma rays can then be estimated as  $197.8 \frac{\text{kg}}{\text{m}^2}$ . That calculates to a flux of

$$\Phi_{\gamma} = 257.1 \frac{1}{\text{s m}^2}. \quad (4.47)$$

Since each  $\gamma$ -ray can only deposit a maximum of  $1.46 \text{ MeV}$  a quadruple coincidence in the detector is required to generate a signal high enough in energy to be in the muon-cut region. With a coincidence window of  $100 \text{ ns}$  the coincidence rate turns out to be  $10^{-4}$  counts in the detector during the whole experimental lifetime.

## 4.6.3 THE MUON-FLUX

The raw data reveal a count rate of

$$R = 5202 \pm 72 \quad (4.48)$$

events in the cut region. Subtracting the tails and adding the error one obtains

$$R = 5214 \pm 72 \begin{smallmatrix} +40 \\ -52 \end{smallmatrix}. \quad (4.49)$$

The neutrons are put into the count rate as an error of  $-90$  (see table 4.23) and the efficiency comes in with an error of  $\pm 52$  this results in a rate of

$$R = 5214 \pm 72 \begin{smallmatrix} +40 \\ -52 \end{smallmatrix} - 111 \pm 52. \quad (4.50)$$

With the geometric efficiency the systematic, the tail and the efficiency errors change whereas the error from neutron stays. Therefore the count rate can be written as

$$R = 6789 \pm 85 \begin{smallmatrix} +47 \\ -61 \end{smallmatrix} - 111 \pm 67 \text{ and by combining the errors} \quad (4.51)$$

$$R = 6789 \begin{smallmatrix} +118 \\ -166 \end{smallmatrix}. \quad (4.52)$$

Name of parameter	Contribution
Runtime of the experiment	532800 seconds
Cut of muon peak	5202±72 Events
Fit of background tails into the signal	-40 Events
Monte-carlo of events in background	+52 Events
Monte-carlo calculation of U, Th, fission events	± 108 Events
Monte-carlo calculation of neutrons generated by $\mu$ 's	±3 Events
Detector Efficiency	100 ± 1%
Detector Efficiency (geometric)	84.25% ± 0.4%
Conversion factor to vertical flux	0.65 ± 0.04

**Table 4.23:** The contributing parameter for the muon flux.

With this count rate the muon flux can be calculated

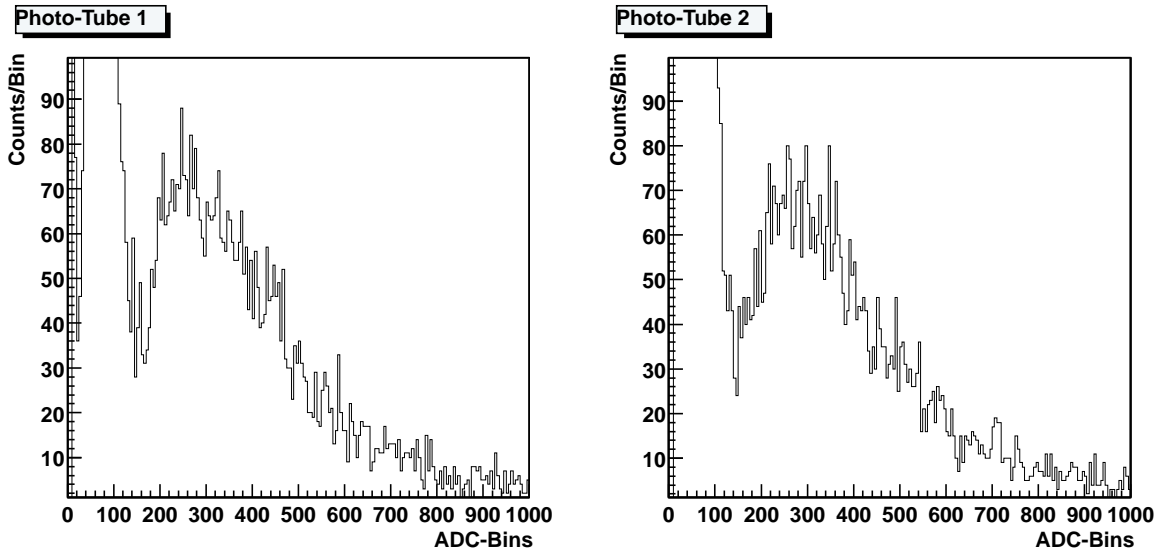
$$\begin{aligned}
 \Phi_{tot} &= \frac{6789^{+118}_{-166}}{532800 \text{ s} \times 23225 \text{ cm}^2} \\
 &= 5.00^{+0.10}_{-0.14} \times 10^{-7} \frac{\text{Hz}}{\text{cm}^2}
 \end{aligned} \tag{4.53}$$

With equation 4.40 This flux can now be converted to a vertical flux of

$$\Phi_{vert} = 3.25^{+0.07}_{-0.10} \times 10^{-7} \frac{\text{Hz}}{\text{cm}^2 \text{ sr}}. \tag{4.54}$$

Measurements made in the past in different underground laboratories in the world ([CRO87], [AMB95] and [AND87]) show similar numbers for this depth. The shallow depth fits within its error bar into the extrapolation of their data points from these experiments. Figure 4.30 shows WIPP in comparison to other underground laboratories. With its average density of  $2.3 \frac{\text{g}}{\text{cm}^3}$  and a depth of 650 meters the WIPP mine muon measurement fits very well with the theoretical predicted data.

### Upper Panel



### Lower Panel

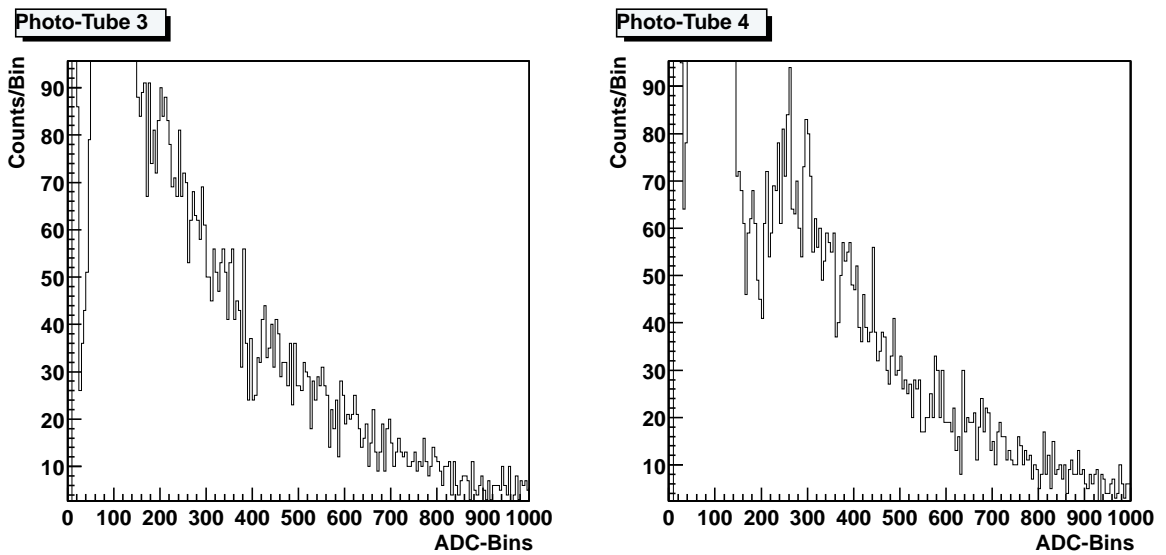
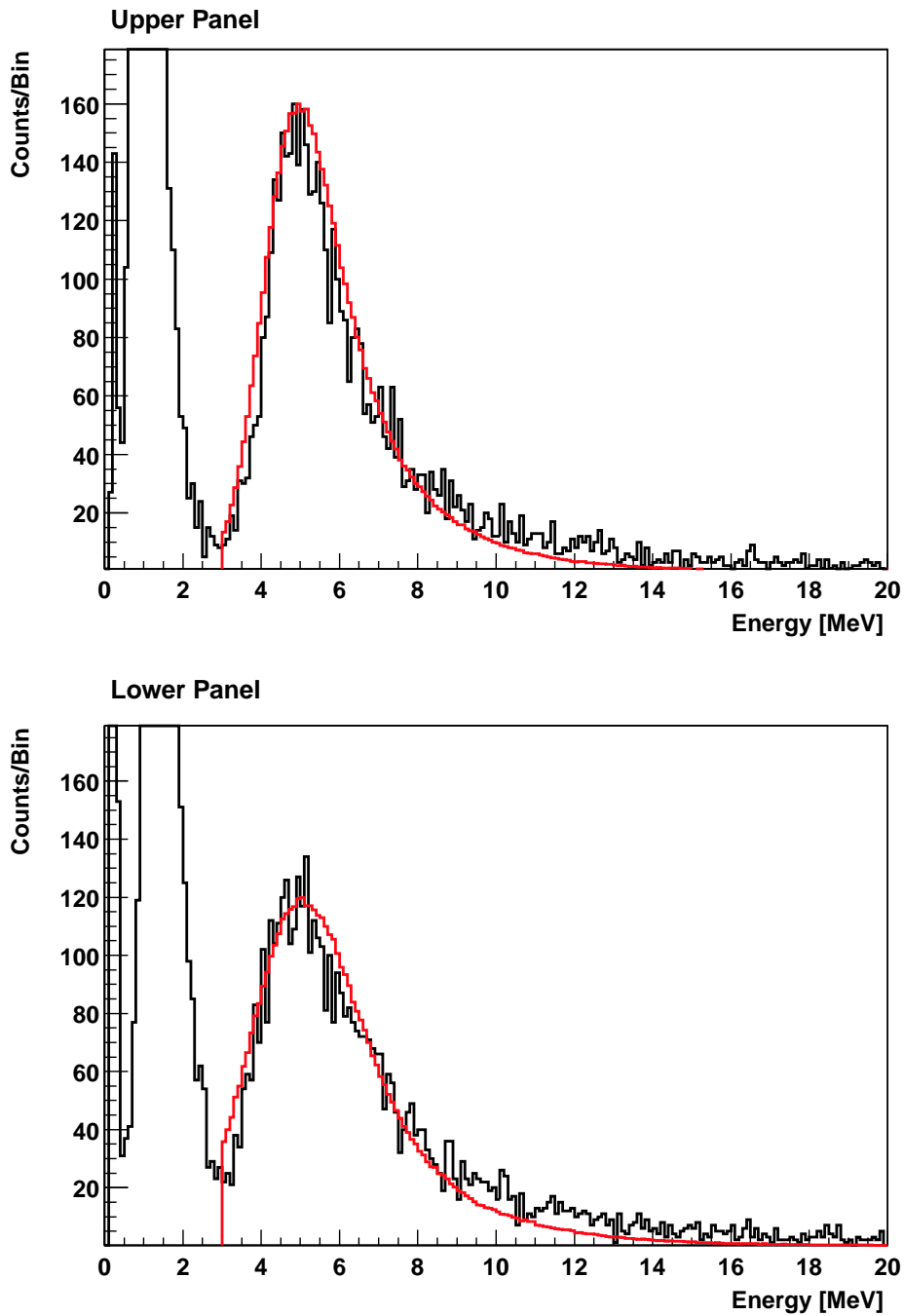
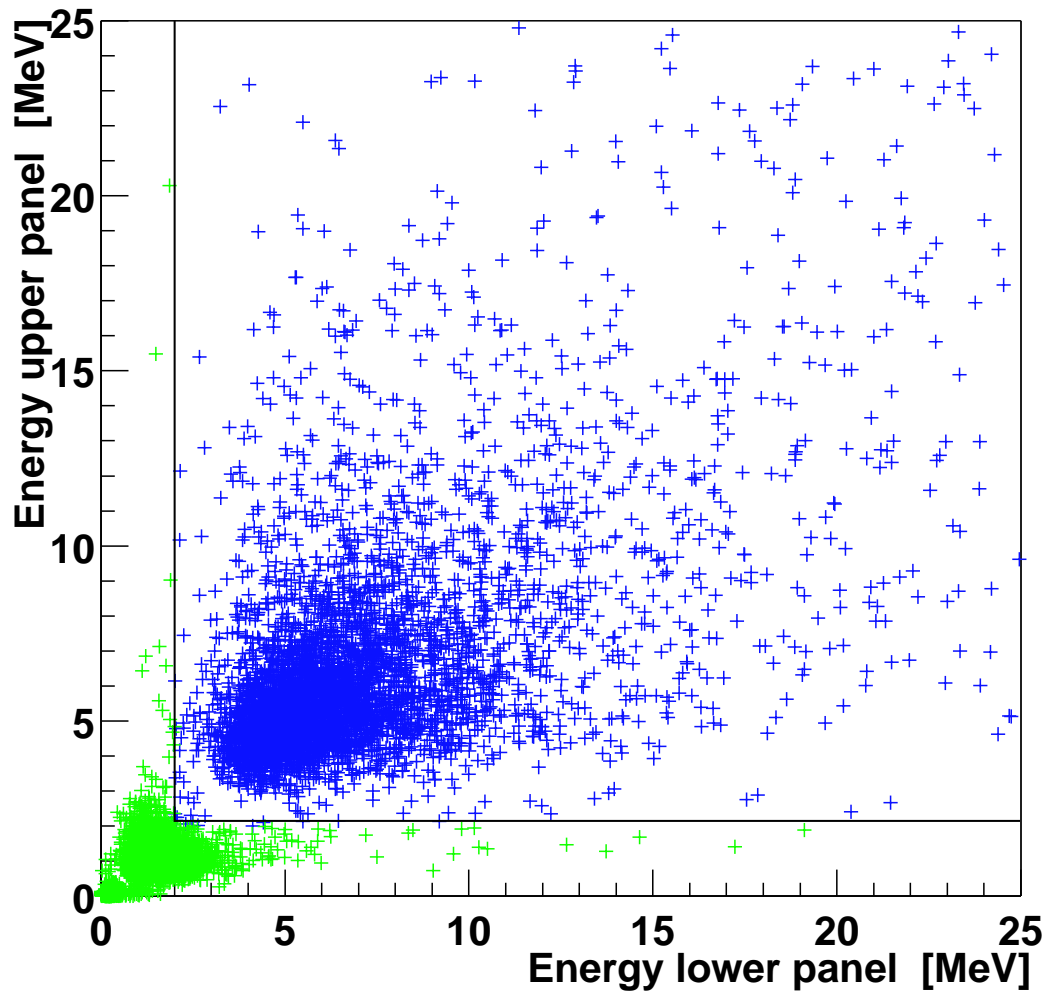


Figure 4.24: Spectrum of the raw data in scintillator.



**Figure 4.25:** Spectrum for the raw energy in the two scintillator panels. The energy is plotted into a histogram in units of  $MeV$ , the Monte-Carlo is shown in red.



**Figure 4.26:** Two dimensional spectrum for the cuts applied to the muons. The spectrum shows on the x-axis the deposited energy in  $MeV$  for the lower panel, on the y-axis the deposited energy for the upper panel. The black line displays the cut chosen for the muon number. The blue events represent the muon peak, the green events are dominated by the random coincidence of the PMTs.

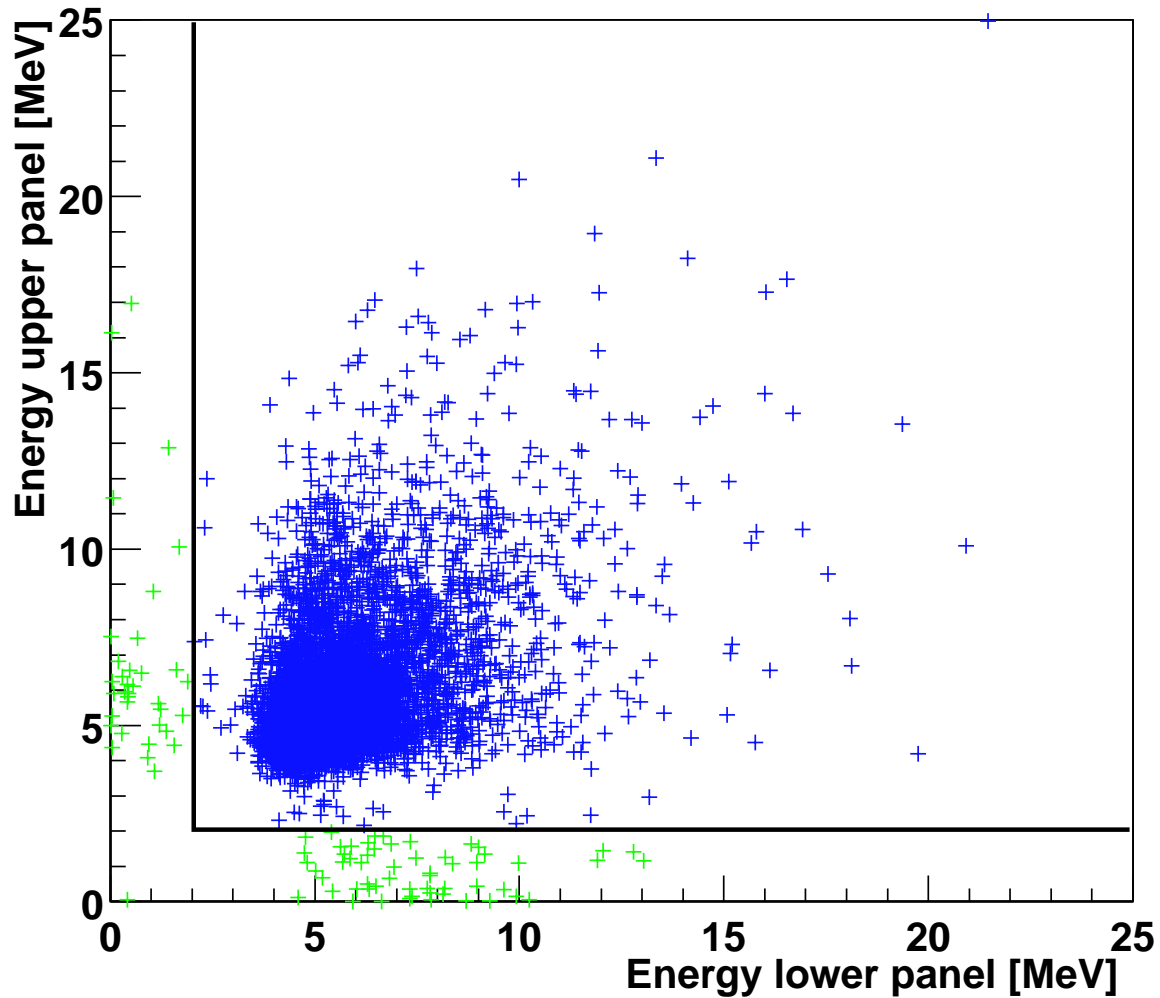


**Figure 4.27:** Two dimensional spectrum for the cuts applied to the muon Monte-Carlo. The spectrum shows on the x-axis the deposited energy in  $MeV$  for the lower panel, on the y-axis the deposited energy for the upper panel. The black line displays the cut chosen for the muon number. The blue events represent the muon peak, the green events represent muons outside the cut region. The ratio of these muons in the simulation is  $1.24 \pm 0.01\%$ .

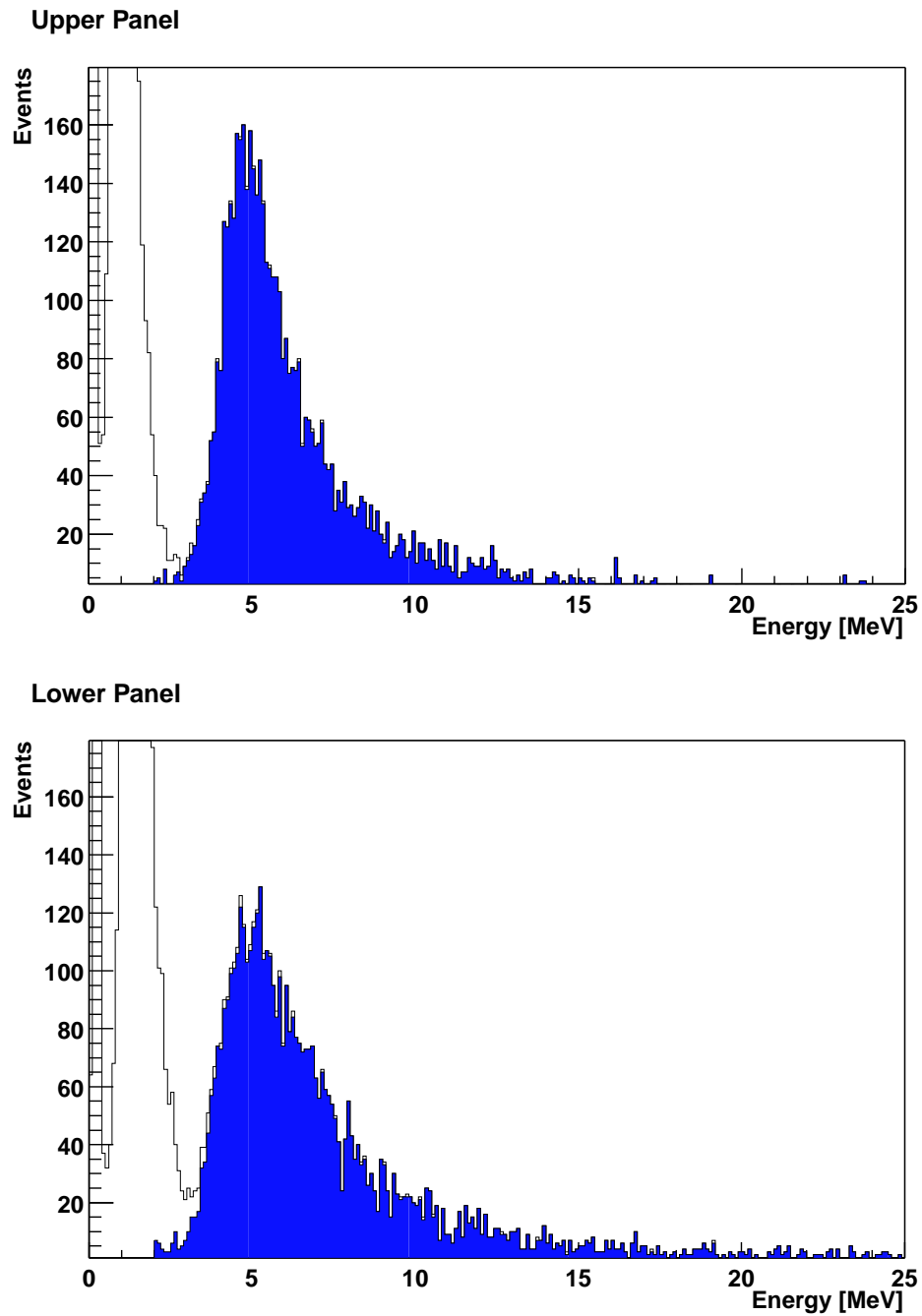


**Figure 4.28:** Energy spectrum of the two panels with spectrum cut. The Energy is displayed in units of  $MeV$ . The blue spectrum shows the remaining spectrum after the  $2MeV$  cut is applied in both panels.

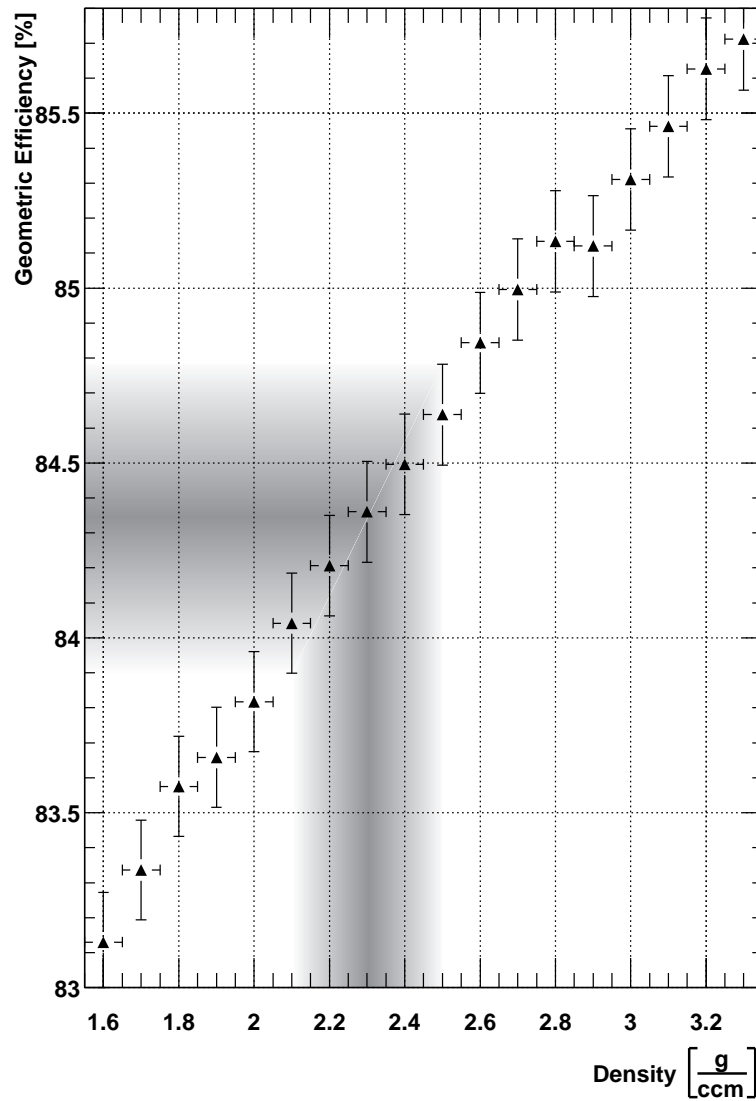


**Figure 4.29:** Geometric efficiency for different densities at the depth of WIPP. The efficiency was calculated by using the Monte-Carlo. The error bars represent the statistical error of the Monte-Carlo.

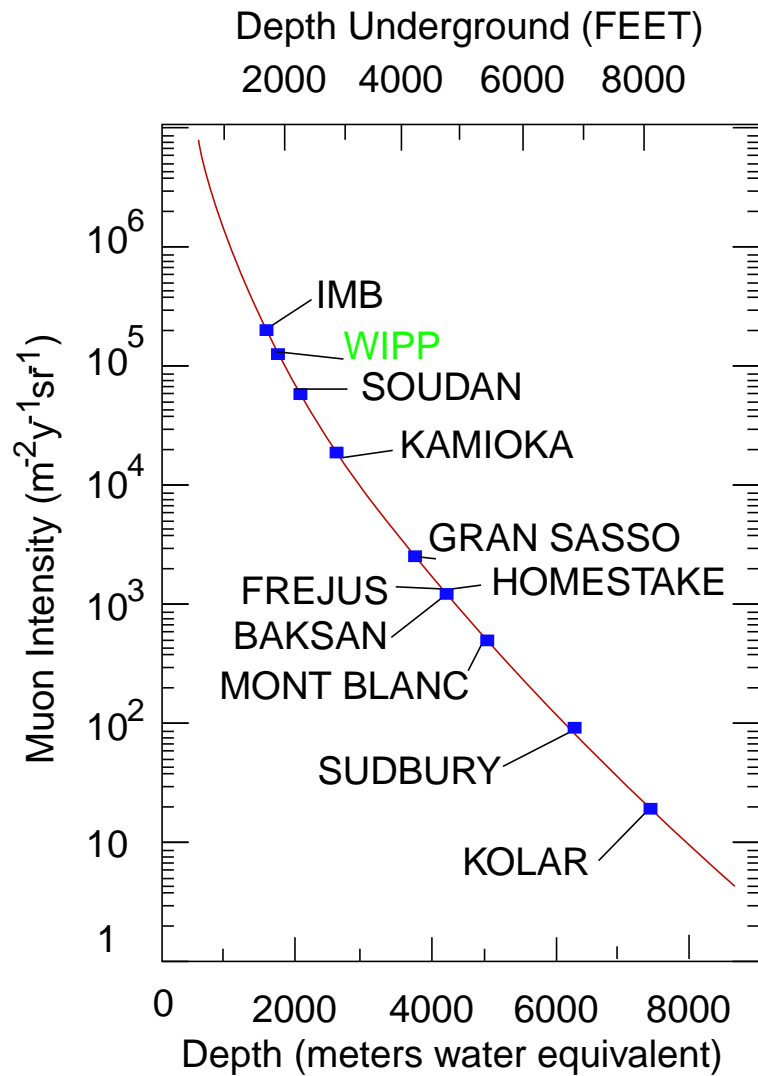


Figure 4.30: Vertical muon flux for different underground experiments.



---

## SUMMARY AND CONCLUSION

---

The silicon prototypes have been tested. The results lead to the conclusion of a surface contamination. Since it was not possible to resolve this problem, a more detailed background analysis for intrinsic background radiation could not be done. However other silicon dark matter experiments with less mass show that main contamination in silicon crystals is generated by three  $\beta$ -decay spectra from  $^3\text{H}$  (18.6keV),  $^{32}\text{Si}$  (225keV) and  $^{210}\text{Pb}$  (63.1keV) [CAL90].  $^3\text{H}$  and  $^{32}\text{Si}$  are produced by cosmic rays.  $^3\text{H}$  in the silicon above ground through bombardment of the silicon itself.  $^{32}\text{Si}$  is generated by cosmic rays interacting with Ar in the atmosphere and the  $^{32}\text{Si}$  is then falling onto the Earth surface [CAL90]. The  $^{32}\text{Si}$  contamination in normal Silicon is expected to be 300 decays per day per kilogram which is an abundance of  $1.18 \frac{10^{-18}g}{g}$ .

This contamination is intrinsic to the detector and can be prevented by using silicon sand that has been mined out of a geological old layer of sand or stone underground. The contribution of  $^{32}\text{Si}$  background is also on the same order than the background from the copper shielding around the detector (see table 4.3). Unfortunately the signal in the prototype detector is 6315 counts per day per kilogram which is a factor of twenty higher than the expected count rate from  $^{32}\text{Si}$ . Therefore it was not possible to determine the  $^{32}\text{Si}$  contamination of the silicon. Despite the fact that this background could not be determined sufficiently it is possible to extrapolate an expected signal from a possible full scale detector. With the assumption that the background limit of the detector is reached with a background rate such as measured, one can still calculate the expected WIMP signal. Since it is possible for the group at the Los Alamos National Laboratory to obtain 65kg of these silicon detectors one can try to look at the annual fluctuation of the WIMP signal. With the existing background of 6315 counts per day per kilogram and a mass of 65kg one can calculate a possible limit on WIMPs. Figure 5.1 shows the possible excluded regions for different run times. Assumed is a detector mass of

65kg. With this mass and the assumption for the background to be the same as obtained by the silicon prototypes in WIPP (see figure 3.6) exclusion region for different runtime scenarios were drawn. The black line represents the exclusion curve for a detector with 65kg mass and a runtime of two days, one while the Earth is moving with the sun and one day while the Earth's velocity vector is opposed to that of the sun. The line labeled "65kg 60 days" represents the exclusion area for the same detector mass with a runtime of two months and the line labeled "65kg 690 days" represent the exclusion border for a runtime of twenty months which amounts to a experimental time of 5 years. The reason for the long experiment time is that the velocity of the WIMPs during the time when the earth is moving perpendicular to the direction of the movement of the sun does not change enough to produce a significant rate difference. The line labeled "0.01 c/(d keV) 65kg 60 days" finally represent a runtime of twenty months with 65kg of detector mass and the assumption that the background is dominated by electrical problems and the detector has as low a radioactive background as the best today produced silicon (0.01 counts per day per kilogram per keV).

Since the ability to detect the signal difference is proportional to the square root of the background signal and anti-proportional to the square root of the mass and the runtime of the detector. It is in the future important to decrease the background to the best level achievable. Once this has been done a 65kg silicon detector with a background 0.01 counts per day per kilogram per keV can improve the existing WIMP limits by a factor of 5, probe the mass regime below 1GeV and, more importantly is able to confirm or deny the result from the DAMA experiment.

The background measurements at the WIPP revealed that the uranium and thorium contents in the salt are a factor of 10 to 30 lower than that of average rock. The measurement with the differential shield shows that without veto shielding the background can be reduced by a factor of 50 to 100. Furthermore the neutron flux is reduced to 0.1 neutrons per gram per year by going underground. This reduction represents a factor of thirteen to comparable depth rock mines and a factor of  $10^4$  reduction from the surface flux (see figure 4.3). This makes WIPP a candidate for low background experiments.

The muon measurement performed in the underground at WIPP revealed a total muon flux of  $\Phi_{tot} = 5.00_{-0.14}^{+0.10} \times 10^{-7} \frac{Hz}{cm^2}$ . This represents about 3900 muons per square meter per day. With this muon flux WIPP is slightly better in background than the IMB (Irvine Michigan Brookhaven) site (see Figure 4.30).

With the right veto system for the muons WIPP represents a well fit site to setup a low background detector in the underground. This shield can detect muons on their way through the detector and vetoes signals that are coming in during this

time. The decision whether a low background experiment can be launched at the WIPP depends mainly on its size and the ability to shield the muons. The high energy neutron flux generated from muon spallation is with  $0.01$  neutrons/ $g y$  a factor of 10 smaller than the neutron flux from natural radioactivity but is much harder to shield. This is probably the most important issue for choosing WIPP as an underground laboratory.

A veto shield for muons has an efficiency which is with the current backgrounds responsible for the upper limit of the background rate in the detector. The surface area of the detector matters as well. If the detector is too large, the dead-time of the system will increase. With the knowledge of the muon flux and the reduction rate of the neutrons and gamma rays the WIPP offers a good environment for small scale dark matter experiments and low background prototype testing.

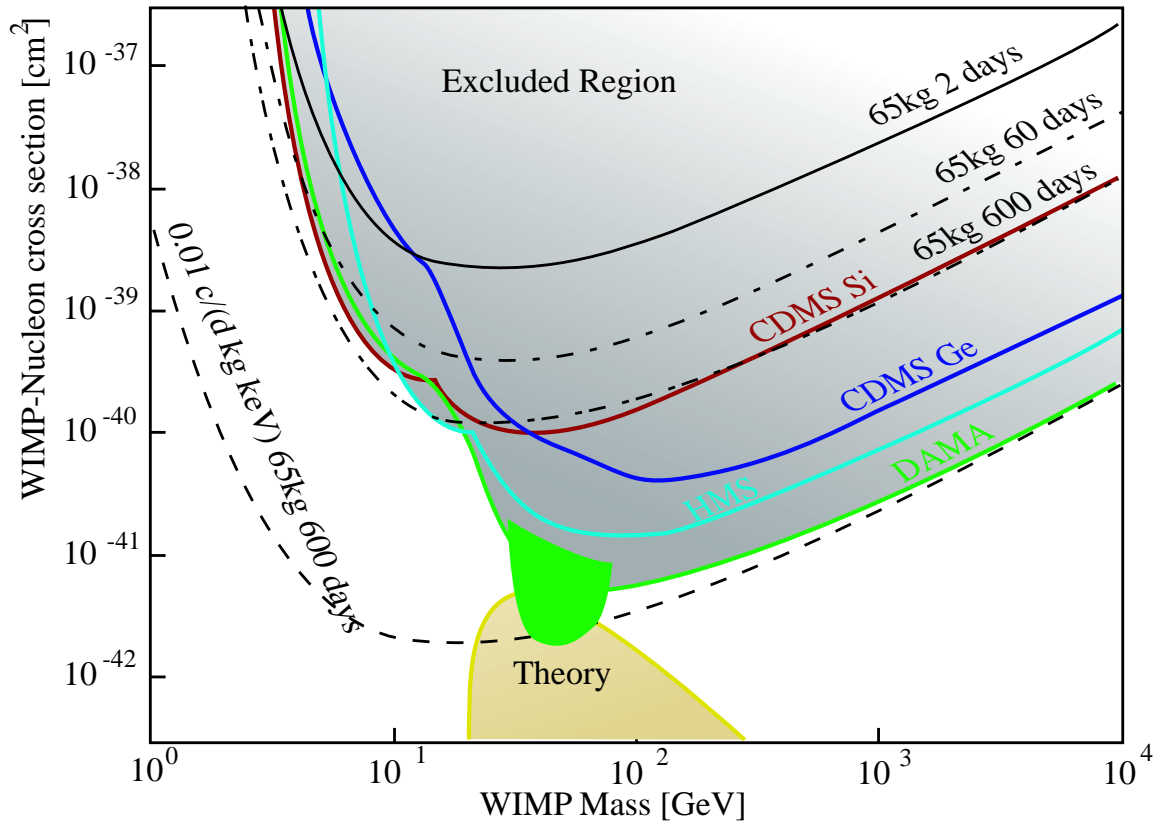


**Figure 5.1:** Possible annual fluctuation signal. With the background from the silicon prototype (see figure 3.6) and a total assumed mass of  $65 \text{ kg}$ . Analysis has been made to calculate the exclusion region for different run times in comparison with already achieved Dark Matter Experiments.

# MANUFACTURING PROCESS OF A COMMERCIAL SOLID STATE DETECTOR

---

Commercial solid state detectors are manufactured out of electronic grade polycrystalline silicon or germanium. Since the commercial sector has moved mainly toward hyper-pure germanium detectors, the process for the creation of a germanium detector is described here. The germanium is put into a quartz "boat" where it is zone refined. The zone refining process is based on the principle that most impurities concentrate in the liquid phase as the germanium starts to freeze out. The germanium is heated by movable rf-coils which heat a segment of the germanium "metal" block and liquefy it. By moving the coil along the material, one end of the heated region solidifies and the other end melts, thereby carrying the impurities through the bar or ingot toward one end. This process is repeated several times to reach an acceptable level of impurities in the ingot. The contaminated ends are then removed from the bar. The zone refinery process usually yields an impurity improvement factor of 100. The remaining impurity in the germanium is then tested and a decision is made whether another zone refinery is necessary or whether a single crystal can be grown from the material. Figure A.1 shows the different schematic working steps in the manufacturing process for an EG&G-ORTEC hyper pure germanium detector [ORT97]. Once the purity of the material is at the right level the germanium is melted and a precisely cut seed crystal is dipped into the liquid. The seed is slowly under rotation withdrawn. The temperature of the melt has to be maintained just above the melting point of the germanium. The temperature and the withdrawal rate can be used to set the size and growth rate of the crystal. This process is called the Czochralski technique. The cold crystal is then cut by a string saw that is made of a wire which pulls a

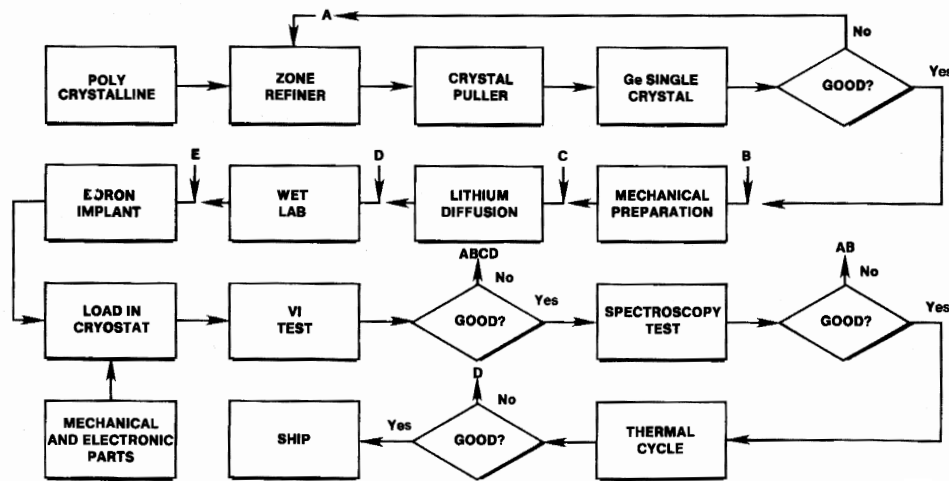


Figure A.1: Manufacturing process for a hyper pure germanium detector.

water and silicon carbide slur along. This mechanism is designed to prevent mechanical damage to the slices. The material is then tested again for impurities and the detector grade material is selected and ground perfectly cylindrical. In this selection process it is determined whether the detector contains a p or n impurity. The future charge bearing edge is then bevelled to decrease electric field edge effects. The non-bevelled side then has a hole machined into the crystal where the signal will be extracted. To form the  $n^+$  contact a lithium diffusion is applied. In the case of a p-type detector, on the entire outside, in the case of a n-type detector, on the inside walls of the hole. The surface not coated is the cylinder surface with the non beveled edge. The coating is about 600 microns thick. The surface is chemically polished and then coated with amorphous germanium hydride which is sputtered on as surface protection [HAN80]. The  $p^+$  contact is formed by ion implantation of boron ions into the opposite surface. This finishes the process for manufacturing the detector element.

The crystal is then mounted in its cryostat. A typical mount is shown in figure A.2 [ORT97]. It is visible that the dewar contains not only the detector element itself but also the first stage of the pre-amplifier, sometimes the whole pre-amplifier to cut down the thermal electronic noise. The contact pin usually presses the detector element in its holder to guarantee a good heat connection. Since these detectors

are built to detect gamma rays the materials used in the cup are to be as low in Z as possible. Hence the use of aluminum, Teflon, magnesium, beryllium, and Mylar is common.

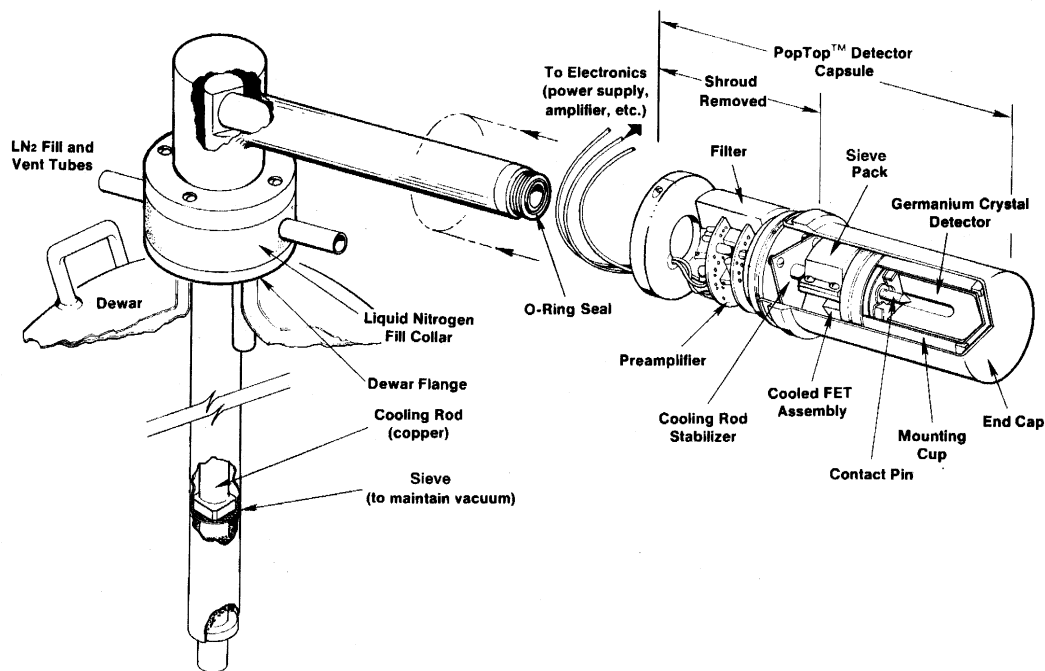


Figure A.2: Typical germanium detector cryostat.



# EQUIPMENT USED

---

This chapter shows the equipment used for the experiment, the Data acquisition and the analysis of the Data.

## B.1 EXPERIMENTAL EQUIPMENT

- Macintosh Quadra 850 (Apple)
  - OS 8.6
  - LANLDAQ (68K) (Data Acquisition Program)
  - MAC VEE & MAC CC
- IBM Pentium 100 MHz PC
  - Windows 95
  - Trump 8k 13bit ADC
  - Maestro (EG&G-ORTEC)
- 375x PM KV High Voltage Supply (Bertran)
- 325 PM KV High Voltage Supply (Bertran)
- C315 Majority Coincidence (EG&G-ORTEC)
- TR 8818A Transient Recorder (Le Croy)
- MM 8103A Memory (Le Croy)
- 2228A TDC (Le Croy)

- 705 Eight Channel Discriminator (Phillips Scientific)
- 711 Six Channel Discriminator (Phillips Scientific)
- 777 8 Channel Gain Amplifier (Phillips Scientific)
- 795 Quad Gate Delay Generator (Phillips Scientific)
- 672 EG&G-ORTEC Shapingamplifier
- RG 11-A EG&G-ORTEC Preamplifier
- P84 Pulse Generator (Berkley Nucleonics Corp.)
- 8082A HP Pulse Generator (Hewlett Packard)
- 9450 Dual 350 MHz Oscilloscope (Le Croy)
- 54542C 2GHz Oscilloscope (HP)
- TDS 224 100 MHz Oscilloscope (Tektronix)
- 871 Timer (EG&G-ORTEC)
- 579 Fast Filter Amplifier (EG&G-ORTEC)
- Delay Box (Range from 0.5 to 127.5 ns in 0.5 ns Steps)

## B.2 DATA ANALYSIS AND DOCUMENTATION EQUIPMENT

- Apple Macintosh Powerbook
  - Adobe Illustrator 8.0
  - Adobe Photoshop 5.5
  - IGOR PRO 2.0 - 3.0
  - Mini Cad 6.0
  - MS Excel
  - MS Word
  - Os 8.6
- Dual 800MHz Pentium III

- Linux Red Hat 6.2
- root (CERN analysis program)
- Geant 4 (CERN Monte-carlo)
- L<sup>A</sup>T<sub>E</sub>X 2<sub>ε</sub>



---

## BIBLIOGRAPHY

---

- [ADA62] J. A. S. Adams, "Radioactivity of the Lithosphere", in Nucl. Rad. Geo. Phys. 1, Academic Press, NY (1962).
- [ALL97] B. Allen, Phys. Rev. Lett. 79, 2624 (1997).
- [ALP48] . A. Alphner, H. Bethe, G. Gamoc, Phys. Rev. 73, 803 (1948).
- [AMB95] M. Ambrosio et al., (MACRO Colaboration), Phys. Ref. D Vol.52 3793 (1995).
- [AND87] Yu.M. Andreev, V.I. Gurenzov and I.M. Koagi, Proc. 20th Int. Cosmic Ray Conf. (Moscow) Vol.6 200 (1987).
- [BAC92] C. Baci et al., Phys. Lett. B, 293, 460 (1992).
- [BAU01] L. Baudis, private comuncations (2001).
- [BAU97] L. Baudis, H. V. Klapdor-Kleingrothaus et al., NIM A 385, 265 (1997).
- [BAU98a] L. Baudis, H. V. Klapdor-Kleingrothaus et al., Phys. Rev. D, 59, 22001 (1998).
- [BAU98b] L. Baudis, H. V. Klapdor-Kleingrothaus et al., Phys. Rep. 307, 301 (1998).
- [BED97] V. Bednyakov, H. V. Klapdor-Kleingrothaus, S. G. Kovalenko, Y. Ramachers, Z. Phys. A, 357, 339 (1997).
- [BEL01] P. Belli, R. Bernabei et al., Proceed. of the 20th Texas symp. on relativistic astrophysics, Austin, Dec 2000.
- [BER00] R. Bernabei et al. Phys. Lett. B, 480, 23 (2000).
- [BER01] M. J. Berger, J. H. Hubbell, and S. M. Seltzer,  
<http://physics.nist.gov/PhysRefData/Xcom/Text/XCOM.html>.
- [BER95] R. Bernabei, Rivista del Nouvo Cimentio, 18(5) 1 (1995).

- [BEZ73] Bezrukov, L.B., Beresnev, V.I., Zatsepin, G.T., Ryazhskaya, O.G., Stepanets, L.N., *Yadernaya Fizika*, Vol. 17, No.1, 98 (1973).
- [BOW97] T.J. Bowles, private communications (1997).
- [BRO85] R. L. Brodzinski, D. P. Brown, J. C. Eavans Jr., W. K. Hensley, J. H. Reeves, N. A. Wogman, F. T. Avignone III, H. S. Miley, *Nucl. Instrum. Meth.* A239 207 (1985).
- [BUH96] M. Bühler et al., *NIM A*, 370, 237 (1996).
- [BUR01] S. Burles, K. M. Nollet, M. Turner *Astrophys. J.* 552, 1 (2001).
- [BUR98] S. Burles, D. Tyler *Astrophys. J.* 499, 699 (1998).
- [CAL88] D. O. Caldwell et al. *Phys Rev. Lett.* 61(5), 510 (1988).
- [CAL90] D. O. Caldwell et al. *Phys Rev. Lett.* 65(11), 1305 (1990).
- [CAL99] D. O. Caldwell, *Nucl. Phys. B Proc. Suppl.* 70, 43 (1999).
- [CAM74] D. C. Camp, C. Gatrousis and L. A. Maynard, *Nucl. Instrum. Meth.* 117,189 (1974).
- [CAR00] J. Carlstrom, *Physica Scripta*, T85, 148 (2000).
- [COP43] Copernicus, N. *De revolutionibus orbium coelestium*, 1543 (Nuremberg, Germany)
- [COW87] L.L. Cowie, M. Henriksen and R. Mushotzky *Astro. Phys. J.*, 317, 593 (1987).
- [CRO87] M. Crouch, *Proc. 20th Int. Cosmic Ray Conf. (Moscow)* Vol.6 165 (1987).
- [DAS96] A. J. da Silva, thesis, "Development of a low background environment for the cryogenic dark matter search"(1996).
- [DEK72] De K.E. et al. *Phys. Rev. D* 5 1068 (1972).
- [DER97] A. Derbin, private communication (1997).
- [DOD96] S. Dodelson, E. I. Gates, M.S. Turner, *Science* 274, 192 (1996).
- [EIN16] A. Einstein, *Ann. d. Phys.* 49, 50 (1916).

- [EVR96] A. E. Evrad MNRAS 292, 298 (1996).
- [FEI68] Y. Feige, B. G. Oltman and J. Kastner, J. Geophys. Res., 73, 3135(1968).
- [FIO84] E. Fiorini, T. O. Niinkoski, NIM 225,83 (1984).
- [FIR96] R. B. Firestone, V. S. Shirley, Table of Isotopes eighth edition.
- [FLO88] T. Forkowski, L. Morawska and K. Rozanski, Nucl. Geophys., 2, 1 (1988).
- [FOR95] G. Forster, Nucl. Phys. B Proc. Suppl. 44, 175 (1995).
- [FRE01] W. L. Freedman et al. Astro. Phys. J. 553, 47, (2001).
- [FUK98] Y. Fukunda et. al (Super Kamiokande Colaboration) Phys. Rev. Lett. 81, 1562 (1998).
- [FUS93] K. Fushimi et al., Phys. Rev. C, 14, R425 (1993).
- [GAL32] Galileo, G./ Dialogue in the two chief world systems, 1632 (Florence)
- [GAM46] G. Gamow, Phys. Rev. 70, 572 (1946).
- [GAM49] G. Gamov, R. Alpher and R. M. Herman detection of microwave background.
- [GER90] G. Gerbier et al, Phys Rev. D, 42(9) 3211 (1990).
- [GIR98] M. Girardi et al. Astro. Phys. J., 505, 74 (1998).
- [GON85] A. Goned, M. Shalaby, A. M. Salem, M. Roushdy, Proc. int. cosmic ray conf. HE5.4-10, 192 (1985).
- [GRE01] L. Grego et al. Astro. Phys. J., 552, 2 (2001).
- [GUN96] K.F. Gunn and P.A. Thomas MNRAS., 281, 1133 (1996).
- [HAB97] S.Habib Los Alamos Science., 25, 180 (1997).
- [HAN80] W. L. Hansen et al. IEEE Trans. on Nucl. Sci., NS-27, 1 (1980).
- [HUB26] E.Hubble Astro Phys. J., 84, 158 (1926).
- [HUB29] E.Hubble Nat. Ac. Sci., 15, 168 (1929).

- [HUW97] W. Hu, N. Sugiyama, J. Silk, *Nature*, 286, 37 (1997).
- [KAP01] M. Kaplinghat, M. S. Turner, *Phys. Rev. Lett.* 86(3), 385 (2001).
- [KEN86] S. M. Kent, *Astro. Jnl.* 4, 816 (1986).
- [KEN87] S. M. Kent, *Astro. J.* 96, 816 (1987).
- [KEP09] Kepler, J. *Astronomia Nova* 1609 (Graz, Austria)
- [KEP19] Kepler, J. *Harmonice Mundi* 1619 (Graz, Austria)
- [KNO99] G. F. Knoll *Radiation Detection and Measurements*.
- [KRI69] M. H. Krieger: Thesis Columbia University, NEVIS-172 (1969).
- [LAB95] M. A. Labreche, M.A. Beikmann, J.D. Osnes, B.M. Butcher, Sandia-Report SAND94-0890 UC-721.
- [LAL67] D. Lal, B. Peters *Handbuch der Physik* 46/2, 551 (1967).
- [LEE77] B. W. Lee, S. Weinberg, *Phys. Rev. Lett.* 39(4) 165 (1977).
- [LIN63] J. Lindhard, V. Nielsen, M. Scharff, P. V. Thomsen, *Mat. Phys, Medd. Dan. Vid. Selsk.* 33, 10 (1963).
- [MCD65] B. MacDonald, J. A. Diaz, S. N. Kaplan, R. V. Pyle, *Phys Rev* 139, B 1253 (1965).
- [MIY73] S. Miyake, 13th int. cosmic ray conf. Denver, CO Vol. 5 3638 (1973).
- [MOH98] J. Mohr et al *Astro. Phys. J.*, 517, 627 (1998).
- [NET01] C. B. Netterfield et al., *Astro. Phys. J.*, 552, 718 (2001),
- [NIS01] NIST Database, <http://rrdjazz.nist.gov/resources/n-lengths/list.html> (2001).
- [OME01] J. M. O'Meara et al., *Astro. Phys. J.*, 552, 718 (2001).
- [ORT97] EG&G-ORTEC Catalog (1997).
- [PAN87] S. DePanfilis, A. C $\check{z}$  Melissinos, D. E. Moskowitz, J. T. Rogers, Y. K. Semerzidis, W. U. Wuensch, *Phys. Rev. Lett.* 59(7)839 (1987).

- [PAS93] M.P. De Pascall et al., *J Geophys. Res.* 98, 3501 (1993).
- [PAU30] G.J. Toomer, "Wolfgang Pauli Wissenschaftlicher Briefwechsel mit Bohr, Einstein, Heissenberg u. a." Band II 39 (Springer Verlag, Berlin 1985).
- [PEC77] R. D. Pecci, H. R. Qinn. *Phy. Rev. Lett.* 38(25) 1440 (1977).
- [PEN65] A. Pnezias and R. Wilson detection of microwave background.
- [PER99] S. Perlmutter et al., *Astro. Phys. J.* 517, 565 (1999).
- [POP97] L. Popeko, private communications (1997).
- [PRI88] J. R. Primack, D. Seckel, B. Sadulet, *Ann. Rev. Nucl. Part. Sci.*, 38 751 (1988).
- [PRY01] C. Pryke et al., astro-ph/0104490 (2001).
- [RAS84] B.C. Rastin, *J. Phys. G10*, 1609 (1984).
- [REI59] F. Reines, C. L. Cowan Jr, *Phys. Rev.* 113, 273 (1959).
- [REU91] D. Reusser et al., *Phys. Lett. B.* 255, 143 (1991).
- [RIE98] A. Riess et al *Astrophys. J.* 504(2) 935 (1998).
- [ROO01] R. Brun, <http://root.cern.ch> (2001).
- [SAT65] A. R. Sattler, *Phys. Rev.* 138, A1815 (1965).
- [SCH71] W. U. Schröder: Thesis Technisch Hochschule Darmstadt (1971).
- [SCH98] B. P. Schmidt et al *Astrophys. J.* 507(1) 46 (1998).
- [SCR98] D. N. Schramm, M. S. Turner, *Rev. mod. Phys.* 70(1) 303 (1998).
- [SIL84] J. Silk, M. Srednicki, *Phys. Rev. Lett.* 53(6), 624 (1984).
- [SIN62] P. Singer, *Nuovo Cimento* 23, 669, (1962).
- [SIN74] P. Singer, *Springer Tracts in Modern Physics*, (1974).
- [SMI90] P.F. Smith and J.D. Lewin *Phys. Rep.*, 187, 203. (1990).
- [SNO01] SNO Colaboration, preprint nucl-ex/0106015 (2001).

- 
- [SNO87] SNO Colaboration, Sudbury Neutrino Observatory Proposal, SNO-87-12 (1987).
- [SPO91] N. J. C. Spooner et al., NIM A, 310,227(1991).
- [TUR01] M. S. Turner, astro-ph/0106035 (2001).
- [TUR98] M Turner, Cosmological Parameters, Preprint (1998).
- [TUR99] M Turner, Nucl. Phys. B. (Proc. Suppl.) 72 69 (1999).
- [WEB98] J. Web, personal conversation at Carlsbad Environmental Monitoring and Research Center (1998).
- [WIL98] J. Willick, M. sTrauss, Astro. Phys. J. 507, 64 (1998).
- [WOL73] A. W. Wolfendale, Cosmic rays at ground level (1973).
- [WOU99] J. Wouters, private comuncations (1999).
- [ZWI33] F. Zwicky, Helv. Phys. Acta., 6, 110 (1933).
- [ZWI42] F. Zwicky, Phys. Rev., 61, 489 (1942).